DECAY RADIOACTIVITY INDUCED IN PLASMA-FACING MATERIALS BY DEUTERIUM-TRITIUM NEUTRONS

BLANKET ENGINEERING

KEYWORDS: *fusion, induced radioactivity, experiments and calculations*

A. KUMAR *University of California, Los Angeles*
School of Engineering and Applied Science
Mechanical, Aerospace, and Nuclear Engineering Department
Los Angeles, California 90095

Y. IKEDA *Japan Atomic Energy Research Institute*
Department of Reactor Engineering, Tokai Research Establishment
Tokai-mura, Naka-gun, Ibaraki-ken 319-11 Japan

M. A. ABDOU and M. Z. YOUSSEF *University of California, Los Angeles*
School of Engineering and Applied Science
Mechanical, Aerospace, and Nuclear Engineering Department
Los Angeles, California 90095

C. KONNO, K. KOSAKO, Y. OYAMA, T. NAKAMURA, and H. MAEKAWA *Japan Atomic Energy Research Institute*
Department of Reactor Engineering, Tokai Research Establishment
Tokai-mura, Naka-gun, Ibaraki-ken 319-11 Japan

Received January 28, 1994
Accepted for Publication July 28, 1994

Deuterium-tritium (D-T) neutron-induced radioactivity constitutes one of the foremost issues in fusion reactor design. Designers have been using radioactivity codes and associated nuclear data libraries for nucleonic designs of fusion reactors. However, in the past, there was hardly any experimental validation of these codes/libraries.

An elaborate, experimental program was initiated in 1988 under a U.S. Department of Energy/Japan Atomic Energy Research Institute collaborative program to validate the radioactivity codes/libraries. Measurements of decay gamma spectra from irradiated, high-purity samples of Al, Si, Ti, V, Cr, Mn-Cu alloy, Fe, Co, Ni, Cu, SS316/AISI316, Zn, Zr, Nb, Mo, In, Sn, Ta, W, and Pb, among others, have been carried out under D-T neutron fluences ranging from 1.6 × 10^{10} to 6.1 × 10^{13} n/cm^2 and cooling times ranging from ~10 min to ~3 weeks. As many as 14 neutron energy spectra were covered for a number of materials.

The analyses of the isotopic activities of the irradiated materials using the activation cross-section libraries of four leading radioactivity codes, i.e., ACT4/THIDA-2, REAC-3, DKR-ICF, and RACC, have shown large discrepancies among the calculations on one hand and between the calculations and the measurements, on the other. Vanadium, Co, Ni, Zn, Zr, Mo, In, Sn, and W each count the largest number of discrepant isotopic activities. It is strongly recommended to continue additional radioactivity experiments under additional neutron energy spectra and large neutron fluence on one hand and to improve activation cross sections related to the problematic isotopic activities on the other. A unique activation cross-section library and associated radioactivity code are also recommended for the best results.

In addition to providing detailed results of the status of predictability of individual isotopic activities using the ACT4, REAC-3, DKR-ICF, and RACC activation cross-section libraries, safety factors cum quality factors characterizing each library are presented and discussed. The related issues of confidence level and associated uncertainty are also highlighted. These considerations are of direct practical importance to reactor designers.

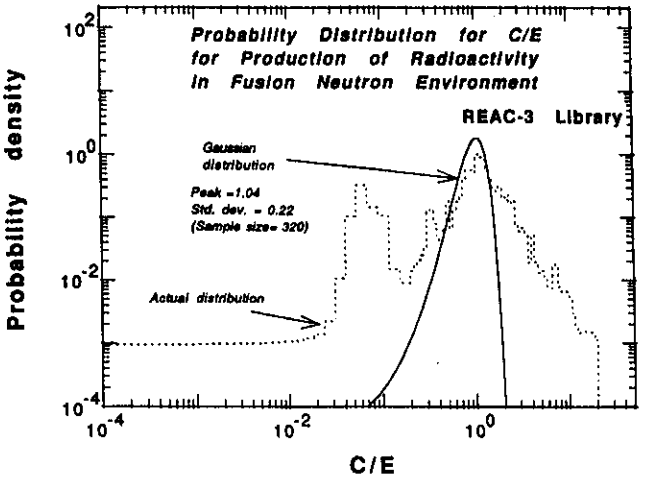

Fig. 107. Probability density distribution of C/Es obtained using REAC-3 library.

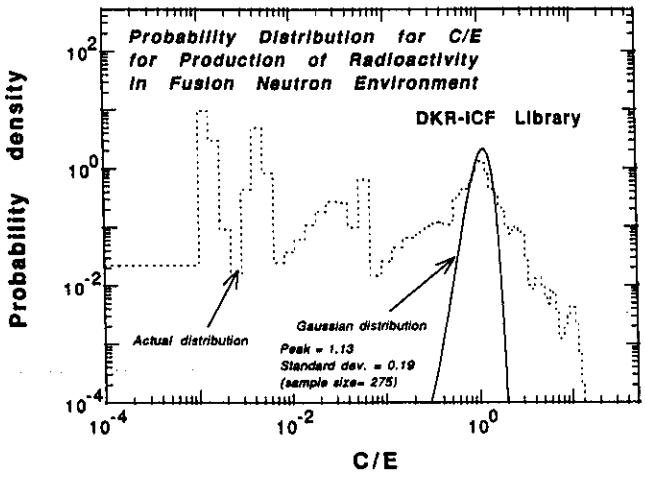

Fig. 108. Probability density distribution of C/Es obtained using DKR-ICF library.

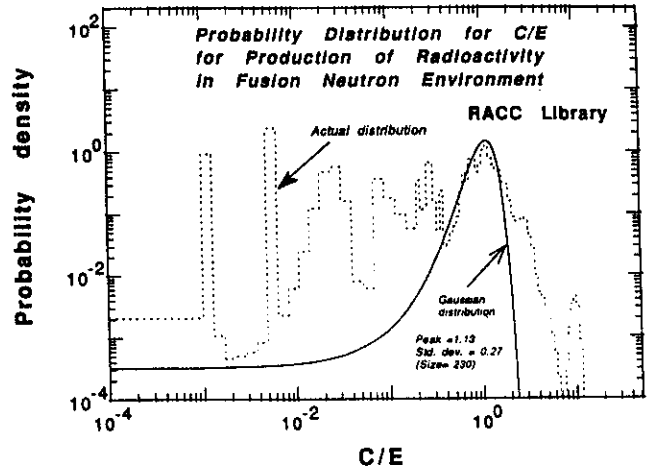

Fig. 109. Probability density distribution of C/Es obtained using RACC library.

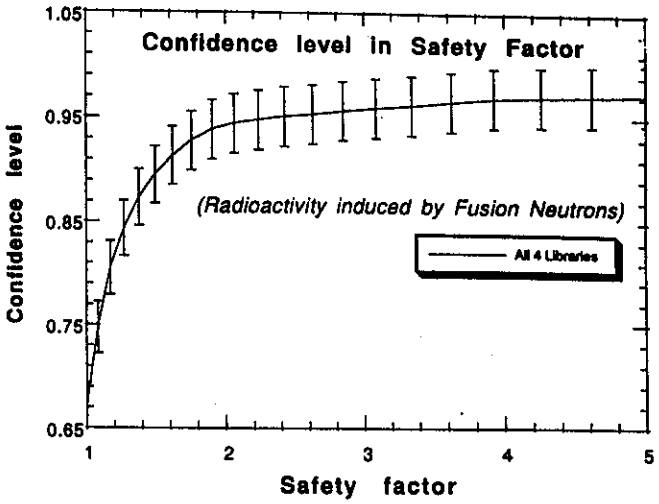

Fig. 110. Fractional confidence level and associated uncertainty as a function of safety factor, using consolidated probability density distribution of C/Es.

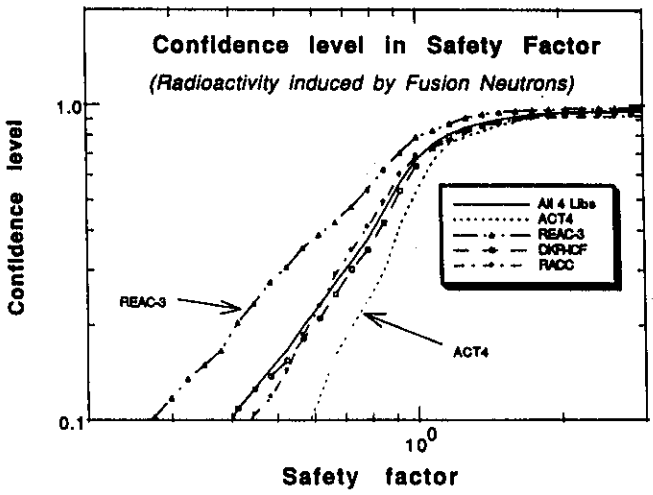

Fig. 111. Fractional confidence level for each of the four libraries as a function of safety factor.

products, it is by no means established that the trends for the other materials will continue to be as favorable under different neutron energy spectra and fluences. These tables are only indicative of the problems that have already been observed. New problem isotopes are likely to be added to this list as the experimentation and the analysis is further strengthened in future. The future experimental work should proceed along the following directions:

1. experiments focusing on the problem isotopes listed in Tables XXIII and XXIV, if it would be difficult to improve significantly on the neutron fluences with respect to those obtained in the reported experiments

I. INTRODUCTION

One of the foremost issues in fusion reactor design is neutron-induced radioactivity. Reactor safety, biological hazard, reactor maintenance, after-shutdown cooling, and waste disposal are among the critical issues impacting the selection of materials for various components from the first wall to the pressure vessel.[1-7]

Decay heat in a deuterium-tritium (D-T) fusion reactor will result from neutron-induced radioactive isotopes. The bulk of the recommended fusion reactor materials have low to medium Z. As a result, most of the produced radioactive isotopes de-excite via beta decay (electron/positron emission), electron capture (EC), or isomeric transition (IT). Most often, beta decay and electron capture are also followed by gamma decay. Ideally, one would welcome efforts to do both beta and gamma spectroscopy of emitted radiations from the radioactive isotopes. But, gamma spectroscopy alone is capable of providing a wealth of extremely valuable data at this early stage of research and development (R&D) effort in this area.

Type 316 stainless steel, V-Cr-Ti alloy, copper-alloys, ferritic steel, molybdenum, niobium, tantalum, and tungsten have been proposed, in one form or the other, as plasma-facing materials for fusion reactors like International Thermonuclear Experimental Reactor (ITER), Next European Torus (NET), Compact Ignition Tokamak (CIT), Fusion Experimental Reactor (FER), etc. A series of experimental measurements of neutron-induced radioactivity, in samples of the plasma-facing and other materials, were carried out in the years 1988 through 1991 at the Fusion Neutronics Source (FNS) facility of the Japan Atomic Energy Research Institute (JAERI) under the U.S. Department of Energy (U.S. DOE)/JAERI collaborative program on fusion neutronics.[8-17] The measurements consisted of gamma spectroscopy of material samples irradiated under a prototypical fusion environment. Multiple irradiation and cooling times along with different spectral conditions were implemented. The irradiated materials during Phases-IIC through -IIIC included Fe, Ni, Cr, MnCu alloy, Ti, Mo, Zr, Ta, W, Si, Mg, Al, V, Nb, Type 316 stainless steel, $YBa_2Cu_3O_7$, $ErBa_2Cu_3O_7$, Sn, Ag, Pb, Zn, and In. Most of these measurements had already been analyzed using four leading radioactivity codes, i.e., ACT4/THIDA-2 (Ref. 18), REAC-2 (Ref. 19), DKR-ICF (Ref. 20), and RACC (Ref. 21), and the results presented in a number of publications.[8-17] The present work, however, gives results of a new analysis that looks directly at individual isotopic activities of irradiated samples of Al, Si, Ti, V, Cr, Mn, Fe, Co, Ni, Cu, Type 316 stainless steel, Zn, Zr, Nb, Mo, In, Sn, Ta, and W. In the new analysis, rather than using the code and library system as a whole, a simplified, common code that uses all the four activation cross-section libraries has been used. This home-grown code ensures that a unique set of data on half-lives, branching ratios, and decay-gamma yields is used for calculation of isotopic activities with different libraries. The data documented in Ref. 22 have been chosen as a primary source for isotopic half-lives, branching ratios, and decay-gamma yields. This kind of analysis helps to focus on the role of the activation cross sections in contributing to discrepancies between the calculation and the experiment in a more direct manner.

In addition to providing detailed results on the status of the predictability of individual isotopic activities using the ACT4, REAC-3, DKR-ICF, and RACC activation cross-section libraries, an attempt has been made to qualify these libraries from the practical viewpoint of a reactor designer. In this regard, safety factors cum quality factors, characterizing each library, have been defined and discussed. Also, the related issues of confidence level and associated uncertainty have been highlighted. These considerations are of direct practical importance to the reactor designers as the latter would like to know beforehand how much confidence they can place in a given activation cross-section library for the nucleonic design of a fusion reactor.

II. EXPERIMENTS

In a fusion reactor environment, the neutron energy spectrum will vary from place to place. The hardest spectrum will be found in close proximity to the burning plasma. As one moves away from the plasma, the spectrum will become softer because of slowing down of 14-MeV D-T neutrons in the first wall/blanket/shield and any other surrounding medium. Thus, materials at different locations inside the fusion reactor will experience different neutron energy spectra. Production cross sections for radioactive isotopes are functions of neutron energy. The (n,n'), (n,p), (n,α), $(n,2n)$, $(n,n'p)$, $(n,^3\mathrm{He})$, (n,d), and (n,t) reactions are generally endothermic and are thus provoked by higher energy neutrons. Contrarily, the (n,γ) reaction is an exothermic reaction and is thus driven by lower energy neutrons. The production cross sections, gamma yields, and gamma half-life data for most of the radioactive isotopes of fusion interest need early validation as all design strategies are critically dependent on it. Figure 1 shows schematically the role of the integral experiments of induced radioactivity for the fusion applications.

II.A. Strategy

Ideally, one needs to have a neutron source that will allow the realization of an intense monoenergetic neutron flux such that one can vary the neutron energy from 14 MeV right down to 0.025 eV or lower. Different material samples could then be irradiated under any desired neutron energy spectrum. But, this approach is impossible to realize because of lack of availability of monoenergetic neutron sources over the energy range of interest on one hand and huge requirements of

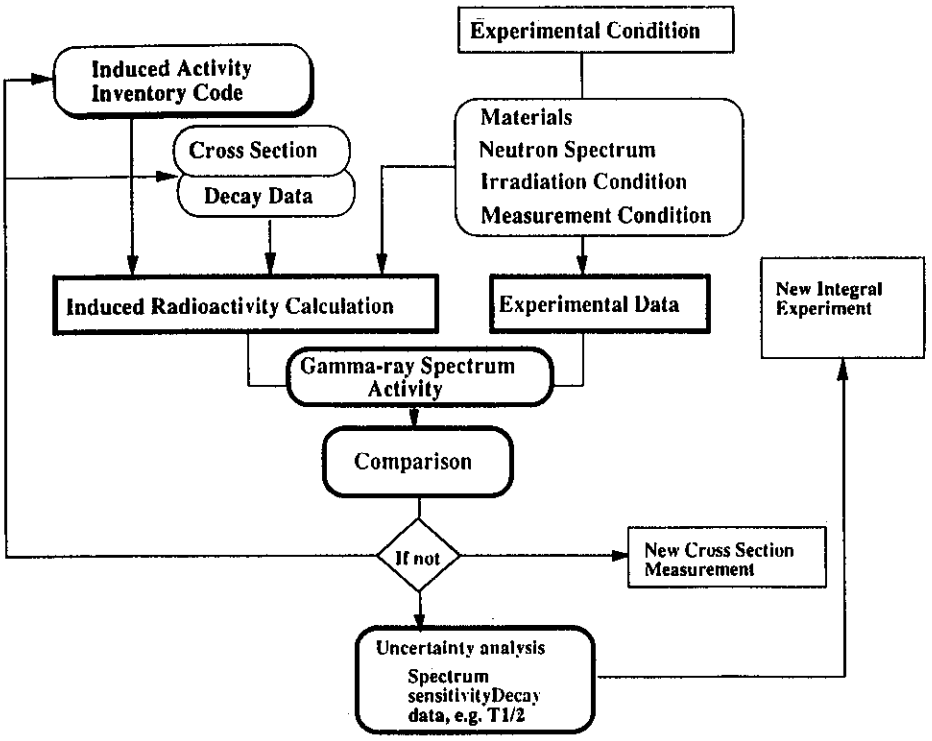

Fig. 1. Role of integral experiments of induced radioactivity for the fusion applications.

expense and effort, even for the few monoenergetic sources that one can utilize, on the other. A cruder but more practical approach consists of irradiating material samples in select locations in a simulated fusion reactor environment. One will obtain an integral effect of the neutron energy spectrum at each location. A number of small material samples can be kept at each location as long as they have a minimal impact on the neutron energy spectrum in the immediate neighborhood. Figure 2 gives a schematic view of a typical experimental arrangement of sample materials. In fact, this was realized in the first experiments done under the U.S.

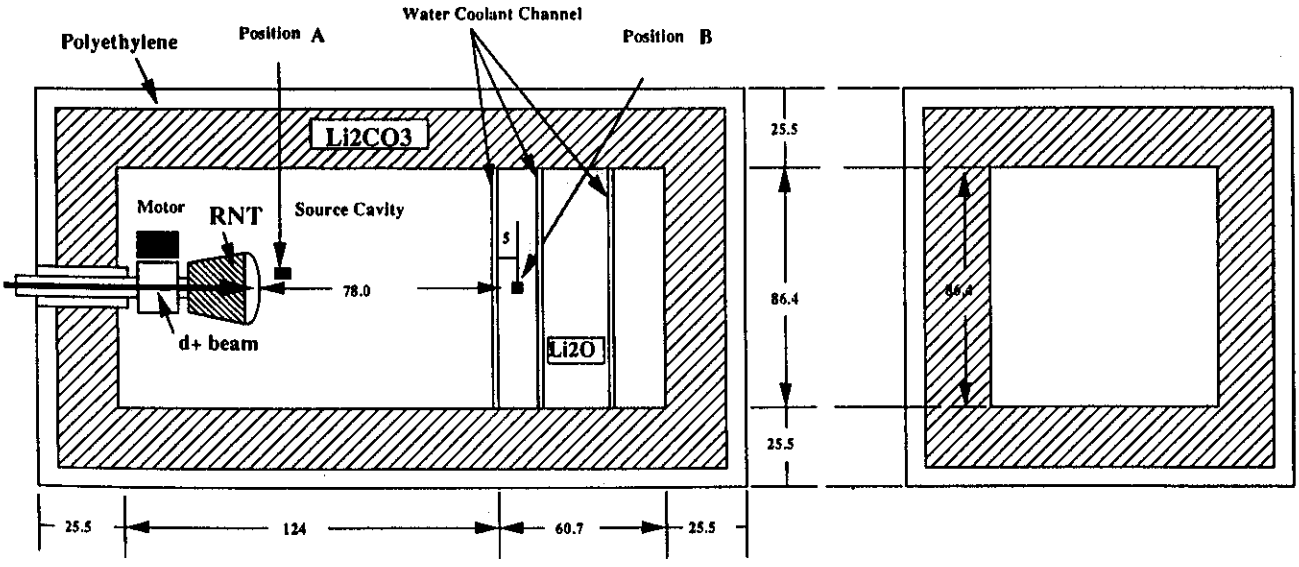

Fig. 2. Schematic view of typical experimental arrangement of sample materials.

DOE/JAERI collaborative program in the coolant channel assembly of Phase-IIC (Refs. 8, 9, and 10).

The U.S. DOE/JAERI collaborative and experimental program on fusion neutronics was designed to simulate reactor-relevant neutron energy spectra in tritium breeding blankets over the years. Two sources of 14-MeV neutrons were used at the FNS facility of JAERI. A rotating neutron target (RNT) source (nominal intensity = 3×10^{12} n/s) was employed in Phases-I through -IIC. A fixed neutron target with lower nominal intensity ($\sim 3 \times 10^{11}$ n/s) was used in later phases, Phases-IIIA, -IIIB, and -IIIC, where the line source was simulated.[11,23-25] Induced radioactivity measurements were conducted during all phases, beginning with Phase-IIC, as shown in Fig. 2.

II.B. Measured Items

The ideal objective of the present series of experiments would have been to measure the gamma spectrum of each induced radioactivity for obtaining complete information on radioactivity characteristics of each irradiation environment. However, the gamma-emitting radioactive isotopes span a large range of half-lives, going from a fraction of a second to one million years. Practical considerations oblige us to first focus on half-lives comprised of a few minutes to a few years. Even in this case, the number and the lengths of the irradiation periods have to be so optimized as to obtain adequate and yet statistically meaningful data on a broad range of half-lives within a limited availability of the neutron source, gamma detectors, and manpower. It was thought practical to include at the most two irradiations per experimental period: Shorter irradiation of ~30 min was deemed adequate for shorter half-lives ranging from a few minutes to a few hours; an irradiation of 9 to 10 h was generally chosen for half-lives ranging from a few hours to a few years. Radioactive samples were cooled for different times and a readoff on two to four detectors that were available.

Table I summarizes data on the chemical compositions of the irradiated samples. The chemical compositions were supplied by two commercial suppliers of foils, i.e., Reactor Experiments (San Carlos, California) and Goodfellow Corporation (Malvern, Pennsylvania). Isotopic compositions were adapted from

TABLE I

Chemical Composition of Primary Impurities in the Samples Used in Induced Activity Irradiations

Sample Material	Chemical Composition by Maximum Weight Percent
Magnesium (Mg)	99.78 Mg, 0.10 Al, 0.07 Zr, 0.02 Mn, 0.01 Si
Aluminum (Al)	99.97 Al, 0.006 Mg
Titanium (Ti)-^{RE}	99.79 Ti, 0.12 O, 0.06 Fe, 0.02 C
Titanium (Ti)-^{GF}	99.6 Ti, 0.13 O, 0.03 Al, 0.03 Cr, 0.03 Mn, 0.03 Mn, 0.03 Ni, 0.03 V, 0.02 Fe
Vanadium (V)	99.82 V, 0.044 Si, 0.03 Ta, 0.03 O, 0.013 Mo, 0.01 Zr, 0.01 Fe, 0.01 Al, 0.01 Hf
Chromium (Cr)	99.0 Cr, 0.43 Fe, 0.10 Al, 0.05 Si
Mn-Cu alloy (MnCu)	79.78 Mn, 19.66 Cu, 0.46 Ni, 0.07 Fe
Iron (Fe)	99.92 Fe, 0.059 Mn, 0.02 C
Stainless steel SS316	66.22 Fe, 17.75 Cr, 11.60 Ni, 2.08 Mo, 1.33 Mn, 0.42 Si, 0.19 Co, 0.34 Cu, 0.06 V
Stainless steel AISI316	68.6 Fe, 16.5 Cr, 11.30 Ni, 2.12 Mo, 1.46 Mn
Cobalt (Co)	99.95 Co, 0.04 Ni
Nickel (Ni)	99.97 Ni, 0.016 C
Copper (Cu)	99.999 Cu, 0.0002 Ag
Zinc (Zn)	99.95 Zn, 0.038 Pb, 0.006 Cu, 0.004 Cd, 0.002 Sn, 0.0004 Ag
Zirconium (Zr)	99.76 Zr, 0.10 Fe, 0.09 Si, 0.03 Ti
Yttrium (Y)	99.9 Y, 0.06 Ta, 0.005 Gd, 0.002 Eu
Niobium (Nb)	99.91 Nb, 0.018 Ta, 0.01 Zr
Molybdenum (Mo)	99.93 Mo, 0.03 W, 0.01 Fe
Silver (Ag)	99.95 Ag, 0.043 Cu, 0.003 Fe, 0.003 Zn, 0.0006 Pb
Indium (In)	99.99 In, 0.003 Cu
Tin (Sn)	99.87 Sn, 0.02 Cu, 0.02 Sb, 0.02 Pb, 0.01 Fe, 0.01 Ni, 0.01 Co, 0.01 S, 0.01 As, 0.01 Bi
Tantalum (Ta)	99.98 Ta, 0.007 Fe
Tungsten (W)	99.97 W, 0.008 Si
Lead (Pb)	99.95 Pb, 0.023 Bi, 0.016 Sn, 0.005 Ag, 0.005 Cu, 0.001 Ti

RE = Sample supplied by Reactor Experiments, Inc.
GF = Sample supplied by Goodfellow Corporation.

Ref. 26. The decay gamma yields were taken from Ref. 22 and are listed materialwise in Table 3 of Ref. 17.

II.C. Irradiation Environment

Irradiation of foil packets[8-17] was carried out in fusion blanket assemblies of the U.S. DOE/JAERI collaborative program during Phases-IIC, through -IIIC. The Phase-IIC experimental assembly was driven by a point neutron source. The experimental assemblies in Phases-IIIA, -IIIB, and -IIIC were driven by a simulated line source. The mean source neutron intensities during the latter experiments were an order lower. Figures 2 and 3 show irradiation geometries during the Phases-IIC, -IIIA, and -IIIB experiments. Table II gives a description of the spectral conditions and the identifiers. Table II also yields a mean 14-MeV neutron intensity during each experiment. In all, 14 spectral locations were used. They are identified as A through N (see Table II). The neutron fluence realized during these experiments is estimated to range from 1.6×10^{10} to 6.1×10^{13} n/cm^2. Tables III through VI give a materialwise summary of the spectral conditions, the irradiation times, the cooling times range, and the counting times range. The gamma spectroscopy of each sample was done using four intrinsic germanium detectors and for multiple cooling periods ranging from 20 min to 10 days. Three detectors were relatively calibrated with respect to an absolutely calibrated standard detector, detector 5S. The counting times ranged from 10 min to 20 h. The neutron energy spectrum, irradiation time, source neutron intensity, cooling time, and counting time were among the major controlling parameters characterizing the measured decay gamma radioactivity.

II.D. Data Reduction

The gamma pulse-height spectrum for a sample for each cooling time was processed by a BOB75 spectrum analysis code[27] to obtain the gamma-ray intensity spectrum. Then, gamma peaks corresponding to the background were identified and removed. The resulting spectrum was then corrected for detector efficiency and attenuation of decay gammas emitted in a sample. The plot of absolute gamma detection efficiency as a function of gamma energy for standard detector 5S is available in Ref. 17. Some of the gamma peaks in the experimental data collected over the relative detectors had to be corrected against the sum peak effect. Variation of the source neutron intensity during irradiation was accounted for to finally obtain the decay gamma emission rate per gram for a normalizing source neutron intensity of 10^{12} n/s. For the simulated line source (step/continuous mode), the correction is applied to account for decay during the intervening period for the step mode and also to account for decay during movement for the continuous mode as the speed of movement is not totally uniform over a cycle itself and the speed is quite low.[11,23,24] The decay gamma emission rate E_{act} for an identified peak is given as

$$E_{act} = \lambda \cdot C / \{\epsilon \cdot w \cdot \mu \cdot S_f \cdot Y_n \cdot [1 - \exp(-\lambda \cdot t_m)]\} ,$$

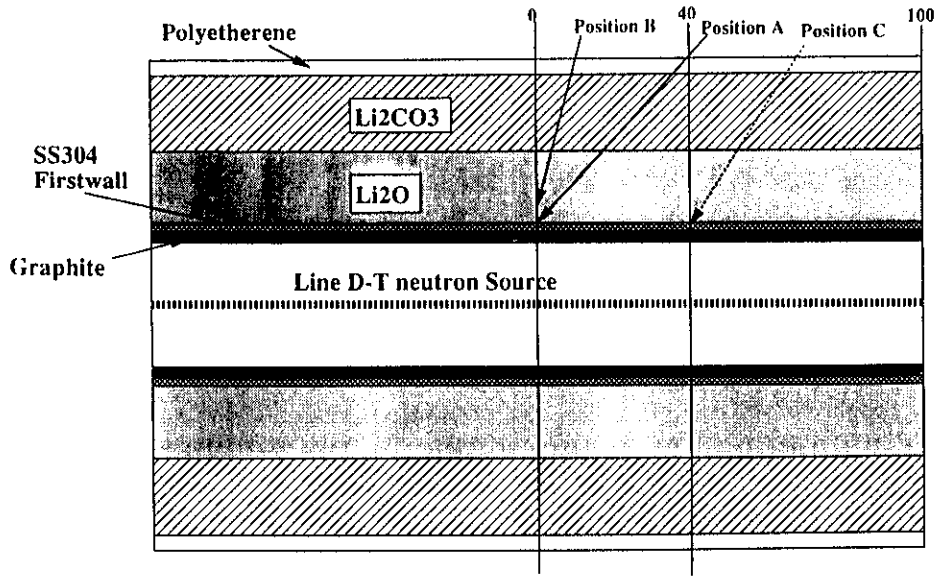

Phase-III Experimental Assembly
Phase-IIIA: without graphite
Phase-IIIB: with graphite

Fig. 3. Experimental geometry of Phases-IIIA, -IIB, and -IIIC.

TABLE II

Description of Spectral Conditions and Identifiers

Experimental Period	Spectral Conditions		Irradiation Time	Mean 14-MeV Intensity
	Location	Identifier		
December 2, 1988 (Phase-IIC: water-coolant channel)	(10, 0) cm	A1	30 min	1.70×10^{12} n/s
	(10, 0) cm	A2	9 h	8.75×10^{11} n/s
	(82, 5) cm	B1	30 min	1.28×10^{12} n/s
	(82, 5) cm	B2	10 h	1.12×10^{12} n/s
November 9, 1989 (Phase-IIIA: bare line source)	(0, 21.9) cm	C1	9 h, 47 min	1.88×10^{11} n/s (9.40×10^{8} n/cm/s)
	(40, 21.9) cm	D1	9 h, 47 min	1.88×10^{11} n/cm/s (9.40×10^{8} n/cm/s)
	(100, 21.9) cm	E1	9 h, 47 min	1.88×10^{11} n/cm/s (9.40×10^{8} n/cm/s)
November 21, 1989 (Phase-IIIA: point source inside annular blanket)	(0, 23.4) cm	F1	30 min	2.42×10^{11} n/s
	(0, 22.9) cm	G1	30 min	2.42×10^{11} n/s
November 22, 1989 (Phase-IIIA: line-source-driven annular blanket)	(0, 23.4) cm	H1	9 h, 51 min, 5 s	1.93×10^{11} n/s (9.66×10^{8} n/cm/s)
	(0, 28.5) cm	I1	9 h, 51 min, 5 s	1.93×10^{11} n/s (9.66×10^{8} n/cm/s)
	(40, 23.4) cm	J1	9 h, 51 min, 5 s	1.93×10^{11} n/s (9.66×10^{8} n/cm/s)
November 1, 1990 (Phase-IIIB: line-source-driven annular blanket with 1-in. thick graphite armor)	(0, 23.4) cm	K1	10 h, 29 min, 40 s	1.31×10^{11} n/s (6.55×10^{8} n/cm/s)
	(40, 23.4) cm	L1	10 h, 29 min, 40 s	1.31×10^{11} n/s (6.55×10^{8} n/cm/s)
November 15, 1991 (Phase-IIIC: line-source-driven annular blanket with graphite armor and a large side opening, 43 × 43 cm)	(0, 23.4) cm	M1	10 h, 6 min, 33 s	2.16×10^{11} n/s (1.08×10^{9} n/cm/s)
	(0, 21.9) cm	N1	10 h, 6 min, 33 s	2.16×10^{11} n/s (1.08×10^{9} n/cm/s)

where

λ = decay constant of radioactivity

C = gamma-ray peak counts

S_f = correction factor to account for source neutron intensity variation and/or decay during line source simulation

ϵ = absolute detector efficiency

μ = correction factor for gamma-ray attenuation inside the irradiated sample

w = sample weight

t_m = collection time

Y_n = normalized source neutron intensity = mean source neutron intensity $\times 10^{-12}$.

Generally, a different treatment is given to 511 KeV, for example, resulting from positron annihilation, and those gamma peaks that are either hard to characterize without ambiguity or result only from daughters of primary reaction products. In this situation, we replace $\lambda/[1 - \exp(-\lambda \cdot t_m)]$ by $1/t_m$ in the foregoing relation.

II.E. Experimental Error

Regarding error estimation on experimental measurements, it is to be recognized that a number of parameters affect counting statistics. The primary parameters include neutron flux, half-life of gamma emitter, detector efficiency, cooling time, counting time, activation cross section, and atom density. It is impossible to give a single figure for even one sample material as is amply brought out in Fig. 4, which shows the percent standard deviation on decay rates for different products as a function of half-life for a molybdenum sample. The molybdenum sample was irradiated in a point-source-driven-assembly experiment during Phase-IIIA. Irradiation (*tr*), cooling (*tcool*), and counting (*tcount*) times are 30 min, 3 h 18.2 min, and 10.75 min, respectively.

TABLE III

Summary of Spectral Conditions, Irradiation Times, Cooling Times, and Counting Times for Titanium, Vanadium, and Chromium

Irradiated Material	Spectral Conditions	Irradiation Times Range	Cooling Times Range	Counting Times Range
Titanium	A1,A2,B1,B2,C1,C2,H1,I1,L1	30 min to 10.49 h	22.3 min to 7.52 days	10 min to 17.28 h
Vanadium	A1,A2,B1,B2,C1,L1,L2	30 min to 10.49 h	22.3 min to 7.75 days	10 min to 17.29 h
Chromium	A2,B2,K1	9 h to 10.49 h	1.2 h to 7.61 days	21.6 min to 17.0 h

TABLE IV

Summary of Spectral Conditions, Irradiation Times, Cooling Times, and Counting Times for Silicon, Manganese, Iron, Cobalt, Nickel, and Molybdenum

Irradiated Material	Spectral Conditions	Irradiation Times Range	Cooling Times Range	Counting Times Range
Silicon	A1	30 min	37.3 min	15 min
Manganese (as Mn-Cu alloy)	A1,A2,B1,B2,K1	30 min to 10.49 h	12.3 min to 6.88 days	10 min to 6.75 h
Iron	A1,A2,B1,B2,C1,D1,E1,F1,G1,H1,I1,J1,L1	30 min to 10.49 h	22.4 min to 7.94 days	10 min to 14.20 h
Cobalt	A1,A2,B1,B2,C1,K1	30 min to 10.49 h	37.3 min to 6.90 days	15 min to 14.52 h
Nickel	A1,A2,B1,B2,C1,D1,E1,F1,G1,H1,I1,J1,K1	30 min to 10.49 h	44 min to 7.61 days	8.6 min to 14.32 h
Molybdenum	A1,A2,B1,B2,C1,D1,E1,H1,I1,J1,K1	30 min to 10.49 h	20.8 min to 8.50 days	10.8 min to 15.5 h

TABLE V

Summary of Spectral Conditions, Irradiation Times, Cooling Times, and Counting Times for Zirconium, Niobium, Tantalum, Tungsten, and Lead

Irradiated Material	Spectral Conditions	Irradiation Times Range	Cooling Times Range	Counting Times Range
Zirconium	A1,A2,B1,B2,C1,D1,E1,H1,I1,K1,L1	30 min to 10.49 h	20.9 min to 7.74 days	10 min to 18.01 h
Niobium	A2,B2,C1,D1,E1,F1,G1,H1,I1,J1,K1,L1	30 min to 10.49 h	4.52 h to 6.93 days	28 min to 14.38 h
Tantalum	A1,B2,C1,H1,I1,K1,L1	9 h to 10.49 h	1.63 h to 7.71 days	16 min to 19.81 h
Tungsten	A1,A2,B1,B2,C1,F1,G1,H1,I1,K1	30 min to 10.49 h	20.6 min to 18.7 days	8.2 min to 18.38 h
Lead	C1,F1,G1,J1,L1	30 min to 10.49 h	11.5 min to 6.86 days	5.5 min to 14.30 h

Note that only the most prominent gamma peaks for a given emitter are included [see Fig. 4; in addition, 66 half-life (h) ^{99}Mo peak at 141 KeV carries a contribution from 6.02 h ^{99m}Tc too]. The error varies from 3.0% for ^{99}Mo(+^{99m}Tc) to 14.4% for 6.95 h ^{93m}Mo.

II.F. Highlights of Measured Data

Spectrum dependence of gamma emission rates is mostly seen in only those materials that have dominating isotopes resulting from (n,γ) reactions. High

TABLE VI

Summary of Spectral Conditions, Irradiation Times, Cooling Times, and Counting Times for Aluminum, Copper, Zinc, Silver, Indium, Tin

Irradiated Material	Spectral Conditions	Irradiation Times Range	Cooling Times Range	Counting Times Range
Aluminum	A1,A2,B1,B2,C1,D1,E1,F1,G1, H1,I1,J1,K1,L1	30 min to 10.49 h	58.3 min to 1.13 days	11.4 min to 10.4 h
Copper (also as Mn-Cu alloy)	A1,A2,B1,B2,K1	30 min to 10.49 h	12.3 min to 7.74 days	5.1 min to 6.75 h
Silver	C1,F1,G1,J1,L1	30 min to 10.49 h	33.3 min to 7.61 days	6.8 min to 19.09 h
Indium	A1,B2,C1,K1,L1	9 h to 10.49 h	37.4 min to 7.61 days	7 min to 14.76 h
Tin	C1,D1,E1,F1,G1,J1,L1	30 min to 10.49 h	21.8 min to 7.52 days	6.7 min to 17.28 h

threshold reactions, e.g., (n,n'), (n,p), $(n,n'p)$, (n,d), $(n,2n)$, are essentially governed by the harder part of the spectrum. Comparing the integrated gamma emission rates (between 100 KeV to 3 MeV), it is found that for a short irradiation time (30 min), Fe, AISI316, Al, and Co give the leading rates in that order. However, the trend changes for ~10 h irradiation to Al, Fe, and AISI316. This is understandable as the ^{24}Na (15 h) production rate was much below saturation during 30 min irradiation but came close to saturation during ~10 h irradiation.

Figure 5 is a plot of the equivalent, integrated (100 KeV to 3 MeV) decay gamma emission rate per second per gram versus Z of the sample for ~1-day cooling time in the Phases-IIC (location A alone) and -III experiments. A similar figure for ~1 week cooling time is available in Ref. 17. Equivalent Phase-III data are obtained by forcing the Nb decay gamma emission rate in this phase to be the same as that in Phase-IIC. The multiplier for the Phase-III data is 20. The Phase-III data take into account all experimental data available from Phases-IIIA and -IIIB. The irradiation time for all these cases is between 9 to 10 h. The emission rate is normalized to a source neutron intensity of 10^{12} n/s. One must emphasize that this kind of plot is a good indicator of the decay radioactivity property of a material for a given cooling time. Wherever possible, least-squares minimization was applied to interpolate/extrapolate data for a preselected cooling time, e.g., 1 day or 1 week, from the available experimental data sets. Otherwise, the experimental data are extrapolated peak by peak using known half-lives. For Phase-III, the extrapolation/interpolation is first done for each subphase, e.g., five locations of Phase-IIIA. Then, the mean and standard deviation on the mean are computed for the entire Phase-III data. Because of the differences in

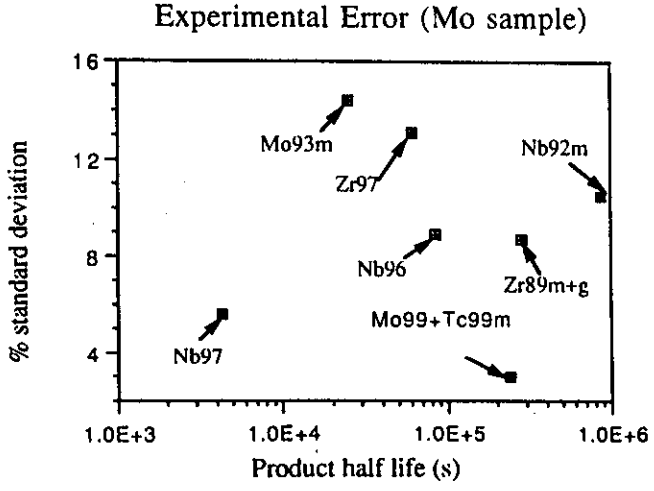

Fig. 4. Percent standard deviation on decay rates as a function of half-life for a molybdenum sample.

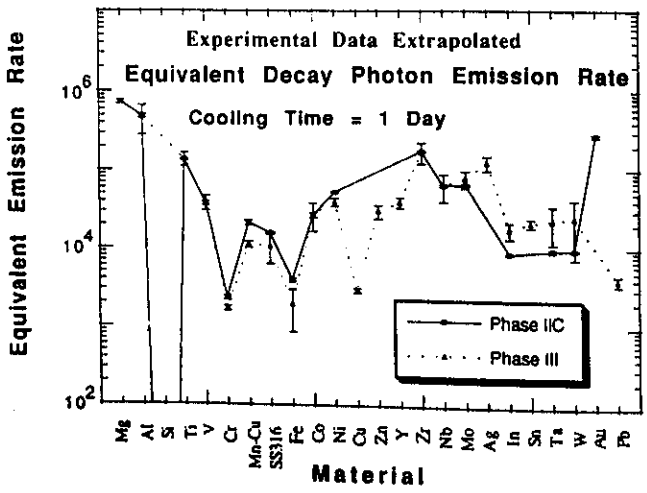

Fig. 5. Integrated decay gamma emission rate/g versus Z of sample for ~1-day cooling time.

the spectra, even for different locations in the same assembly, the standard deviation of the Phase-III extrapolated data is higher in general. The following observations are to be noted:

1. Broadly, the equivalent gamma emission rates from Phases-IIC and -III trace the same trend as a function of material for both cooling times (~1 day and ~1 week).

2. For a cooling time of 1 day, Mg has the largest emission rate. It is followed by Al, Au, Zr, Ti, Ag, Mo, Nb, Ni, V, and others. The Si activity is negligibly small.

3. For a cooling time of 1 week, Au has the largest emission rate. It is followed by Ag, Nb, Zr, Y, Co, Ti, Mo, Sn, Ni, In, Mn-Cu alloy, and others. The Si activity is infinitesimally small. Copper has the lowest decay gamma emission rate, apart from Si.

4. Although most of the gamma emission rates drop significantly as the cooling time increases from 1 day to 1 week, cobalt and yttrium have almost no change. Also, the decay rates in Nb, In, Cr, and Au drop much less readily compared with the others.

For some of the irradiated materials, the dominant contributors to the decay gamma emission rates are summarized as follows:

aluminum and magnesium: The ^{24}Na ($t_{1/2}$ = 15 h) dominated the decay gamma spectra at larger cooling times.

titanium: At short cooling times, 511-KeV annihilation gammas from ^{45}Ti (3.1 h) and ^{48}Sc (43.7 h) gammas dominate the measured emission rates. At longer cooling times, other contributors include ^{47}Sc (3.42 days) and ^{46}Sc (83.8 days).

vanadium: At shorter cooling times, ^{51}Ti (5.8 min) dominated the emission rate followed by ^{48}Sc (43.7 h). Also, ^{52}V (3.8 min) was observed. For longer cooling times, ^{48}Sc dominated the scene single handedly.

chromium: The 320-KeV gamma line from ^{51}Cr (27.7 days) dominates for long irradiation and cooling times. The NaCl and Fe/Mn impurities seem to be present as ^{24}Na (15 h), ^{35m}Cl (32 min), and ^{56}Mn (2.6 h) contribute as much as 3% to the total decay gamma emission rate for a cooling period of 1.5 h. For a cooling period of 15 h, only ^{24}Na contributes (<1%).

MnCu alloy: For shorter cooling times, ^{62}Cu (9.73 min, 511-KeV annihilation gammas) and ^{56}Mn (2.6 h) dominated the emission rate. However, their relative contributions varied depending on the hardness of the neutron energy spectrum, with ^{62}Cu dominating for the harder neutron spectrum. At larger cooling times, ^{54}Mn (312 days) dominates.

iron: For cooling times <10 h, ^{56}Mn ($t_{1/2}$ = 2.6 h) dominates. For larger cooling times, ^{54}Mn ($t_{1/2}$ = 312 days) assumes growing ascendancy. No significant neutron energy spectrum dependence was seen as both these products result from the high-threshold (n,p) reaction.

cobalt: For cooling periods of <5 h, ^{56}Mn, the product of the ^{59}Co$(n,\alpha)^{56}$Mn reaction, made the dominating contribution, as much as 95% for an irradiation period of 30 min and a cooling period of 37 min. The other contributing isotopes include ^{59}Fe (44.6 days), ^{58}Co (70.8 days), and ^{60}Co (5.3 yr); the last isotope was noticeable at locations having a larger component of softer neutrons.

nickel: The ^{62m}Co (13.9 min) and ^{57}Ni (36 h) dominate for short cooling times. The ^{58}Co (70.8 days), ^{57}Co (271 days), ^{57}Ni, ^{59}Fe (44.6 days), and ^{60}Co (5.3 yr) take over at larger cooling times.

molybdenum: The major contributors for short cooling times are ^{101}Mo (14.6 min), ^{101}Tc (14.2 min), ^{97}Nb (1.2 h), ^{98m}Nb (51 min), ^{99}Mo (66 h), ^{99m}Tc (6 h), ^{96}Nb (23.4 h), and ^{93m}Mo (6.9 h). The ^{101}Tc results from the beta decay of ^{101}Mo, and ^{99m}Tc is produced by the beta decay of ^{99}Mo. Longer cooling times see the dominance of ^{99}Mo, ^{99m}Tc, ^{96}Nb, ^{97}Nb, and ^{89}Zr.

stainless steel (Type 316 and AISI316): It is an alloy of Fe, Ni, Cr, Mn, and Mo. The ^{56}Mn contributes overwhelmingly at cooling times <1 day. At larger cooling times, ^{99}Mo, ^{99m}Tc, ^{51}Cr, ^{58}Co, ^{57}Ni, and ^{54}Mn are the leading contributors.

zinc: An annihilation peak at 511 KeV dominates at short cooling times. Other significant contributors include ^{63}Zn (38 min), ^{66}Cu (5.1 min), ^{69m}Zn (13.8 h), and ^{65}Ni (2.52 h). At larger cooling times, apart from the annihilation peak, the leading contributors are ^{69m}Zn, ^{67}Cu (61.9 h), ^{65}Zn (244 days), ^{64}Cu (12.7 h), and ^{65}Ni.

zirconium: The ^{89}Zr (78.4 h), ^{87m}Sr (2.8 h), ^{90m}Y (3.2 h), ^{94}Y (18.7 min), ^{92}Y (3.5 h), and ^{91}Sr (9.5 h) contribute for short cooling times. Larger cooling times bring into focus the predominance of ^{89}Zr and ^{90m}Y (3.2 h).

silver: At short cooling times, a peak at 511 to 512 KeV dominates. This peak gets large contributions from ^{106}Ag (24 min), ^{106m}Rh (130 min), and ^{106m}Ag (8.5 days). At larger cooling times, a large number of gamma lines from ^{106m}Ag dominate the emission rate.

tin: At shorter cooling times, ^{123m}Sn (40 min) dominates. Other contributors include ^{117}In (42.3 min), ^{116m1}In (54.1 min), ^{117}In (1.93 h), ^{111}In (2.8 days), and ^{117m}Sn (14 days). At larger cooling times, ^{117m}Sn dominates.

tantalum: The ^{180m}Ta (8 h), ^{180m}Hf (5.5 h), and ^{182}Ta (115 days) dominate the gamma emission rate.

tungsten: The ^{187}W (23.9 h), ^{186}Ta (10.5 min), and ^{183}Hf (64 min) dominate short cooling times. For larger cooling times, the predominant contributor ^{187}W is backed up by ^{183}Ta (5 days) and ^{182}Ta (115 days).

lead: The ^{203}Pb (52 h) and ^{204m}Pb (67 min) dominate at shorter cooling times; ^{203}Pb dominates at larger cooling times.

III. FEATURES OF EARLIER ANALYSIS

III.A. Approach

As shown in Ref. 10 (see Fig. 2 there), the usual analysis to calculate the decay gamma emission rate involves a multistep procedure. A two- or three-dimensional transport code is employed to get the neutron energy distribution, i.e., the neutron flux, at spatial locations of the samples. The geometry and material composition of the irradiation environment are important inputs for this calculation. The next stage involves the computation of the decay gamma emission spectrum using a radioactivity calculation code. Neutron flux, sample composition, irradiation, and cooling (or shutdown) times are required input data for this stage. Decay and activation cross-section libraries form part of the code used. The codes used for this purpose have included DKR-ICF, REAC, RACC, and THIDA-2. In fact, THIDA-2 is a code system that includes neutron flux–calculating modules too. However, its central module is ACT4, which calculates induced radioactivity and associated quantities.

Two calculational schemes were followed for the analysis. The first scheme was related to the use of the externally evaluated neutron flux with four radioactivity codes: DKRICF, REAC, RACC, and ACT4. The flux was obtained in a two-step process. First, the source neutron energy and the angular distribution were obtained[28] by three-dimensional MCNP modeling of RNT of the FNS facility. Second, the source neutron distribution from MCNP was input to the RUFF (Ref. 29) and DOT4.3 (Ref. 30) code systems to compute the spatial distribution of the neutron flux. The 30-group MATXS5 cross-section library (based on ENDF/B-V) of Los Alamos National Laboratory[31] (LANL) was used for neutron transport. The second calculational scheme was similar to the one in Ref. 32 wherein the THIDA code was employed for a whole analysis.

III.B. Spectral Conditions

Figure 6 shows the computed neutron energy spectra per unit lethargy as a function of neutron energy in Phases-IIC through -IIIB for 5 typical locations, e.g., A, B, C, H, and K out of a total of 14 (A through N). The remaining spectra are not shown for fear of overcrowding the figure. The calculations show that >95% of the neutrons lie above 0.1 MeV for positions A, C, and D; and E, B, and I have the lowest fraction of neutrons above 0.1 MeV; i.e., only 66% of the neutrons lie above 0.1 MeV. For locations F, G, H, J, and L, 70 to 80% of the neutrons lie above 0.1 MeV. It is evident that the neutron energy spectrum is quite hard for most of these locations.

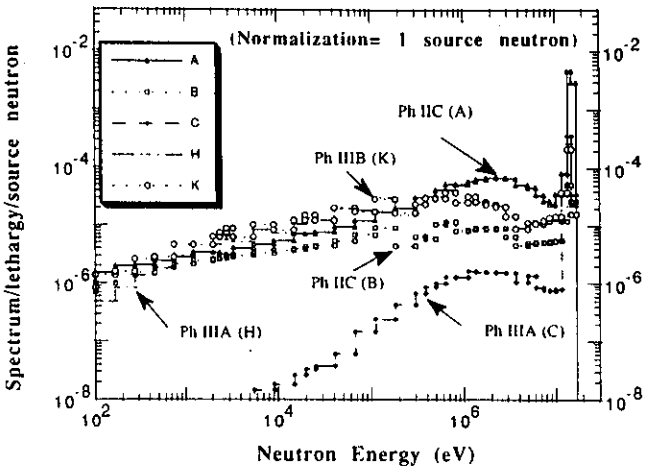

Fig. 6. Computed neutron energy spectra per unit lethargy as a function of neutron energy in Phases-IIC through -IIIB for five locations A, B, C, H, and K.

III.C. Trends of Results

The results of the comparison of the integrated, from 100 KeV through 3 MeV of the gamma energy, decay gamma emission rates were presented and discussed in earlier publications.[8-13,17] The computed results from REAC-2, DKR-ICF, RACC, and THIDA-2 were included. Large deviations in the calculated-to-experiment (C/E) ratio were observed for Si, Ti, V, Cr, MnCu alloy, Co, Zn, Zr, Mo, Ag, In, Sn, Ta, W, and $YBa_2Cu_3O_7$. For example, C/E for W ranged from 0.0005 to 300, depending on the radioactivity code, neutron flux, irradiation, and cooling times. The results of the comparison of the isotopic activities of the irradiation products were also discussed earlier.[8-13,17] Although the C/E ratios for the integrated decay-gamma emission rates for Fe, Ni, and Type 316 stainless steel, among others, generally behaved quite well, large discrepancies were seen for the isotopic activities for even these materials.[8-13,17] For example, for irradiated Ni samples, C/E ranged from 0.2 to 1.4 for ^{57}Co, 0.6 to 1.9 for ^{58}Co, and 0.6 to 2.8 for ^{60}Co.

III.D. Problems with Multiplicity of Impacting Parameters

The observed discrepancies between the measured and the computed values of the decay gamma emission rates could be traced to the following components: experimental error, calculational error, and presence of

contributions from unspecified impurities in the irradiated samples. The factors contributing to the experimental error were already discussed earlier. In addition, the experimental data may be marked by the absence of those gamma peaks that suffer from poor counting statistics. Also, at times, there may be interference from background gammas. Thus, for a radioactive product emitting multiple gammas, the experimental data may not contain contributions from all of them. The factors contributing to the calculational error could be (a) the neutron energy spectrum, (b) the half-lives of the products, (c) the decay gamma yields of the isotopic products, (d) the activation cross sections, and (e) the solution algorithm of the radioactivity code being used. The calculated neutron energy spectrum is subject to error due to deficiencies in transport cross sections on one hand and numerical/statistical/modeling errors on the other. Generally, the energy group structures used in the transport and the radioactivity calculations are different. The conversion of the neutron spectrum from one structure to another might lead to additional error.

Erroneous or outdated decay data libraries of the radioactivity codes would be responsible for factors (b) and (c). One must highlight that error in half-life of a radioactive product will make an important contribution to the calculation. As a result, C/E will be erroneous too. Trends of the impact of error in the half-life on C/E for isotopic activity are traced in Figs. 7 and 8. The reference half-life is the correct half-life that is actually controlling the build-up/decay of isotopic activity as a function of irradiation/cooling time. Both irradiation time, *tr*, and cooling time, *tw*, have been expressed in units of the reference half-life. An erroneous half-life is assumed to be used in a radioactivity calculation. The trends shown in the figures apply only to the products

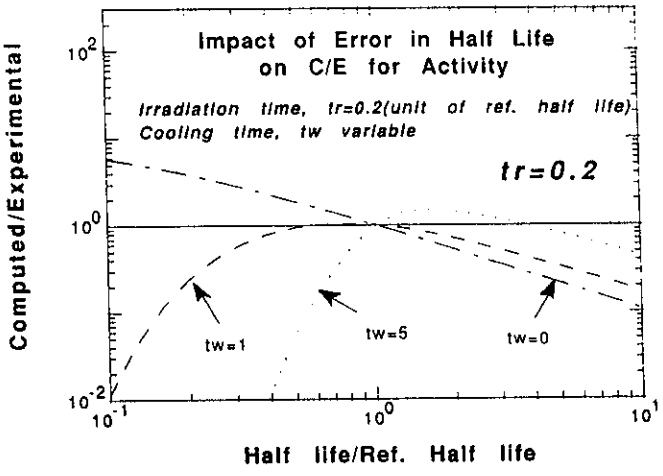

Fig. 7. Impact of error in half-life with respect to reference half-life on ratio of computed to experimentally measured activity of an isotopic product, irradiation time = 0.2 × reference half-life, and cooling time (expressed in unit of reference half-life) is a variable.

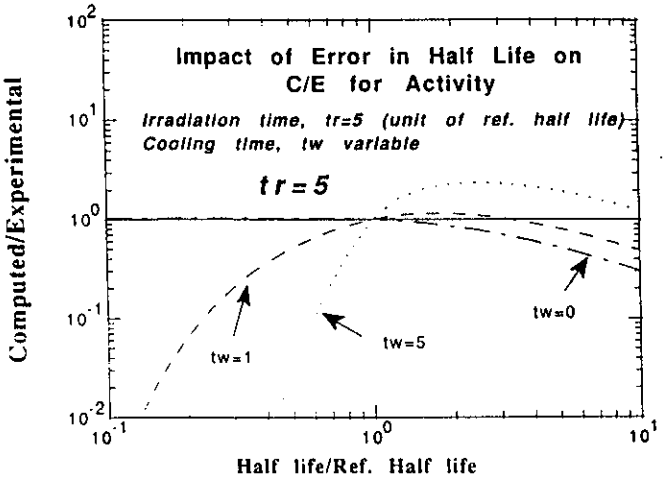

Fig. 8. Impact of error in half-life with respect to reference half-life on ratio of computed to experimentally measured activity of an isotopic product, irradiation time = 5.0 × reference half-life, and cooling time (expressed in unit of reference half-life) is a variable.

generated in a single-step process. In the figures, whereas "computed" represents the calculation of activity with an erroneous half-life, "experimental" stands for the calculation with the reference half-life. As is quite evident, one can underestimate as well as overestimate the activity depending on the combination of governing parameters of half-life, irradiation time, and cooling time. Thus, while comparing different cross-section libraries, it is important to use the same half-life for each isotope to ensure that there is no relative bias introduced in a C/E by one or the other library due to this factor. Of course, it does not rule out the possibility that the reference half-life itself is off. If this be the case, C/Es by all libraries will have a systematic bias for underprediction or overprediction.

Deficient activation cross-section libraries of the radioactivity codes would be responsible for factor (d). Finally, the method of solution implemented in the radioactivity code might lead to an error in certain situations [factor (e)]. It is obvious from the plurality of the contributing factors to the calculational error that it is required to do a deeper analysis by restricting the number of the impacting parameters as much as possible, if one wants to form a substantive judgment as to the quality/status of the decay data library, the activation cross-section library, or the solution algorithm of a radioactivity code under study.

IV. CURRENT ANALYTICAL PROCEDURE

IV.A. Rationale and Strategy

Figure 9 shows the steps followed in computing decay gamma emission rates using the current procedure.

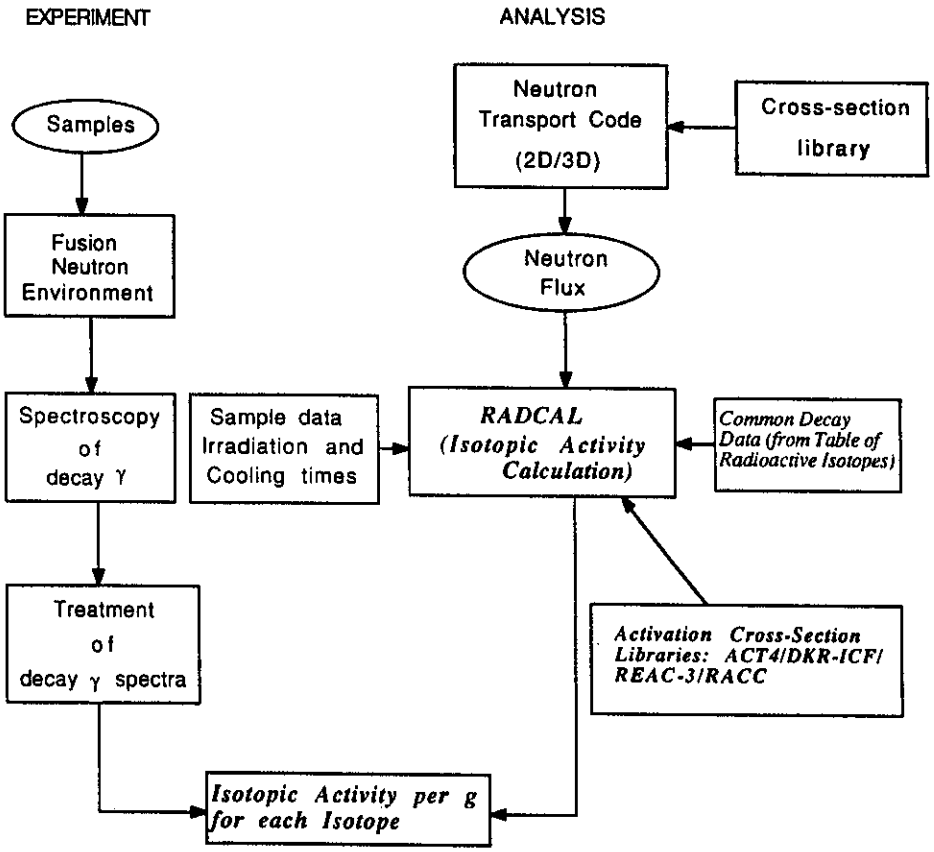

Fig. 9. Flowchart of isotopic activity comparison procedure.

This differs from the earlier analysis at the critical step of calculation of radioactivity. The isotopic decay gamma emission rates are calculated by the RADCAL common module using activation cross-section data from the ACT4, REAC-3, DKR-ICF, and RACC data libraries. The decay data are taken from Ref. 22. The solution algorithm implemented in RADCAL is close to the one followed in DKR-ICF, but it is less general and designed with an eye to deal with experimental exigencies. The decay gamma emission rates computed using RADCAL for the entire range of experimental conditions of interest were found to be the same as those calculated by other codes, provided identical decay and cross-section data were used. It is not intended as a replacement for a radioactivity code. Basically, the intention has been to provide a tool that can help in comparing directly the relative performance of the activation cross-section libraries used by the radioactivity codes under consideration.

IV.B. Reactions Covered

Tables VII through XIII list reactions/decays leading to the production of the observed isotopic products for different materials. Impurities are not considered. There are more than 250 reactions leading to the production of more than 80 radioactive isotopes. These tables also show if these cross sections are included in ACT4, REAC-3, DKR-ICF, and RACC. The REAC-3 library covers all the reactions; RACC covers the least number of reactions. When comparing different cross-section libraries for a given nuclear reaction, one needs to look at not only their detailed energy-wise dependence but also their integrated behavior over the entire energy range of interest. For quantifying integrated behavior, we define a quantity, called cross-sectional integral (CSI), as follows:

$$\mathrm{CSI} = \int_{u_{min}}^{u_{max}} \sigma(u)\, du \ ,$$

where $\sigma(u)$ is the microscopic activation cross section at lethargy u and is expressed in barns. The u_{min} and u_{max}, respectively, define the lowest and the highest lethargies of interest. The highest neutron energy is taken as 14.92 MeV. The lowest energy of interest is the lower energy boundary of the lowest neutron energy group where the cross section is nonzero. The CSI is given in barns. The physical significance of CSI for a reaction lies in the fact that for a flat neutron energy spectrum, it is directly proportional to the energy-integrated reaction rate for that reaction. However,

TABLE VII

Status of Cross Sections of Reactions Leading to Production of Radioactive Isotopes in Titanium, Vanadium, and Chromium

Material	Radioactive Isotope (Product)	Contributing Reactions	Status of Reaction Cross Sections in Libraries of the Four Codes[a]			
			ACT4	REAC-3	DKR-ICF	RACC
Titanium	$^{51}Ti^{b}$	$^{50}Ti(n,\gamma)^{51}Ti$	p	p	p	a
	$^{45}Ti^{b}$	$^{46}Ti(n,2n)^{45}Ti$	p	p	p	p
	$^{44}Sc^{b}$	$^{46}Ti(n,t)^{44}Sc$	z	p	p	a
	^{48}Sc	$^{48}Ti(n,p)^{48}Sc$	p	p	p	p
		$^{49}Ti(n,np)^{48}Sc$	p	p	p	a
		$^{48}Ti(n,d)^{48}Sc$	a	p	a	p
		$^{50}Ti(n,t)^{48}Sc$	a	p	a	a
	^{47}Sc	$^{47}Ti(n,p)^{47}Sc$	p	p	p	p
		$^{48}Ti(n,np)^{47}Sc$	p	p	p	a
		$^{48}Ti(n,d)^{47}Sc$	z	p	a	p
		$^{49}Ti(n,t)^{47}Sc$	a	p	p	a
	^{47}Ca	$^{50}Ti(n,\alpha)^{47}Ca$	p	p	p	p
	^{46}Sc	$^{46}Ti(n,p)^{46}Sc$	p	p	p	p
		$^{47}Ti(n,np)^{46}Sc$	p	p	p	a
		$^{47}Ti(n,d)^{46}Sc$	a	p	a	p
		$^{48}Ti(n,t)^{46}Sc$	a	p	a	a
Vanadium	^{52}V	$^{51}V(n,\gamma)^{52}V$	p	p	p	p
	^{51}Ti	$^{51}V(n,p)^{51}Ti$	p	p	p	p
	^{48}Sc	$^{51}V(n,\alpha)^{48}Sc$	p	p	p	p
	$^{47}Sc^{b}$	$^{50}V(n,\alpha)^{47}Sc$	p	p	p	p
		$^{51}V(n,n'a)^{47}Sc$	p	p	p	p
Chromium	^{49}Cr	$^{50}Cr(n,2n)^{49}Cr$	p	p	p	p
	^{51}Cr	$^{52}Cr(n,2n)^{51}Cr$	p	p	p	p
		$^{50}Cr(n,\gamma)^{51}Cr$	p	p	p	p

[a]The p stands for present, a for absent, and z for zero values for cross sections.
[b]Not observed in main experiments.

when for a given nuclear reaction, one compares CSIs from different cross-section libraries, it is imperative to compare the cross-section shapes as a function of neutron energy before inferring the relative quality of the cross sections. Tables XIV through XVII compare CSIs for a few select reactions, as computed for the four libraries. Practically, all the materials of interest to fusion reactor designers have discrepant cross-sectional representations in the libraries of the four codes. For some reactions, CSIs computed using ENDF/B-VI/JENDL-3/JEF-2 are also listed for making comparisons. Doubtless, REAC-3 has the most complete library; RACC has the least complete library. Almost all kinds of reactions, i.e., $(n,2n)$, (n,p), (n,γ), etc., show discrepancies among the libraries.

IV.C. Impact of Energy Group Structure on Reaction Rate Calculations

Ideally, one would like to have a very large number of energy groups to characterize each activation cross section as a function of neutron energy in the entire range of interest. This is desirable for representing all fine features of the cross sections. Also, it would be very helpful in minimizing errors in computing reaction rates due to flux weighting used for generating grouped cross-section sets; the flux weighting may not represent the actual neutron energy spectrum shape for an experimental situation at hand. However, practical considerations related to excessive memory requirements and exorbitant calculational time for the neutron energy spectrum restrict the number of energy groups.

The energy group structures used in the activation cross-section libraries of different codes are generally different. In addition, the energy group structures used in the transport calculations of the neutron energy spectrum and those of the activation cross sections (in radioactivity codes) may not be identical. In this event, one needs to convert the neutron energy spectrum. To summarize, we find it of interest to understand the two contributions to errors in the calculation of the reaction rate: that due to a limited number of energy groups

TABLE VIII

Status of Cross Sections of Reactions Leading to Production of Radioactive Isotopes in Silicon, Manganese, Iron, Cobalt, and Nickel

Material	Radioactive Isotope (Product)	Contributing Reactions	Status of Reaction Cross Sections in Libraries of the Four Codes[a]			
			ACT4	REAC-3	DKR-ICF	RACC
Silicon	^{29}Al	^{29}Si$(n,p)^{29}$Al	p	p	p	p
		^{30}Si$(n,np)^{29}$Al	p	p	a	a
	^{27}Mg	^{30}Si$(n,\alpha)^{27}$Mg	p	p	p	p
Manganese	^{52}V	^{55}Mn$(n,\alpha)^{52}$V	p	p	p	p
	^{56}Mn	^{55}Mn$(n,\gamma)^{56}$Mn	p	p	p	p
	^{54}Mn	^{55}Mn$(n,2n)^{54}$Mn	p	p	p	p
Iron	^{53}Fe	^{54}Fe$(n,2n)^{53}$Fe	p	p	p	p
	^{56}Mn	^{56}Fe$(n,p)^{56}$Mn	p	p	p	p
		^{57}Fe$(n,np)^{56}$Mn	p	p	p	a
		^{57}Fe$(n,d)^{56}$Mn	z	p	a	p
		^{58}Fe$(n,t)^{56}$Mn	a	p	p	p
	^{51}Cr	^{54}Fe$(n,\alpha)^{51}$Cr	p	p	p	p
	^{59}Fe	^{58}Fe$(n,\gamma)^{59}$Fe	p	p	p	p
	^{54}Mn	^{54}Fe$(n,p)^{54}$Mn	p	p	p	p
Cobalt	^{56}Mn	^{59}Co$(n,\alpha)^{56}$Mn	p	p	p	p
	^{59}Fe	^{59}Co$(n,p)^{59}$Fe	p	p	p	p
	^{58}Co	^{59}Co$(n,2n)^{58}$Co	p	p	p	p
		^{59}Co$(n,2n)^{58m}$Co $\rightarrow$ ^{58}Co	p	p	p	a
	^{60}Co	^{59}Co$(n,\gamma)^{60}$Co	p	p	p	p
		^{59}Co$(n,\gamma)^{60m}$Co $\rightarrow$ ^{60}Co	p	p	p	a
Nickel	^{62m}Co	^{62}Ni$(n,p)^{62m}$Co	p	p	p	a
	^{65}Ni	^{64}Ni$(n,\gamma)^{65}$Ni	p	p	p	p
	^{57}Ni	^{58}Ni$(n,2n)^{57}$Ni	p	p	p	p
	^{59}Fe	^{62}Ni$(n,\alpha)^{59}$Fe	p	p	p	p
		^{60}Ni$(n,2p)^{59}$Fe	a	p	a	a
	^{58}Co	^{58}Ni$(n,p)^{58}$Co	p	p	p	p
		^{58}Ni$(n,p)^{58m}$Co $\rightarrow$ ^{58}Co	p	p	p	a
		^{58}Ni$(n,np)^{57}$Co	p	p	p	a
	^{57}Co	^{58}Ni$(n,d)^{57}$Co (also ^{57}Ni $\rightarrow$ ^{57}Co)	a	p	a	p
	^{60}Co	^{60}Ni$(n,p)^{60}$Co	p	p	p	p
		^{61}Ni$(n,np)^{60}$Co	p	p	p	a
		^{61}Ni$(n,d)^{60}$Co	p	p	a	p
		^{62}Ni$(n,t)^{60}$Co	a	p	p	p
		^{60}Ni$(n,p)^{60m}$Co $\rightarrow$ ^{60}Co	p	p	p	p
		^{61}Ni$(n,np)^{60m}$Co $\rightarrow$ ^{60}Co	a	p	a	a
		^{61}Ni$(n,d)^{60m}$Co $\rightarrow$ ^{60}Co	a	p	a	a

[a]The p stands for present, a for absent, and z for zero values for cross sections.

for representation of activation cross sections[33,34] and that due to the conversion of the neutron energy spectrum from one group structure to another. We assume here that there is no uncertainty in computing the neutron energy spectrum for the original group structure. Also, we confine ourselves to threshold activation cross sections, even though the errors for the capture reactions may show quite different trends. A set of ten activation cross-section shapes with varying thresholds from 0.1 to 14 MeV are shown in Fig. 10. These shapes were characterized by simple expressions. We confine ourselves to neutron energy above 0.1 MeV. Four energy group structures are considered: 125 groups,[17] 63 groups (REAC-3), 46 groups (DKR-ICF/RACC), and 42 groups (ACT4). Multigroup cross sections were obtained by flux weighting over a reference spectrum shape shown in Fig. 11. This figure also shows four additional spectral shapes. The reaction rates were obtained for

TABLE IX

Status of Cross Sections of Reactions Leading to Production of Radioactive Isotopes in Molybdenum

Material	Radioactive Isotope (Product)	Contributing Reactions	Status of Reaction Cross Sections in Libraries of the Four Codes[a]			
			ACT4	REAC-3	DKR-ICF	RACC
Molybdenum	^{101}Tc	^{100}Mo$(n,\gamma)^{101}$Mo → ^{101}Tc	p	p	p	p
	^{101}Mo	^{100}Mo$(n,\gamma)^{101}$Mo	p	p	p	p
	^{91}Mo	^{92}Mo$(n,2n)^{91}$Mo	p	p	p	p
		^{92}Mo$(n,2n)^{91m}$Mo → ^{91}Mo	p	p	a	a
	^{98m}Nb	^{98}Mo$(n,p)^{98m}$Nb	p	p	a	a
		^{100}Mo$(n,t)^{98m}$Nb	a	p	a	a
		^{100}Mo$(n,nd)^{98m}$Nb	a	p	a	a
	^{97}Nb	^{97}Mo$(n,p)^{97}$Nb	p	p	p	p
		^{98}Mo$(n,np)^{97}$Nb	p	p	p	a
		^{98}Mo$(n,d)^{97}$Nb (& ^{97}Zr → ^{97m}Nb → ^{97}Nb)	p	p	a	p
	^{93m}Mo	^{94}Mo$(n,2n)^{93m}$Mo	p	p	p	a
		^{92}Mo$(n,\gamma)^{93m}$Mo	p	p	a	a
	^{96}Nb	^{96}Mo$(n,p)^{96}$Nb	p	p	p	p
		^{97}Mo$(n,np)^{96}$Nb	p	p	p	a
		^{97}Mo$(n,d)^{96}$Nb	a	p	a	p
		^{98}Mo$(n,t)^{96}$Nb	a	p	p	p
	^{99}Mo	^{100}Mo$(n,2n)^{99}$Mo	p	p	p	p
		^{98}Mo$(n,\gamma)^{99}$Mo	p	p	p	p
	^{89}Zr	^{92}Mo$(n,\alpha)^{89}$Zr	p	p	p	p
		^{92}Mo$(n,\alpha)^{89m}$Zr → ^{89}Zr	p	p	a	a
	^{95m}Nb	^{95}Mo$(n,p)^{95m}$Nb	p	p	p	p
		^{96}Mo$(n,np)^{95m}$Nb	p	p	a	a
		^{96}Mo$(n,d)^{95m}$Nb	a	p	a	a
		^{97}Mo$(n,t)^{95m}$Nb	a	p	a	a
		^{98}Mo$(n,nt)^{95m}$Nb (also ^{95}Zr → ^{95m}Nb)	a	p	a	a
	^{92m}Nb	^{92}Mo$(n,p)^{92m}$Nb	p	p	p	p
	^{95}Nb	^{95}Mo$(n,p)^{95}$Nb	p	p	p	p
		^{96}Mo$(n,np)^{95}$Nb	p	p	p	a
		^{96}Mo$(n,d)^{95}$Nb	a	p	a	p
		^{97}Mo$(n,t)^{95}$Nb	a	p	p	p
		^{98}Mo$(n,nt)^{95}$Nb (also ^{95m}Nb → ^{95}Nb)	a	p	a	a
	^{91}Nb	(^{91}M→ ^{91}Nb)				
	^{95}Zr	^{98}Mo$(n,\alpha)^{95}$Zr	p	p	p	p
	^{88}Zr	^{92}Mo$(n,na)^{88}$Zr	p	p	p	p

[a]The p stands for present, a for absent, and z for zero values for cross sections.

each of the five spectral shapes for the four group structures for all the reaction cross-section shapes. In addition, the reaction rate was also obtained by integration of the product of flux (continuous spectrum shape) and the cross section over the entire energy range for each of the ten cross sections. This reaction rate is exact and is termed ideal (or reference). The reaction rates for all the multigroup cases are normalized with respect to the ideal values for each cross-section shape. Figure 12 shows the normalized reaction rates as a function of

TABLE X

Status of Cross Sections of Reactions Leading to Production of Radioactive Isotopes in Zirconium, Niobium, and Tantalum

Material	Radioactive Isotope (Product)	Contributing Reactions	Status of Reaction Cross Sections in Libraries of the Four Codes[a]			
			ACT4	REAC-3	DKR-ICF	RACC
Zirconium	^{94}Y	^{94}Zr$(n,p)^{94}$Y	p	p	p	p
		^{96}Zr$(n,t)^{94}$Y	a	p	p	p
	^{91m}Y	^{91}Zr$(n,p)^{91m}$Y	p	p	p	p
		^{92}Zr$(n,np)^{91m}$Y	p	p	a	a
		^{92}Zr$(n,d)^{91m}$Y	a	p	a	a
	^{87m}Sr	^{90}Zr$(n,\alpha)^{87m}$Sr	p	p	a	a
		^{91}Zr$(n,na)^{87m}$Sr	a	p	a	a
	^{90m}Y	^{90}Zr$(n,p)^{90m}$Y	p	p	p	p
		^{91}Zr$(n,np)^{90m}$Y	p	p	a	a
		^{91}Zr$(n,d)^{90m}$Y	a	p	a	a
		^{92}Zr$(n,nd)^{90m}$Y	a	p	a	a
	^{92}Y	^{92}Zr$(n,p)^{92}$Y	p	p	p	p
		^{94}Zr$(n,t)^{92}$Y	a	p	p	p
	^{91}Sr	^{94}Zr$(n,\alpha)^{91}$Sr	p	p	p	p
	^{97}Zr	^{96}Zr$(n,\gamma)^{97}$Zr	p	p	a	a
	^{97}Nb	^{96}Zr$(n,\gamma)^{97}$Zr $\rightarrow$ ^{97}Nb	p	p	a	a
	^{89}Zr	^{90}Zr$(n,2n)^{89}$Zr	p	p	p	p
		^{90}Zr$(n,2n)^{89m}$Zr $\rightarrow$ ^{89}Zr	p	p	p	p
	^{95}Zr	^{96}Zr$(n,2n)^{95}$Zr	p	p	p	p
		^{94}Zr$(n,\gamma)^{95}$Zr	p	p	p	p
Niobium	^{90m}Y	^{93}Nb$(n,\alpha)^{90m}$Y	p	p	a	a
	^{92m}Nb	^{93}Nb$(n,2n)^{92m}$Nb	p	p	p	p
Tantalum	^{180m}Hf	^{180}Ta$(n,p)^{180m}$Hf	a	p	p	a
		^{181}Ta$(n,np)^{180m}$Hf	a	p	a	a
		^{181}Ta$(n,d)^{180m}$Hf	a	p	a	a
	^{180m}Ta	^{181}Ta$(n,2n)^{180m}$Ta	p	p	p	a
	^{181}Hf	^{181}Ta$(n,p)^{181}$Hf	p	p	p	a
	^{182}Ta	^{181}Ta$(n,\gamma)^{182}$Ta	p	p	p	p
		^{181}Ta$(n,\gamma)^{182m}$Ta $\rightarrow$ ^{182}Ta	p	p	p	a

[a]The p stands for present, a for absent, and z for zero values for cross sections.

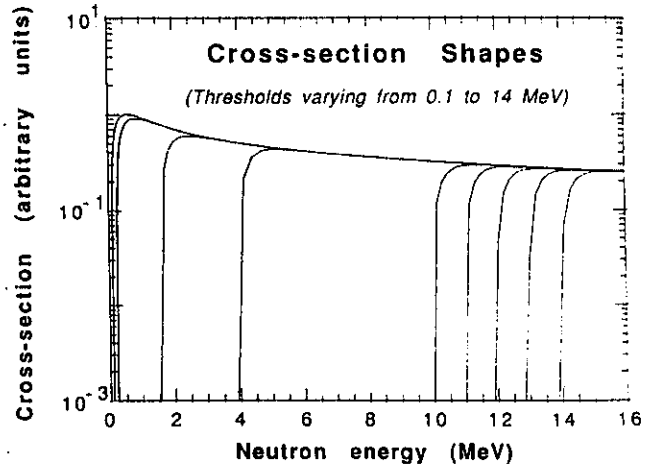

Fig. 10. Assumed shapes of activation cross section for thresholds varying from 0.1 to 14 MeV.

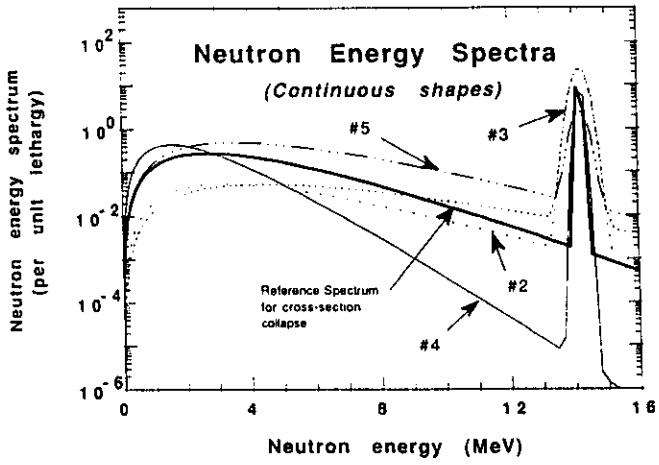

Fig. 11. Test neutron energy spectra including reference neutron energy spectrum.

TABLE XI

Status of Cross Sections of Reactions Leading to Production of Radioactive Isotopes in Copper, Tungsten, and Lead

Material	Radioactive Isotope (Product)	Contributing Reactions	Status of Reaction Cross Sections in Libraries of the Four Codes[a]			
			ACT4	REAC-3	DKR-ICF	RACC
Copper	^{64}Cu	^{65}Cu$(n,2n)^{64}$Cu	p	p	p	p
		^{63}Cu$(n,\gamma)^{64}$Cu	p	p	p	p
	^{62m}Co	^{65}Cu$(n,\alpha)^{62m}$Co	p	p	p	p
	^{65}Ni	^{65}Cu$(n,p)^{65}$Ni	p	p	p	a
	^{60}Co	^{63}Cu$(n,\alpha)^{60}$Co	p	p	p	p
		^{63}Cu$(n,\alpha)^{60m}$Co $\rightarrow$ ^{60}Co	p	p	a	a
Tungsten	^{186}Ta	^{186}W$(n,p)^{186}$Ta	p	p	a	a
	^{182m}Ta	^{182}W$(n,p)^{182m}$Ta	a	p	a	a
		^{183}W$(n,np)^{182m}$Ta	z	p	a	a
		^{183}W$(n,d)^{182m}$Ta	a	p	a	a
		^{184}W$(n,t)^{182m}$Ta	a	p	a	a
	^{183}Hf	^{186}W$(n,\alpha)^{183}$Hf	p	p	p	p
	^{184}Ta	^{184}W$(n,p)^{184}$Ta	p	p	p	p
	^{187}W	^{186}W$(n,\gamma)^{187}$W	p	p	p	p
	^{183}Ta	^{183}W$(n,p)^{183}$Ta	p	p	p	p
		^{184}W$(n,np)^{183}$Ta	p	p	p	a
		^{184}W$(n,d)^{183}$Ta (also ^{183}Hf $\rightarrow$ ^{183}Ta)	z	p	a	p
	^{182}Ta	^{182}W$(n,p)^{182}$Ta	p	p	p	p
		^{183}W$(n,np)^{182}$Ta	p	p	p	a
		^{183}W$(n,d)^{182}$Ta	a	p	a	p
		^{184}W$(n,t)^{182}$Ta (also ^{182m}Ta $\rightarrow$ ^{182}Ta)	a	p	a	a
Lead	^{204m}Pb	^{204}Pb$(n,n')^{204m}$Pb	a	p	a	a
		^{206}Pb$(n,3n)^{204m}$Pb	a	p	a	a
	^{203}Pb	^{204}Pb$(n,2n)^{203}$Pb	p	p	a	a

[a]The p stands for present, a for absent, and z for zero values for cross sections.

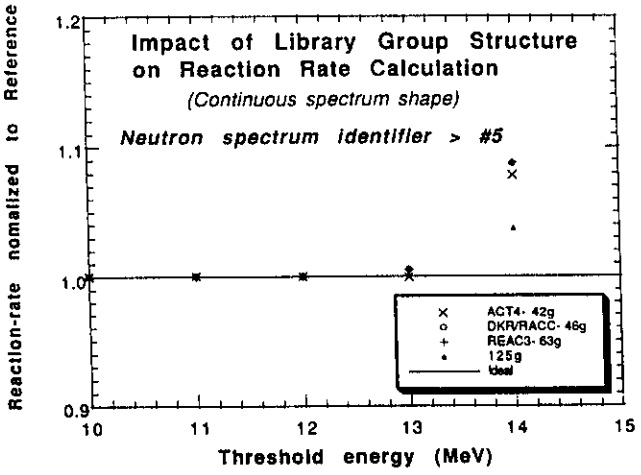

Fig. 12. Normalized reaction rates as a function of threshold energy for test shape 5.

threshold for shape 5. The behavior for the other shapes parallels that for shape 5. The largest discrepancy is <10%. As for the effect of spectral shapes and the cross-section threshold, the largest deviation is seen for the 14-MeV threshold and for the softer spectra. Shape 4 represents a dominant 14.2-MeV peak, and the largest discrepancy (for the 14-MeV threshold) is <4%.

The impact of flux conversion from one group structure to another is studied next. The original group structure has 125 groups. Three spectral shapes, i.e., A, B, and L, are shown in Fig. 13. Spectrum A is the hardest one; L is the softest one. All the reaction rates are normalized with respect to the reference group structure of 125 groups. For shapes A and B, the normalized reaction rates deviate significantly from 1 for the 14-MeV threshold only. The rates drop as low as 0.5. The trends are quite different for shape L, however. Figure 14 shows the normalized reaction rates for

TABLE XII

Status of Cross Sections of Reactions Leading to Production of Radioactive Isotopes in Aluminum, Zinc, and Indium

Material	Radioactive Isotope (Product)	Contributing Reactions	Status of Reaction Cross Sections in Libraries of the Four Codes[a]			
			ACT4	REAC-3	DKR-ICF	RACC
Aluminum	^{27}Mg	^{27}Al$(n,p)^{27}$Mg	p	p	p	p
	^{24}Na	^{27}Al$(n,\alpha)^{24}$Na	p	p	p	p
Zinc	^{63}Zn	^{64}Zn$(n,2n)^{63}$Zn	p	p	p	p
	^{65}Ni	^{68}Zn$(n,\alpha)^{65}$Ni	p	p	p	p
	^{64}Cu	^{64}Zn$(n,p)^{64}$Cu	p	p	p	p
	^{69m}Zn	^{70}Zn$(n,2n)^{69m}$Zn	p	p	p	a
		^{68}Zn$(n,\gamma)^{69m}$Zn	p	p	p	p
	^{67}Cu	^{67}Zn$(n,p)^{67}$Cu	p	p	p	p
		^{68}Zn$(n,np)^{67}$Cu	a	p	p	a
		^{68}Zn$(n,d)^{67}$Cu	a	p	a	a
	^{65}Zn	^{66}Zn$(n,2n)^{65}$Zn	p	p	p	p
		^{64}Zn$(n,\gamma)^{65}$Zn	p	p	p	p
Indium	^{112m}In	^{113}In$(n,2n)^{112m}$In	p	p	a	a
	^{112}In	^{113}In$(n,2n)^{112}$In (also ^{112m}In → ^{112}In)	p	p	p	a
	^{116m}In	^{115}In$(n,\gamma)^{116m}$In	p	p	p	a
	^{113m}In	^{113}In$(n,n')^{113m}$In	p	p	a	a
	^{112}Ag	^{115}In$(n,\alpha)^{112}$Ag	p	p	p	a
	^{115m}In	^{115}In$(n,n')^{115m}$In	a	p	a	a
		^{115}In$(n,p)^{115}$Cd → ^{115m}In	p	p	p	a
		^{115}In$(n,p)^{115m}$Cd → ^{115m}In	a	p	a	a
	^{115}Cd	^{115}In$(n,p)^{115}$Cd	p	p	p	a
	^{114m}In	^{115}In$(n,2n)^{114m}$In	a	p	p	a
		^{113}In$(n,\gamma)^{114m}$In	p	p	p	a
	^{114}In	^{115}In$(n,2n)^{114}$In	a	p	p	a
		^{113}In$(n,\gamma)^{114}$In (also ^{114m}In → ^{114}In)	p	p	p	a

[a]The p stands for present, a for absent, and z for zero values for cross sections.

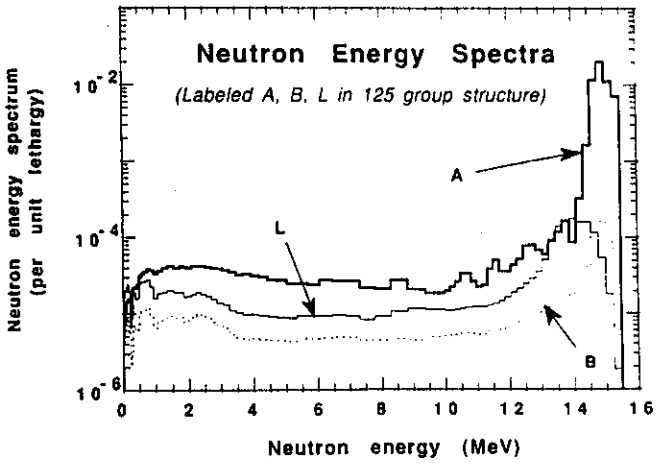

Fig. 13. Three test spectral shapes, A, B, and L, considered for flux conversion study.

shape L. For this shape, the reaction rates start showing large discrepancies for the 12-MeV threshold itself. There is no definite trend for one or the other group structure as a function of threshold.

IV.D. Impact of Transport Cross Sections on Reaction Rate Calculations

The shape and magnitude of the neutron energy spectrum used in the reaction rate calculation depends among other things on the transport cross sections chosen. The latest available transport cross sections from ENDF/B-V and JENDL-3 were used by the United States and Japan, respectively. Figure 15 compares the two sets of neutron energy spectra for positions A and B. Note that for position A, the Japan spectrum, denoted as A (125g-J), is lower than the U.S. spectrum, denoted as A (63g-U), between 1 to 8 MeV. For location B, however, the two sets of computed spectra are

TABLE XIII

Status of Cross Sections of Reactions Leading to Production of Radioactive Isotopes in Tin

Material	Radioactive Isotope (Product)	Contributing Reactions	Status of Reaction Cross Sections in libraries of the Four Codes[a]			
			ACT4	REAC-3	DKR-ICF	RACC
Tin	^{117}In	^{117}Sn$(n,p)^{117}$In	p	p	p	p
		^{118}Sn$(n,np)^{117}$In	p	p	a	a
		^{118}Sn$(n,d)^{117}$In	a	p	p	p
		^{117}Sn$(n,p)^{117m}$In $\rightarrow$ ^{117}In	p	p	p	a
		^{118}Sn$(n,np)^{117m}$In $\rightarrow$ ^{117}In	p	p	a	a
		^{118}Sn$(n,d)^{117m}$In $\rightarrow$ ^{117}In	a	p	a	a
		^{120}Sn$(n,\alpha)^{117m}$Cd $\rightarrow$ ^{117m}In $\rightarrow$ ^{117}In	p	p	a	a
		^{120}Sn$(n,\alpha)^{117}$Cd $\rightarrow$ ^{117m}In $\rightarrow$ ^{117}In	p	p	p	p
	^{116m}In	^{116}Sn$(n,p)^{116m}$In	p	p	p	a
		^{117}Sn$(n,np)^{116m}$In	a	p	a	a
		^{117}Sn$(n,d)^{116m}$In	a	p	a	a
	^{115m}In	^{115}Sn$(n,p)^{115m}$In	p	p	a	a
		^{116}Sn$(n,np)^{115m}$In	p	p	a	a
		^{116}Sn$(n,d)^{115m}$In	a	p	a	a
		^{117}Sn$(n,t)^{115m}$In	a	p	a	a
		^{118}Sn$(n,\alpha)^{115m}$Cd $\rightarrow$ ^{115m}In	p	p	a	a
		^{118}Sn$(n,\alpha)^{115}$Cd $\rightarrow$ ^{115m}In	p	p	p	p
	^{111}In	^{112}Sn$(n,np)^{111}$In	p	p	a	a
		^{112}Sn$(n,d)^{111}$In	a	p	a	p
		^{112}Sn$(n,np)^{111m}$In $\rightarrow$ ^{111}In	p	p	a	a
		^{112}Sn$(n,d)^{111m}$In $\rightarrow$ ^{111}In	a	p	a	a
		^{112}Sn$(n,2n)^{111}$Sn $\rightarrow$ ^{111m}In $\rightarrow$ ^{111}In	p	p	p	p
	^{117m}Sn	^{118}Sn$(n,2n)^{117m}$Sn	p	p	p	a
		^{116}Sn$(n,\gamma)^{117m}$Sn	p	p	p	a
		^{117}Sn$(n,p)^{117m}$In $\rightarrow$ ^{117m}Sn	p	p	p	a
		^{118}Sn$(n,np)^{117m}$In $\rightarrow$ ^{117m}Sn	p	p	a	a
		^{118}Sn$(n,d)^{117m}$In $\rightarrow$ ^{117m}Sn	a	p	a	a
		^{117}Sn$(n,p)^{117}$In $\rightarrow$ ^{117m}Sn	p	p	p	p
		^{118}Sn$(n,np)^{117}$In $\rightarrow$ ^{117m}Sn	p	p	p	a
		^{118}Sn$(n,d)^{117}$In $\rightarrow$ ^{117m}Sn	a	p	a	p
		^{120}Sn$(n,\alpha)^{117m}$Cd $\rightarrow$ ^{117m}In $\rightarrow$ ^{117m}Sn	p	p	a	a
		^{120}Sn$(n,\alpha)^{117}$Cd $\rightarrow$ ^{117m}In $\rightarrow$ ^{117m}Sn	p	p	p	p
	^{113}Sn	^{114}Sn$(n,2n)^{113}$Sn	p	p	p	p
		^{112}Sn$(n,\gamma)^{113}$Sn	p	p	a	a
		^{114}Sn$(n,2n)^{113m}$Sn $\rightarrow$ ^{113}Sn	p	p	p	a
		^{112}Sn$(n,\gamma)^{113m}$Sn $\rightarrow$ ^{113}Sn	p	p	a	a

[a]The p stands for present, a for absent, and z for zero values for cross sections.

quite close between 1 to 11 MeV. Figure 16 shows ratios of computed (C) and experimental (E) reaction rates for six reactions: ^{27}Al$(n,\alpha)^{24}$Na, ^{51}V$(n,\alpha)^{48}$Sc, ^{54}Fe$(n,p)^{54}$Mn, ^{113}In$(n,n')^{113m}$In, ^{93}Nb$(n,2n)^{92m}$Nb, and ^{186}W$(n,\gamma)^{187}$W. Note that this figure shows values using the REAC-3 library only. The trends will be somewhat different for the other libraries. The C/E ratios are marked as U and J to denote the use of the U.S. and the Japan fluxes, respectively. Also shown in the figure are the ratios of the computed reaction rate with the U.S. flux to that with the Japan flux, for example, C(U)/C(J). One can observe that the ratio of the computed reaction rates varies from 0.94 to 1.46. It has been observed that, generally, this ratio is within 10% of unity. Thus, the computed flux shapes will affect the rates for different reactions differently. The largest departure from unity is seen for ^{113}In$(n,n')^{113m}$In. We add here that, although not shown, the ratio of the computed reaction rates for ^{115}In$(n,n')^{115m}$In is quite close to the one for ^{113}In$(n,n')^{113m}$In. Figure 17 is a plot

TABLE XIV

Cross-Sectional Integrals for Titanium, Vanadium, and Chromium

Material	Reaction	CSI (barn)				Reference CSI (b)
		ACT4	REAC-3	DKR-ICF	RACC	
Titanium	$^{47}Ti(n,p)^{47}Sc$	0.164	0.177	0.223	0.188	0.176[a]
	$^{48}Ti(n,p)^{48}Sc$	2.68×10^{-2}	2.75×10^{-2}	5.97×10^{-2}	4.87×10^{-2}	2.74×10^{-2}[a]
	$^{48}Ti(n,np)^{47}Sc$	1.09×10^{-3}	1.07×10^{-3}	1.02×10^{-3}	4.72×10^{-3}	
Vanadium	$^{51}V(n,p)^{51}Ti$	1.89×10^{-2}	1.87×10^{-2}	4.51×10^{-2}	3.93×10^{-2}	1.89×10^{-2}[b]
	$^{51}V(n,\alpha)^{48}Sc$	5.06×10^{-3}	4.98×10^{-3}	1.13×10^{-2}	4.75×10^{-3}	5.06×10^{-3}[b]
	$^{51}V(n,\gamma)^{52}V$	30.0	53.4	9.59	11.6	1.24×10^{-2}[b]
Chromium	$^{50}Cr(n,2n)^{49}Cr$	1.50×10^{-3}	2.25×10^{-3}	2.18×10^{-3}	4.31×10^{-3}	4.54×10^{-3}[c]
	$^{52}Cr(n,2n)^{51}Cr$	3.53×10^{-2}	3.90×10^{-2}	4.98×10^{-2}	4.08×10^{-2}	4.64×10^{-2}[c]
	$^{50}Cr(n,\gamma)^{51}Cr$	96.6	166.8	29.1	51.3	

[a]From ENDF/B-VI cross sections.
[b]From JENDL-3 cross sections.
[c]From JEF-2 cross sections.

of the cross section for $^{113}In(n,n')^{113m}In$ from the REAC-3 library. Also shown in Fig. 16 are the neutron energy spectra for location A from the United States (63-group REAC-3 structure) and Japan (125-group structure). It is evident that the Japan flux is generally lower than the U.S. flux in the energy range of interest from ~0.2 to ~10 MeV.

V. INTERCOMPARISON OF MEASURED AND COMPUTED ISOTOPIC ACTIVITY

The ratios of the computed and experimental isotopic activities, available from all four libraries, have been obtained for a number of neutron energy spectra. It is intended to display the range of C/Es for each isotopic product for different materials subjected to the irradiation. The materials to be covered include Al, Si, Ti, V, Cr, Mn, Fe, Co, Ni, Cu, Zn, Zr, Nb, Mo, Type 316 stainless steel, In, Sn, Ta, W, and Pb. First, overall C/E dispersion trends for each material are presented. The overall dispersion for an isotopic product is obtained by getting the lowest and the highest C/Es observed for its activity by the four libraries for all the spectral locations covered in the analysis. One standard deviation of experimental error is considered in getting the overall dispersion. Subsequently, the individual overall C/E dispersion trends for each of the four libraries are also discussed for each material. Table XVIII

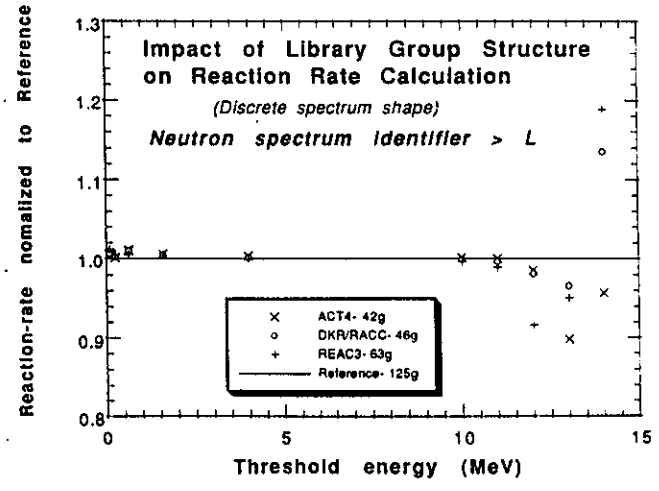

Fig. 14. Normalized reaction rate as function of threshold energy for the spectral shape L (normalized with respect to the spectral shape L in 125-energy group structure).

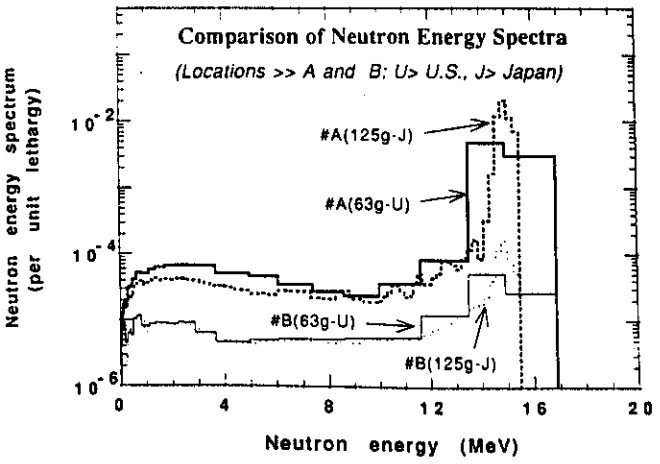

Fig. 15. Intercomparison of U.S. and Japanese neutron energy spectra for positions A and B.

TABLE XV

Cross-Sectional Integrals for Silicon, Manganese, Iron, Cobalt, and Nickel

Material	Reaction	CSI (barn)				Reference CSI (b)
		ACT4	REAC-3	DKR-ICF	RACC	
Silicon	$^{29}Si(n,p)^{29}Al$	6.92×10^{-2}	0.229	0.240	1.02×10^{-2}	8.71×10^{-2}[a]
	$^{30}Si(n,\alpha)^{27}Mg$	1.41×10^{-2}	3.15×10^{-2}	3.42×10^{-2}	4.60×10^{-3}	2.56×10^{-2}[a]
Manganese	$^{55}Mn(n,2n)^{54}Mn$	0.150	0.149	0.199	0.169	0.150[a,b] 0.168[c]
	$^{55}Mn(n,\alpha)^{52}V$	1.17×10^{-2}	1.44×10^{-2}	1.20×10^{-2}	1.32×10^{-2}	1.17×10^{-2}[a,b] 1.31×10^{-2}[c]
	$^{55}Mn(n,\gamma)^{56}Mn$	86.4	82.2	31.1	29.6	
Iron	$^{54}Fe(n,p)^{54}Mn$	0.700	0.683	0.736	0.411	0.661[b] 0.700[a] 0.760[c]
	$^{54}Fe(n,\alpha)^{51}Cr$	4.54×10^{-2}	4.50×10^{-2}	5.64×10^{-2}	5.91×10^{-2}	4.68×10^{-2}[b] 4.53×10^{-2}[a] 4.64×10^{-2}[c]
	$^{56}Fe(n,p)^{56}Mn$	6.26×10^{-2}	6.74×10^{-2}	6.94×10^{-2}	6.89×10^{-2}	
Cobalt	$^{59}Co(n,\gamma)^{60m}Co$	174.9	196.6	72.2	No data	
	$^{59}Co(n,\gamma)^{60}Co$	109.3	267.6	54.4	0.150	
	$^{59}Co(n,\gamma)^{58m}Co$	7.06×10^{-2}	9.17×10^{-2}	0.111	No data	
	$^{59}Co(n,2n)^{58}Co$	8.26×10^{-2}	0.144	4.74×10^{-2}	0.130	0.135[b] 0.137[a]
	$^{59}Co(n,\alpha)^{56}Mn$	1.19×10^{-2}	1.33×10^{-2}	1.19×10^{-2}	1.33×10^{-2}	
	$^{59}Co(n,p)^{59}Fe$	3.55×10^{-2}	3.75×10^{-2}	3.75×10^{-2}	6.36×10^{-2}	3.48×10^{-2}[b] 3.51×10^{-2}[a]
Nickel	$^{58}Ni(n,2n)^{57}Ni$	3.09×10^{-3}	3.09×10^{-3}	5.74×10^{-3}	4.07×10^{-3}	3.08×10^{-3}[b] 2.97×10^{-3}[a]
	$^{64}Ni(n,\gamma)^{65}Ni$	9.12	15.9	2.97	5.05	
	$^{58}Ni(n,p)^{58m}Co$	0.201	0.417	0.441	No data	
	$^{58}Ni(n,p)^{58}Co$	0.791	0.790	0.441	0.450	
	$^{58}Ni(n,np+d)^{57}Co$	0.127	0.162	0.157	3.75×10^{-2}	
	$^{60}Ni(n,p)^{60m}Co$	0.105	6.04×10^{-2}	6.50×10^{-2}	2.74×10^{-2}	
	$^{60}Ni(n,p)^{60}Co$	6.72×10^{-2}	0.103	6.50×10^{-2}	9.17×10^{-2}	
	$^{62}Ni(n,\alpha)^{59}Fe$	1.81×10^{-3}	1.03×10^{-2}	7.72×10^{-3}	1.27×10^{-6}	

[a]From ENDF/B-VI cross sections.
[b]From JENDL-3 cross sections.
[c]From JEF-2 cross sections.

provides a quick reference for locating tables and figures directly relevant to various isotopic activities.

Tables XIX through XXII list the lowest and highest C/Es observed for each of the four cross-section libraries for various isotopic activities. The tables also give the overall dispersion derived from the four libraries. Whenever a library does not have the cross-section data for all the important, contributing reactions for the production of an isotopic activity, an entry "missing" is noted. It is evident that the RACC library accounts for most of these notations. One can note from the tables that generally, there is considerable disagreement among the four libraries. Tables XXIII and XXIV show the isotopic products with the largest C/E dispersions. Also shown are the important reactions that lead to the production of those isotopic products. Practically, all irradiated materials have one or more isotopic products that suffer from serious disagreement among different cross-section libraries in predicting induced radioactivity.

The strategy for C/E plots for each material as a function of product half-life is as follows. Each such plot shows an upper envelope and a lower envelope. An envelope is plotted by joining the highest (or lowest) C/E values for each product as a function of half-life. The ratios of the computed and experimental isotopic activities, available from all the four libraries, have been obtained for a number of neutron energy spectra.

TABLE XVI

Cross-Sectional Integrals for Molybdenum, Zirconium, Niobium, Tantalum, Tungsten, and Copper

Material	Reaction	CSI (barn) ACT4	REAC-3	DKR-ICF	RACC	Reference CSI (b)
Molybdenum	$^{92}Mo(n,2n)^{91}Mo$	2.06×10^{-2}	1.79×10^{-2}	2.11×10^{-2}	4.55×10^{-2}	
	$^{92}Mo(n,2n)^{91m}Mo$	1.02×10^{-3}	1.79×10^{-2}	No data	No data	
	$^{95}Mo(n,p)^{95m}Nb$	3.01×10^{-3}	1.75×10^{-2}	7.01×10^{-3}	6.94×10^{-3}	
	$^{96}Mo(n,p)^{96}Nb$	5.88×10^{-3}	7.48×10^{-3}	2.83×10^{-2}	5.28×10^{-3}	
	$^{94}Mo(n,2n)^{93m}Mo$	8.37×10^{-4}	5.51×10^{-4}	9.57×10^{-4}	No data	
Zirconium	$^{90}Zr(n,2n)^{89m}Zr$	1.06×10^{-2}	9.08×10^{-2}	7.73×10^{-3}	7.23×10^{-3}	
	$^{90}Zr(n,2n)^{89}Zr$	6.90×10^{-2}	9.08×10^{-2}	0.110	9.61×10^{-2}	8.86×10^{-2}[a]
	$^{92}Zr(n,p)^{92}Y$	5.25×10^{-3}	6.56×10^{-3}	6.55×10^{-3}	4.15×10^{-3}	8.86×10^{-2}[a]
	$^{94}Zr(n,p)^{94}Y$	9.89×10^{-4}	2.76×10^{-3}	2.39×10^{-3}	1.34×10^{-3}	2.72×10^{-3}[a]
	$^{96}Zr(n,\gamma)^{97}Zr$	5.99	0.771	No data	No data	
	$^{96}Zr(n,2n)^{95}Zr$	0.739	0.647	0.576	0.733	0.643[a]
	$^{94}Zr(n,\gamma)^{95}Zr$	0.565	0.771	0.334	No data	
Niobium	$^{93}Nb(n,\alpha)^{90m}Y$	2.66×10^{-3}	No data	No data	4.01×10^{-3}	
	$^{93}Nb(n,2n)^{92m}Nb$	0.155	0.174	0.145	0.162	
Tantalum	$^{181}Ta(n,p)^{181}Hf$	7.18×10^{-4}	1.22×10^{-3}	1.30×10^{-3}	5.53×10^{-4}	1.41×10^{-3}[a]
	$^{181}Ta(n,2n)^{180m}Ta$	0.285	0.881	0.913	No data	
	$^{181}Ta(n,\gamma)^{182m}Ta$	1.06×10^{-5}	0.273	0.204	No data	
	$^{181}Ta(n,\gamma)^{182}Ta$	775.9	862.8	644.7	668.6	
Tungsten	$^{186}W(n,p)^{186}Ta$	3.74×10^{-4}	1.97×10^{-4}	2.52×10^{-4}	2.14×10^{-4}	1.36×10^{-4}[a]
	$^{186}W(n,\alpha)^{183}Hf$	6.92×10^{-5}	1.63×10^{-4}	2.02×10^{-4}	1.77×10^{-4}	
	$^{184}W(n,p)^{184}Ta$	4.33×10^{-4}	4.01×10^{-4}	5.19×10^{-4}	4.29×10^{-4}	3.62×10^{-4}[a]
	$^{186}W(n,\gamma)^{187}W$	559.8	919.8	1506.8	517.3	
	$^{182}W(n,p)^{182}Ta$	2.19×10^{-3}	5.61×10^{-4}	6.97×10^{-4}	5.53×10^{-4}	
Copper	$^{63}Cu(n,\alpha)^{60m}Co$	1.30×10^{-2}	3.13×10^{-2}	No data	No data	2.58×10^{-2}[a]
	$^{63}Cu(n,\alpha)^{60}Co$	1.00×10^{-2}	3.13×10^{-2}	1.03×10^{-2}	2.55×10^{-2}	
	$^{65}Cu(n,2n)^{64}Cu$	0.199	0.196	0.225	0.203	0.198[a]
	$^{63}Cu(n,\gamma)^{64}Cu$	30.2	52.7	10.9	12.7	

[a]From ENDF/B-VI cross sections.

In a few cases, the C/Es obtained with activation cross sections from ENDF/B-VI/JENDL-3/JEF-2 are also considered for getting the overall dispersion. It is intended to display the range of C/Es for each isotopic product for different materials subjected to the irradiation. For each isotopic product, typical C/E values lying between the upper and the lower envelopes are shown along with associated standard deviations.

V.A. Aluminum

Figure 18 is a plot of C/Es for aluminum. It encompasses the data for two spectral locations, i.e., A and B, only. Results with the ENDF/B-VI cross sections are also included. For ^{27}Mg, C/E ranges from 1.08 to 3.04. The corresponding range for the ENDF/B-VI activation cross sections is slightly narrower, going from 1.2 to 3.0. The C/E is larger for B. For ^{24}Na, C/E ranges from 0.96 to 1.24. The corresponding range for the ENDF/B-VI activation cross sections is from 1.03 to 1.18. The C/E is larger for B. The cross sections are plotted as a function of energy for the $^{27}Al(n,p)^{27}Mg$ and the $^{27}Al(n,\alpha)^{24}Na$ reactions in Figs. 19 and 20. The REAC-3 cross sections appear to be lying closest to the ENDF/B-VI data. Significant differences in the cross-sectional integrals for the $^{27}Al(n,p)^{27}Mg$ and $^{27}Al(n,\alpha)^{24}Na$ reactions (see Table XVII) are also indicative of the divergence in the C/E values from the different libraries.

V.B. Silicon

Figure 21 is a plot of C/Es for silicon. The data were available only for spectral location A. Results with the JENDL-3 cross sections are also included. Figure 22 is a plot of the C/E data with JENDL-3 alone.

TABLE XVII

Cross-Sectional Integrals for Aluminum, Zinc, Tin, and Lead

Material	Reaction	CSI (barn)				Reference CSI (b)
		ACT4	REAC-3	DKR-ICF	RACC	
Aluminum	$^{27}Al(n,p)^{27}Mg$	8.14×10^{-2}	8.82×10^{-2}	9.26×10^{-2}	8.79×10^{-2}	8.78×10^{-2}[a]
	$^{27}Al(n,\alpha)^{24}Na$	7.02×10^{-2}	6.68×10^{-2}	7.01×10^{-2}	6.65×10^{-2}	6.64×10^{-2}[a]
Zinc	$^{70}Zn(n,2n)^{69m}Zn$	0.170	0.308	0.201	No data	
	$^{67}Zn(n,p)^{67}Cu$	2.34×10^{-2}	9.86×10^{-2}	3.57×10^{-2}	4.80×10^{-3}	
	$^{66}Zn(n,2n)^{65}Zn$	0.121	9.88×10^{-2}	0.118	7.60×10^{-3}	
Tin	$^{118}Sn(n,2n)^{117m}Sn$	0.225	0.475	1.45×10^{-2}	No data	
	$^{116}Sn(n,\gamma)^{117m}Sn$	2.59×10^{-2}	10.7	0.236	No data	
	$^{114}Sn(n,2n)^{113}Sn$	2.59×10^{-2}	0.286	0.198	0.344	0.260[b]
	$^{112}Sn(n,\gamma)^{113}Sn$	18.8	10.7	No data	No data	
Lead	$^{204}Pb(n,2n)^{203}Pb$	0.419	0.615	0.712	1.03	0.768[b]

[a]From ENDF/B-VI cross sections.
[b]From JENDL-3 cross sections.

The C/Es are closer to unity, and the dispersion is smaller compared with the corresponding values in Fig. 21. The cross sections are plotted as a function of energy for the $^{29}Si(n,p)^{29}Al$, and $^{30}Si(n,\alpha)^{27}Mg$ reactions in Figs. 23 and 24. All the libraries deviate from the JENDL-3 cross sections. It is evident that silicon cross sections need to be updated in all the libraries. Note that the ACT4 and RACC results lie close to each other and are considerably below unity for both ^{29}Al and ^{27}Mg. Similarly, the C/E results from REAC-3 and DKR-ICF are close to each other and are significantly larger than unity for both isotopic activities.

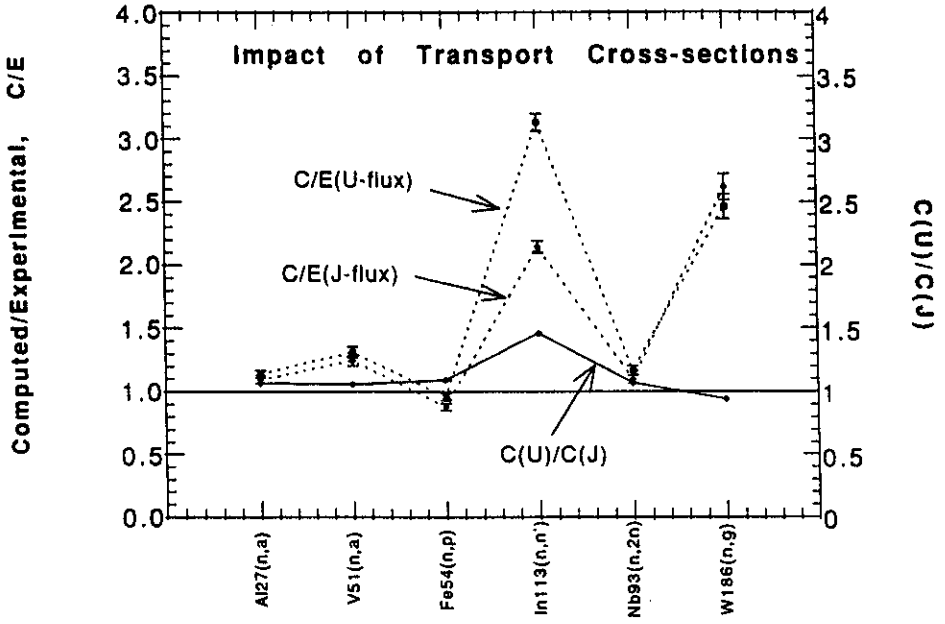

Fig. 16. Comparison of computed to experimental rates, using U.S. and Japanese fluxes for six reactions: $^{27}Al(n,\alpha)^{24}Na$, $^{51}V(n,\alpha)^{48}Sc$, $^{54}Fe(n,p)^{54}Mn$, $^{113}In(n,n')^{113m}In$, $^{93}Nb(n,2n)^{92m}Nb$, and $^{186}W(n,\gamma)^{187}W$ (cross sections from REAC-3 library only).

TABLE XVIII

Quick Index for Locating Tables and Figures of Direct Relevance to Various Isotopic Activities

Material	Radioactive Isotope	Reference Numbers	
		Table	Figure
Aluminum	^{27}Mg	XVII, XIX	18, 19
	^{24}Na	XVII, XIX	18, 20
Silicon	^{29}Al	XV, XIX	21, 22, 23
	^{27}Mg	XV, XIX	21, 22, 24
Titanium	^{48}Sc	XIV, XIX	25, 26, 28 to 31
	^{47}Sc	XIV, XIX	25, 27, 28 to 31
	^{47}Ca	XIX	25, 28 to 31
	^{46}Sc	XIX	25, 28 to 31
Vanadium	^{52}V	XIV, XIX	32, 33
	^{51}Ti	XIV, XIX	32, 34
	^{48}Sc	XIV, XIX	32, 35
Chromium	^{49}Cr	XIV, XIX	36, 37
	^{51}Cr	XIV, XIX	36, 38
Manganese	^{52}V	XV, XIX	39, 40
	^{56}Mn	XV, XIX	39, 41
	^{54}Mn	XV, XIX	39, 42
Iron	^{56}Mn	XV, XIX	43, 44
	^{51}Cr	XV, XIX	43, 45
	^{54}Mn	XV, XIX	43, 46
Cobalt	^{56}Mn	XV, XIX	47
	^{59}Fe	XV, XIX	47
	^{58}Co	XV, XIX	47, 48
	^{60}Co	XV, XIX	47, 49
Nickel	^{62m}Co	XX	50
	^{57}Ni	XV, XX	50, 51
	^{59}Fe	XV, XX	50
	^{58}Co	XV, XX	50, 52
	^{57}Co	XV, XX	50
	^{60}Co	XV, XX	50, 53
Copper	^{62m}Co	XX	54
	^{65}Ni	XX	54
	^{64}Cu	XVI, XX	54, 55, 56
	^{60}Co	XVI, XX	54, 57
Zinc	^{63}Zn	XX	58
	^{65}Ni	XX	58
	^{64}Cu	XX	58
	^{69m}Zn	XVII, XX	58, 59
	^{67}Cu	XVII, XX	58, 60
	^{65}Zn	XVII, XX	58, 61
Zirconium	^{94}Y	XVI, XX	62, 63
	^{91m}Y	XX	62
	^{97}Nb	XX	62
	^{87m}Sr	XX	62
	^{90m}Y	XX	62
	^{92}Y	XVI, XX	62
	^{91}Sr	XX	62
	^{97}Zr	XVI, XX	62, 64
Zirconium	^{89}Zr	XVI, XX	62, 65, 66
	^{95}Zr	XVI, XX	62, 67
Niobium	^{90m}Y	XVI, XX	68, 69
	^{92m}Nb	XVI, XX	68, 70, 71
Molybdenum	^{101}Tc	XXI	72
	^{101}Mo	XXI	72
	^{91}Mo	XVI, XXI	72, 73, 74
	^{98m}Nb	XXI	72
	^{97}Nb	XXI	72
	^{93m}Mo	XVI, XXI	72, 75, 76
	^{96}Nb	XVI, XXI	72, 77
	^{99}Mo	XXI	72, 78
	^{89}Zr	XXI	72
	^{95m}Nb	XVI, XXI	72, 79
	^{92m}Nb	XXI	72
	^{95}Nb	XXI	72
	^{91}Nb	XXI	72
	^{95}Zr	XXI	72
SS316	All	---	80 to 84
Indium	^{112}In	XXI	85
	^{112m}In	XXI	85
	^{116m}In	XXI	85
	^{113m}In	XXI	85
	^{112}Ag	XXI	85
	^{115m}In	XXI	85
	^{114}In	XXI	85, 86
	^{115}Cd	XXI	85
	^{114m}In	XXI	85, 87
Tin	^{117}In	XXI	88, 89
	^{116m}In	XXI	88, 90
	^{115m}In	XXI	88
	^{111}In	XXI	88
	^{117m}Sn	XVII, XXI	88, 91, 92
	^{113}Sn	XVII, XXI	88, 93
Tantalum	^{180m}Hf	XXI	94
	^{180m}Ta	XVI, XXI	94
	^{181}Hf	XVI, XXI	94, 95
	^{182}Ta	XVI, XXI	94
Tungsten	^{186}Ta	XVI, XXII	96, 97
	^{182m}Ta	XXII	96
	^{183}Hf	XVI, XXII	96, 98
	^{184}Ta	XVI, XXII	96, 99
	^{187}W	XXII	96
	^{183}Ta	XVI, XXII	96, 98
	^{182}Ta	XVI, XXII	96
Lead	^{204m}Pb	XXII	101
	^{203}Pb	XVII, XXII	101, 102

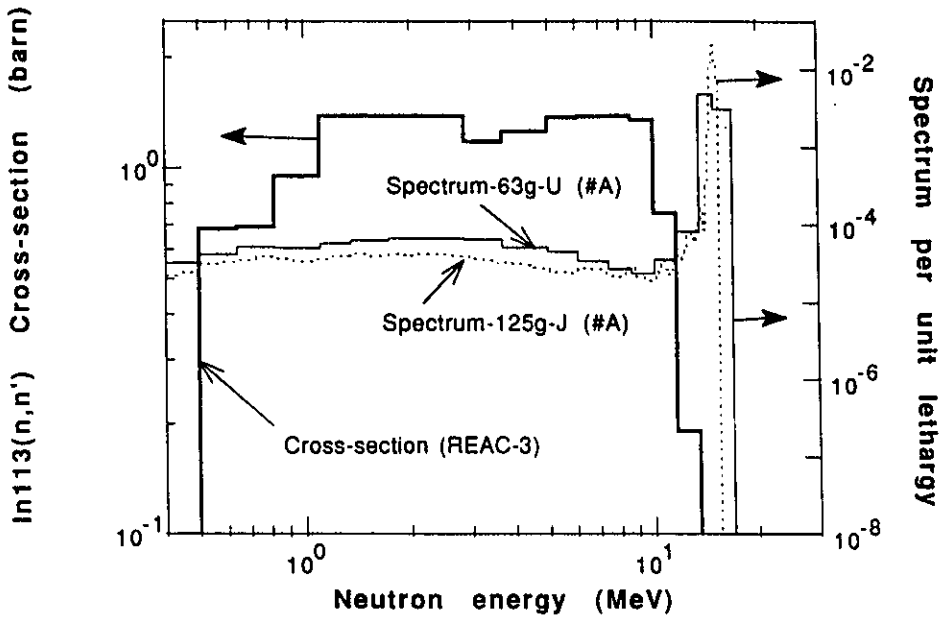

Fig. 17. Cross section for $^{113}In(n,n')^{113m}In$ reaction from REAC-3 library and U.S./Japanese neutron energy spectra for location A.

V.C. Titanium

Figure 25 is a plot of C/Es for titanium. The data for the two spectral locations, i.e., A and B, are considered. The results for the ^{48}Sc product also include C/Es with the ENDF/B-VI activation cross sections. The cross sections are plotted as a function of energy for the $^{48}Ti(n,p)^{48}Sc$ and $^{47}Ti(n,p)^{47}Sc$ reactions in Figs. 26 and 27. Of all the libraries, REAC-3 comes closest to the ENDF/B-VI cross sections. The DKR-ICF and RACC libraries are close to each other but deviate much from the ENDF/B-VI cross sections for these reactions.

Figures 28 through 31 show C/Es for the ACT4, REAC-3, DKR-ICF, and RACC libraries, respectively. Overall, ACT4 yields the best predictions. The REAC-3 and RACC predictions for ^{47}Sc are definitely too high. In fact, $^{48}Ti(n,d)^{47}Sc$ and $^{48}Ti(n,np)^{47}Sc$ together contribute as much as ~70% to ^{47}Sc isotopic activity by REAC-3, in contrast to an ~29% contribution for ACT4; the corresponding contributions for RACC and

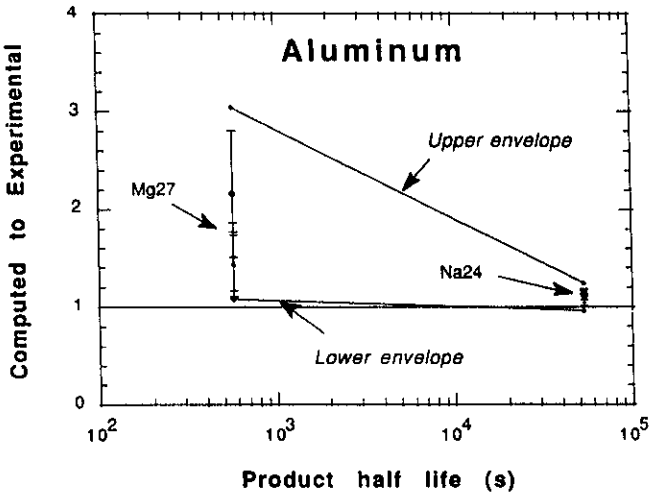

Fig. 18. Aluminum: Overall C/E dispersion for isotopic activities, using activation cross-section data contained in ACT4, REAC-3, DKR-ICF, RACC, and ENDF/B-VI libraries.

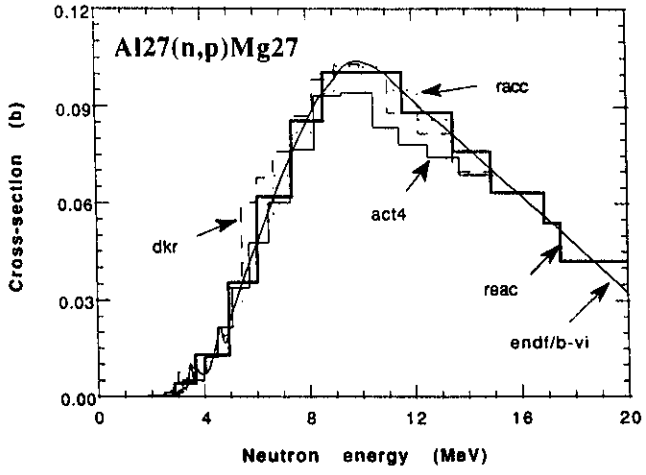

Fig. 19. Cross sections for $^{27}Al(n,p)^{27}Mg$ reaction from different libraries.

TABLE XIX

Observed C/E Ranges for Isotopic Activities in Irradiated Samples of Aluminum, Silicon, Titanium, Vanadium, Manganese, Iron, and Cobalt

Irradiated Material	Radioactive Isotope (Product)	Observed C/E Ranges for Various Activation Cross-Section Libraries				
		ACT4	REAC-3	DKR-ICF	RACC	All Four Libraries
Aluminum	^{27}Mg	1.1 to 2.8	1.1 to 2.9	1.1 to 3.0	1.2 to 3.1	1.1 to 3.1
	^{24}Na	1.07 to 1.20	0.97 to 1.17	1.03 to 1.22	1.07 to 1.23	0.97 to 1.23
Silicon	^{29}Al	0.50 to 0.64	1.64 to 2.10	1.75 to 2.22	0.62 to 0.79	0.50 to 2.22
	^{27}Mg	0.50 to 0.76	1.08 to 1.68	1.12 to 1.74	0.56 to 0.87	0.50 to 1.74
Titanium	^{48}Sc	1.05 to 1.20	1.00 to 1.20	1.14 to 1.56	1.29 to 1.63	1.00 to 1.63
	^{47}Sc	0.71 to 0.94	2.19 to 2.53	0.52 to 0.91	1.46 to 1.70	0.52 to 2.53
	^{47}Ca	0.66 to 0.97	0.80 to 1.19	0.65 to 0.98	0.55 to 0.83	0.55 to 1.19
	^{46}Sc	1.05 to 1.22	1.07 to 1.23	0.84 to 0.97	1.08 to 1.26	0.84 to 1.26
Vanadium	^{52}V	0.84 to 2.24	0.73 to 1.54	0.72 to 1.66	0.73 to 2.01	0.72 to 2.24
	^{51}Ti	0.83 to 1.13	0.97 to 1.25	1.05 to 1.76	1.33 to 1.93	0.83 to 1.93
	^{48}Sc	0.86 to 1.13	1.14 to 1.36	2.40 to 3.19	0.98 to 1.31	0.86 to 3.19
Chromium	^{49}Cr	0.84 to 1.27	2.89 to 4.21	1.00 to 1.58	2.22 to 3.30	0.84 to 4.21
	^{51}Cr	0.63 to 1.01	0.71 to 1.29	0.77 to 1.13	0.74 to 1.12	0.63 to 1.29
Manganese	^{52}V	7.3 to 8.9	9.0 to 11.0	9.0 to 11.1	8.6 to 10.7	7.3 to 11.1
	^{56}Mn	1.41 to 1.72	1.93 to 2.21	1.77 to 2.12	1.55 to 1.85	1.41 to 2.21
	^{54}Mn	0.95 to 1.10	0.97 to 1.13	1.05 to 1.23	1.00 to 1.17	0.95 to 1.23
Iron	^{56}Mn	0.88 to 1.10	0.77 to 1.07	0.90 to 1.13	1.01 to 1.22	0.77 to 1.22
	^{51}Cr	0.87 to 0.99	0.75 to 0.86	0.94 to 1.07	1.51 to 1.70	0.75 to 1.70
	^{54}Mn	1.04 to 1.23	0.85 to 0.99	0.97 to 1.11	1.19 to 1.34	0.85 to 1.34
Cobalt	^{56}Mn	0.90 to 1.42	0.91 to 1.20	0.93 to 1.26	0.93 to 1.27	0.90 to 1.42
	^{59}Fe	1.04 to 2.09	1.75 to 2.08	0.83 to 1.05	0.97 to 1.16	0.83 to 2.08
	^{58}Co	1.05 to 1.26	1.32 to 1.57	1.54 to 1.84	1.75 to 2.08	1.05 to 2.08
	^{60}Co	3.10 to 5.03	4.10 to 6.81	2.60 to 4.36	0.085 to 0.14	0.085 to 6.81

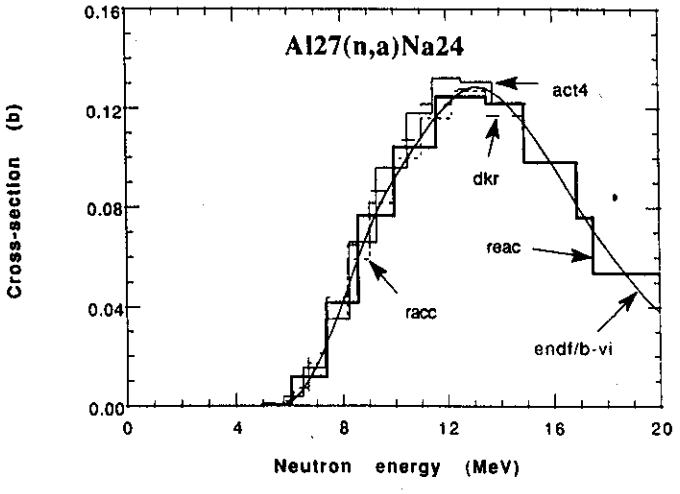

Fig. 20. Cross sections for ^{27}Al$(n,\alpha)^{24}$Na reaction from different libraries.

DKR-ICF are ~53 and ~3%, respectively. As for ^{48}Sc, the cross section for the ^{48}Ti$(n,p)^{48}$Sc reaction is largely overpredicted for both DKR-ICF and RACC.

V.D. Vanadium

Figure 32 is a plot of C/Es for vanadium. The data for three spectral locations, i.e., A, B, and C, are considered. The C/E results with the JENDL-3 activation cross sections were not included for obtaining the overall C/E range for ^{52}V. The cross sections are plotted as a function of energy for the ^{51}V$(n,\gamma)^{52}$V, ^{51}V(n,p)-^{51}Ti, and ^{51}V$(n,\alpha)^{48}$Sc reactions in Figs. 33, 34, and 35. Of all the libraries, REAC-3 comes closest to the JENDL-3 cross sections. Other libraries deviate much from the JENDL-3 cross sections for these reactions. The JENDL-3 cross section for ^{51}V$(n,\gamma)^{52}$V has odd behavior in that it drops to zero below ~0.1 MeV. This leads to a strong underestimation of ^{52}V production,

TABLE XX

Observed C/E Ranges for Isotopic Activities in Irradiated Samples of Nickel, Copper, Zinc, Zirconium, and Niobium

Irradiated Material	Radioactive Isotope (Product)	Observed C/E Ranges for Various Activation Cross-Section Libraries				
		ACT4	REAC-3	DKR-ICF	RACC	All Four Libraries
Nickel	^{62m}Co	1.30 to 1.64	1.34 to 1.68	1.34 to 1.70	Missing	1.30 to 1.70
	^{57}Ni	0.86 to 1.10	0.87 to 1.19	1.15 to 1.66	1.05 to 1.43	0.86 to 1.66
	^{59}Fe	0.88 to 1.52	1.96 to 3.21	0.62 to 1.05	5.5×10^{-4} to 9.0×10^{-4}	5.5×10^{-4} to 3.21
	^{58}Co	1.09 to 2.00	1.19 to 2.26	0.55 to 1.28	0.94 to 1.55	0.55 to 2.26
	^{57}Co	0.88 to 1.22	1.20 to 1.53	0.91 to 1.32	0.25 to 0.33	0.25 to 1.53
	^{60}Co	0.81 to 1.39	0.78 to 1.31	0.53 to 0.88	1.89 to 3.10	0.53 to 3.10
Copper	^{62m}Co	0.6 to 16.5	0.6 to 19.1	Missing	Missing	0.6 to 19.1
	^{65}Ni	1.08 to 1.31	0.98 to 1.20	1.02 to 1.24	Missing	0.98 to 1.31
	^{64}Cu	0.76 to 0.85	0.74 to 0.83	0.75 to 0.84	0.75 to 0.84	0.74 to 0.85
	^{60}Co	0.31 to 1.24	0.71 to 1.33	0.11 to 0.41	0.30 to 1.13	0.11 to 1.33
Zinc	^{63}Zn	1.5 to 1.8	2.9 to 3.3	1.5 to 1.8	1.5 to 1.8	1.5 to 3.3
	^{65}Ni	0.2 to 1.1	0.24 to 1.24	0.2 to 1.2	0.5 to 1.2	0.2 to 1.24
	^{64}Cu	0.73 to 0.93	0.32 to 0.55	0.51 to 0.88	1.34 to 2.32	0.32 to 2.32
	^{69m}Zn	0.88 to 1.43	1.67 to 2.71	0.68 to 1.22	1.37×10^{-4} to 7.87×10^{-2}	1.37×10^{-4} to 2.71
	^{67}Cu	0.49 to 0.96	2.84 to 5.57	0.44 to 0.70	0.59 to 3.17	0.44 to 5.57
	^{65}Zn	1.29 to 1.36	0.76 to 0.80	1.20 to 1.26	0.35 to 0.38	0.35 to 1.36
Zirconium	^{94}Y	0.56 to 0.63	1.29 to 1.44	0.97 to 1.11	0.58 to 0.67	0.56 to 1.44
	^{91m}Y	1.10 to 1.32	2.15 to 2.64	0.78 to 0.96	0.73 to 1.20	0.73 to 2.64
	^{97}Nb	1.21 to 2.30	0.068 to 0.13	Missing	Missing	0.068 to 2.30
	^{87m}Sr	0.87 to 0.93	1.18 to 1.28	Missing	Missing	0.87 to 1.28
	^{90m}Y	1.10 to 1.18	4.10 to 4.32	0.60 to 0.65	0.60 to 0.65	0.60 to 4.32
	^{92}Y	1.02 to 1.11	1.31 to 1.44	0.91 to 1.02	0.73 to 0.82	0.73 to 1.44
	^{91}Sr	1.01 to 1.17	1.24 to 1.42	1.35 to 1.58	1.17 to 1.38	1.01 to 1.58
	^{97}Zr	0.89 to 1.40	0.048 to 0.072	Missing	Missing	0.048 to 1.40
	^{89}Zr	0.91 to 0.98	2.33 to 2.47	1.13 to 1.22	1.14 to 1.19	0.91 to 2.47
	^{95}Zr	1.01 to 1.65	0.85 to 1.39	0.73 to 1.20	1.00 to 1.64	0.73 to 1.65
Niobium	^{90m}Y	0.6 to 1.0	1.1 to 2.3	Missing	Missing	0.6 to 2.3
	^{92m}Nb	0.80 to 1.13	0.87 to 1.06	0.88 to 1.15	0.79 to 1.01	0.79 to 1.15

the corresponding C/E range for JENDL-3 being just 0.10 to 0.17.

Regarding librarywise comparisons, we see that the DKR-ICF cross section for $^{51}V(n,\alpha)^{48}Sc$ is clearly too high above ~10 MeV. This generates too high a C/E range (see Table XIX), that is, 2.40 to 3.19. For the ^{51}Ti prediction, both DKR-ICF and RACC yield overly high C/Es, largely due to too large cross sections for $^{51}V(n,p)^{51}Ti$ above ~4 MeV.

V.E. Chromium

Figure 36 is a plot of C/Es for chromium. The data for two spectral locations, i.e., A and K, are considered. The cross sections are plotted as a function of energy for the $^{50}Cr(n,2n)^{49}Cr$ and $^{52}Cr(n,2n)^{51}Cr$ reactions in Figs. 37 and 38. The JEF-2 cross-section data are also plotted; the ENDF/B-VI and JENDL-3 cross-section data were not available for these two reactions. The status of the cross sections for the two reactions appears questionable. More data points need to be included in JEF. In addition, all four libraries need to have a much finer group structure above ~10 MeV to describe the cross-section behavior with confidence.

As for comparison of librarywise C/Es, even though ^{51}Cr has contributions from both the $^{52}Cr(n,2n)^{51}Cr$ and $^{50}Cr(n,\gamma)^{51}Cr$ reactions, the former sweeps the latter. For example, for spectral location A, the $(n,2n)$ contribution is as much as ~1000 times of the (n,γ) one. The C/E dispersions for ^{51}Cr are almost comparable for the four libraries. However, for ^{49}Cr, both REAC-3 and RACC strongly overpredict the C/Es. A

TABLE XXI

Observed C/E Ranges for Isotopic Activities in Irradiated Samples of Molybdenum, Indium, Tin, and Tantalum

Irradiated Material	Radioactive Isotope (Product)	Observed C/E Ranges for Various Activation Cross-Section Libraries				
		ACT4	REAC-3	DKR-ICF	RACC	All Four Libraries
Molybdenum	^{101}Tc	1.7 to 2.4	1.4 to 2.2	1.4 to 2.0	1.3 to 2.1	1.3 to 2.4
	^{101}Mo	2.0 to 3.3	1.7 to 2.9	1.6 to 2.7	1.5 to 2.8	1.5 to 3.3
	^{91}Mo	0.7 to 1.9	1.7 to 4.2	0.9 to 1.8	1.7 to 4.2	0.7 to 4.2
	^{98m}Nb	1.2 to 1.6	1.2 to 1.6	Missing	Missing	1.2 to 1.6
	^{97}Nb	0.68 to 0.72	3.9 to 4.2	1.0 to 1.2	0.7 to 0.8	0.68 to 4.2
	^{93m}Mo	1.4 to 2.2	5.9 to 9.3	2.0 to 3.1	Missing	1.4 to 9.3
	^{96}Nb	1.5 to 2.0	2.7 to 3.4	4.3 to 5.6	1.3 to 1.8	1.3 to 5.6
	^{99}Mo	0.99 to 1.12	0.81 to 0.93	0.89 to 1.02	1.11 to 1.27	0.81 to 1.27
	^{89}Zr	0.94 to 1.00	2.05 to 2.22	1.53 to 1.67	1.75 to 1.91	0.94 to 2.22
	^{95m}Nb	0.83 to 0.92	6.6 to 7.4	1.7 to 2.0	1.6 to 2.0	0.83 to 7.4
	^{92m}Nb	0.99 to 1.12	1.06 to 1.17	1.0 to 1.2	1.1 to 1.4	0.99 to 1.4
	^{95}Nb	1.02 to 1.10	2.37 to 2.55	2.4 to 2.7	0.7 to 0.9	0.7 to 2.7
	^{91}Nb	1.4 to 1.7	3.04 to 3.45	1.3 to 1.6	3.1 to 3.7	1.3 to 3.7
	^{95}Zr	0.4 to 0.6	1.03 to 1.25	1.0 to 1.3	0.6 to 0.8	0.4 to 1.3
Indium	^{112}In	0.23 to 0.50	0.28 to 0.61	0.020 to 0.043	Missing	0.02 to 0.61
	^{112m}In	0.50 to 0.80	0.6 to 0.8	Missing	Missing	0.50 to 0.80
	^{116m}In	0.4 to 0.6	0.3 to 0.4	1.27 to 1.45	Missing	0.30 to 1.45
	^{113m}In	1.1 to 1.4	2.0 to 3.2	Missing	Missing	1.1 to 3.2
	^{112}Ag	1.2 to 2.1	2.2 to 3.8	1.5 to 2.7	Missing	1.2 to 3.8
	^{115m}In	0.009 to 0.2	2.07 to 3.57	Missing	Missing	0.009 to 3.57
	^{114}In	0.003 to 0.006	0.65 to 0.92	0.56 to 0.84	Missing	0.003 to 0.92
	^{115}Cd	1.6 to 2.3	6.8 to 9.7	2.1 to 3.1	Missing	1.6 to 9.7
	^{114m}In	0.005 to 0.008	1.08 to 1.46	0.93 to 1.24	Missing	0.005 to 1.46
Tin	^{117}In	0.33 to 0.52	4.61 to 7.32	0.29 to 0.46	0.18 to 0.29	0.18 to 7.32
	^{116m}In	0.1 to 0.3	1.1 to 2.7	0.1 to 0.5	Missing	0.1 to 2.7
	^{115m}In	0.40 to 0.76	1.35 to 2.63	0.48 to 0.93	2.58 to 4.89	0.40 to 4.89
	^{111}In	1.5 to 1.9	1.2 to 1.6	1.2 to 1.5	0.95 to 1.76	0.95 to 1.9
	^{117m}Sn	0.9 to 1.1	1.7 to 1.9	0.0061 to 0.066	Missing	0.0061 to 1.9
	^{113}Sn	0.6 to 0.8	1.6 to 1.9	0.7 to 0.9	1.03 to 1.16	0.6 to 1.9
Tantalum	^{180m}Hf	Missing	11.4 to 100.2	7.21×10^{-4} to 3.16×10^{-3}	Missing	7.21×10^{-4} to 100.2
	^{180m}Ta	0.53 to 4.28	1.2 to 10.6	1.3 to 10.7	Missing	0.53 to 10.7
	^{181}Hf	0.98 to 1.28	1.43 to 1.88	1.52 to 2.05	1.00 to 1.36	0.98 to 2.05
	^{182}Ta	1.28 to 1.70	1.22 to 1.64	1.00 to 1.34	1.28 to 1.72	1.00 to 1.72

high threshold for the ^{50}Cr$(n,2n)^{49}$Cr reaction coupled with very coarse energy group structure is responsible for these C/E spreads. In fact, it is sheer chance that DKR-ICF and ACT4 yield more reasonable C/Es!

V.F. Manganese

Figure 39 is a plot of C/Es for manganese. The data for two spectral locations, i.e., A and B, are considered. The results for the ENDF/B-VI (same as JENDL-3) and JEF-2 activation cross sections are also included. The cross sections are plotted as a function of energy for the ^{55}Mn$(n,\alpha)^{52}$V, ^{55}Mn$(n,\gamma)^{56}$Mn, and ^{55}Mn$(n,2n)^{54}$Mn reactions in Figs. 40, 41, and 42. The JEF-2 cross-section data do not agree very well with the ENDF/B-VI data for ^{55}Mn$(n,\alpha)^{52}$V and ^{55}Mn$(n,2n)^{54}$Mn. The status of the cross sections for these two reactions is questionable. All the libraries show deviations from the ENDF/B-VI data. Also, the C/Es for ^{52}V look too high in light of the cross-section plot of Fig. 40. The experimental data could be doubted to be in error for this product. All the libraries appear to overpredict both ^{56}Mn and ^{54}Mn. The relatively high threshold (~11 MeV) for the ^{55}Mn$(n,2n)^{54}$Mn reaction and the coarse energy group structure appear to be mainly responsible for the overprediction of C/Es for ^{54}Mn. As for ^{56}Mn, two contributing factors are traceable. First, the cross sections differ significantly from each other. In fact, CSI's for ACT4, REAC-3, DKR-ICF, and RACC are 86.4, 82.2, 31.1, and 29.6 b, respectively. Second, the computed neutron energy spectrum is inadequate to deal with a series of resonances in the (n,γ) cross section from 100 eV to 100 KeV. Also, the spectrum for the lower energy neutrons may be overestimated.

TABLE XXII

Observed C/E Ranges for Isotopic Activities in Irradiated Samples of Tungsten and Lead

Irradiated Material	Radioactive Isotope (Product)	Observed C/E Ranges for Various Activation Cross-Section Libraries				
		ACT4	REAC-3	DKR-ICF	RACC	All Four Libraries
Tungsten	^{186}Ta	1.6 to 2.2	2.0 to 2.6	1.3 to 1.7	1.1 to 1.6	1.1 to 2.6
	^{182m}Ta	Missing	9.5 to 23.3	Missing	Missing	9.5 to 23.3
	^{183}Hf	0.5 to 0.7	4.6 to 5.7	2.4 to 3.0	2.3 to 2.8	0.5 to 5.7
	^{184}Ta	0.8 to 1.2	1.6 to 2.2	1.1 to 1.7	1.0 to 1.5	0.8 to 2.2
	^{187}W	0.95 to 1.66	1.57 to 2.73	3.80 to 6.80	1.74 to 3.30	0.95 to 6.80
	^{183}Ta	0.8 to 1.1	2.1 to 2.7	1.2 to 1.6	1.2 to 1.6	0.8 to 2.7
	^{182}Ta	1.04 to 1.34	2.28 to 2.81	0.76 to 0.97	0.70 to 0.90	0.70 to 2.81
Lead	^{204m}Pb	Missing	24.9 to 48.5	Missing	Missing	24.9 to 48.5
	^{203}Pb	0.57 to 0.73	1.01 to 1.29	1.06 to 1.34	1.35 to 1.72	0.57 to 1.72

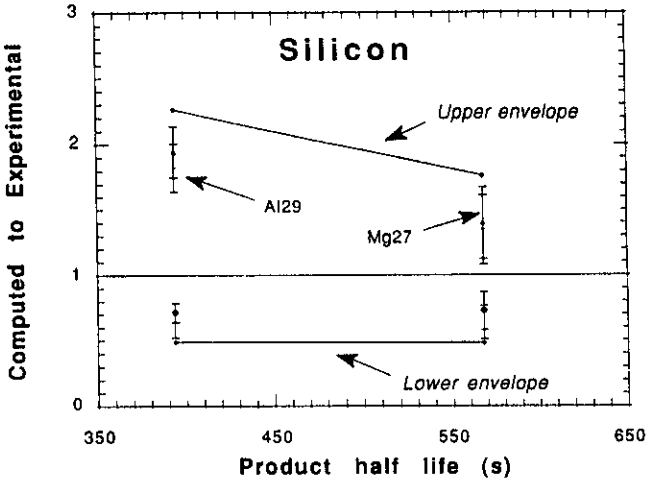

Fig. 21. Silicon: Overall C/E dispersion for isotopic activities, using activation cross-section data contained in ACT4, REAC-3, DKR-ICF, RACC, and JENDL-3 libraries.

V.G. Iron

Figure 43 is a plot of C/Es for iron. The data for three spectral locations, i.e., A, F, and L, are considered. The results with the ENDF/B-VI, JENDL-3, and JEF-2 cross sections are also included for ^{54}Mn. The cross sections are plotted as a function of energy for the ^{56}Fe$(n,p)^{56}$Mn, ^{54}Fe$(n,\alpha)^{51}$Cr, and ^{54}Fe$(n,p)^{54}$Mn reactions in Figs. 44, 45, and 46. The JEF-2 and JENDL-3 cross-section data do not have excellent agreement with the ENDF/B-VI data for ^{54}Fe$(n,\alpha)^{51}$Cr and ^{54}Fe(n,p)-^{54}Mn. The ACT4 cross sections are closest to ENDF/B-VI. Even though all the libraries show deviations from the ENDF/B-VI data, the RACC and REAC-3 libraries have the largest deviations of the four.

The cross section for the ^{54}Fe$(n,\alpha)^{51}$Cr reaction is significantly off in the REAC-3, DKR-ICF, and RACC libraries, being underpredicted at a higher energy in REAC-3 and overpredicted in RACC above ~10 MeV. The shape of this cross section differs sharply from those in ENDF/B-VI, JENDL-3, and JEF-2. The cross-section shape for ^{54}Fe$(n,p)^{54}$Mn in RACC differs sharply from those in the ENDF/B-VI, JENDL-3, and JEF-2 libraries. Even larger C/E dispersion for the ^{54}Mn production is bound to occur with RACC. Table XV compares CSIs for ^{54}Fe$(n,p)^{54}$Mn. The RACC library has the lowest value of 0.41 b as against 0.76 b by the JEF-2 library. This large difference in the CSIs stresses a need for large improvement for this cross section, particularly in the RACC library. The

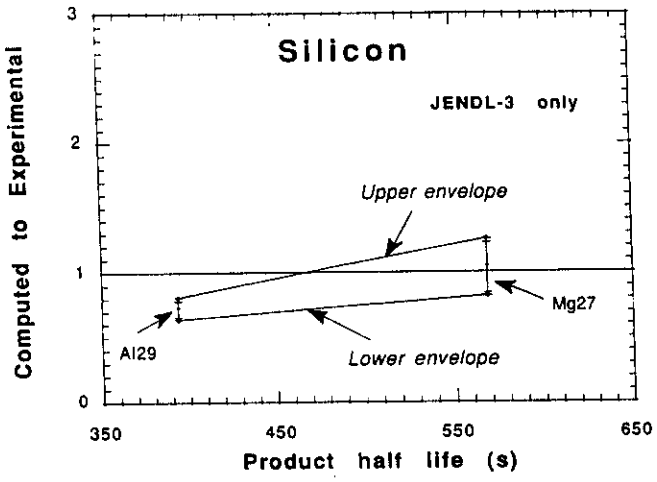

Fig. 22. Silicon: C/E dispersion for isotopic activities, using activation cross-section data contained in JENDL-3 library alone.

TABLE XXIII

Radioactive Products with Large C/E Dispersions, Resulting from D-T Neutron Irradiation of Al, Si, Ti, V, Cr, Mn, Fe, Co, Ni, Co, Cu, Zn, Zr, and Nb

Irradiated Material	Isotopic Products with Large C/E Dispersion (Overall C/E Dispersion)	Important Reactions Leading to Production of the Radioactive Isotopic Products
Aluminum	^{27}Mg (1.1 to 3.1)	^{27}Al$(n,p)^{27}$Mg
Silicon	^{29}Al (0.50 to 2.22)	^{30}Si$(n,p)^{29}$Al
Titanium	^{48}Sc (1.00 to 1.63) ^{47}Sc (0.52 to 2.53)	^{48}Ti$(n,p)^{48}$Sc ^{47}Ti$(n,p)^{47}$Sc
Vanadium	^{52}V (0.72 to 2.24) ^{51}Ti (0.83 to 1.93) ^{48}Sc (0.86 to 3.19)	^{51}V$(n,\gamma)^{52}$V ^{51}V$(n,p)^{51}$Ti ^{51}V$(n,\alpha)^{48}$Sc
Chromium	^{49}Cr (0.84 to 4.21)	^{50}Cr$(n,2n)^{49}$Cr
Manganese	^{52}V (7.3 to 11.1)	^{55}Mn$(n,\alpha)^{52}$V
Iron	^{54}Mn (0.85 to 1.34)	^{55}Mn$(n,2n)^{54}$Mn
Cobalt	^{59}Fe (0.83 to 2.08) ^{58}Co (1.05 to 2.08) ^{60}Co (0.085 to 6.81)	^{59}Co$(n,p)^{59}$Fe ^{59}Co$(n,2n)^{58}$Co, ^{59}Co$(n,2n)^{58m}$Co $\rightarrow$ ^{58}Co ^{59}Co$(n,\gamma)^{60}$Co, ^{59}Co$(n,\gamma)^{60m}$Co $\rightarrow$ ^{60}Co
Nickel	^{62m}Co (1.30 to 1.70) ^{57}Ni (0.86 to 1.66) ^{58}Co (0.55 to 2.26) ^{57}Co (0.25 to 1.53) ^{60}Co (0.53 to 3.10)	^{62}Ni$(n,p)^{62m}$Co ^{58}Ni$(n,2n)^{57}$Ni ^{58}Ni$(n,p)^{58}$Co, ^{58}Ni$(n,p)^{58m}$Co $\rightarrow$ ^{58}Co ^{58}Ni$(n,np/d)^{57}$Co ^{60}Ni$(n,p)^{60}$Co, ^{60}Ni$(n,p)^{60m}$Co $\rightarrow$ ^{60}Co
Copper	^{60}Co (0.11 to 1.33) ^{62m}Co (0.6 to 19.1)	^{63}Cu$(n,\alpha)^{60}$Co, ^{63}Cu$(n,\alpha)^{60m}$Co $\rightarrow$ ^{60}Co ^{65}Cu$(n,\alpha)^{62m}$Co
Zinc	^{64}Cu (0.32 to 2.32) ^{69m}Zn (1.37×10^{-4} to 2.71) ^{67}Cu (0.44 to 5.57) ^{65}Zn (0.35 to 1.36)	^{64}Zn$(n,p)^{64}$Cu ^{70}Zn$(n,2n)^{69m}$Zn, ^{68}Zn$(n,\gamma)^{69m}$Zn ^{67}Zn$(n,p)^{67}$Cu ^{64}Zn$(n,\gamma)^{65}$Zn, ^{66}Zn$(n,2n)^{65}$Zn
Zirconium	^{94}Y (0.56 to 1.44) ^{91m}Y (0.73 to 2.64) ^{97}Zr (0.048 to 1.40) ^{90m}Y (0.60 to 4.32) ^{97}Nb (0.068 to 2.30) ^{89}Zr (0.91 to 2.47) ^{95}Zr (0.73 to 1.65)	^{94}Zn$(n,p)^{94}$Y, ^{96}Zr$(n,t)^{94}$Y ^{91}Zr$(n,p)^{91m}$Y, ^{92}Zr$(n,np/d)^{91m}$Y ^{96}Zr$(n,\gamma)^{97}$Zr ^{90}Zr$(n,p)^{90m}$Y, ^{91}Zr$(n,np/d)^{90m}$Y ^{96}Zr$(n,\gamma)^{97}$Zr $\rightarrow$ ^{97}Nb ^{90}Zr$(n,2n)^{89}$Zr, ^{90}Zr$(n,2n)^{89m}$Zr $\rightarrow$ ^{89}Zr ^{96}Zr$(n,2n)^{95}$Zr, ^{94}Zr$(n,\gamma)^{95}$Zr
Niobium	^{90m}Y (0.6 to 2.3)	^{93}Nb$(n,\alpha)^{90m}$Y

REAC-3 cross section for the ^{56}Fe$(n,p)^{56}$Mn reaction seems to be clearly underestimated in the 13- to 15-MeV range. This is responsible for the downward trend in the C/E values for the ^{56}Mn production by this library.

V.H. Cobalt

Figure 47 is a plot of C/Es for cobalt. The data for two spectral locations, i.e., A and C, are considered. The results with ENDF/B-VI, JENDL-3, and JEF-2 (same as ENDF/B-VI) cross sections are also included for ^{59}Fe. The cross sections are plotted as a function of energy for the ^{59}Co$(n,2n)^{58}$Co and ^{59}Co$(n,\gamma)^{60}$Co reactions in Figs. 48 and 49. The JENDL-3 and ENDF/B-VI libraries differ significantly from each other for ^{59}Co$(n,2n)^{58}$Co; REAC-3 comes closest to JENDL-3 and ENDF/B-VI; ACT4 and DKR-ICF cross sections differ much from all the others. As for ^{59}Co$(n,\gamma)^{60}$Co, all four libraries have different cross sections. However, ACT4 and RACC have peculiar representations for this reaction; the cross section in RACC is constant at $<10^{-2}$ b below ~1 MeV! The ACT4 cross section above ~3 MeV drops rapidly and is lower by a factor or 4 or more below the smallest cross section at ~14 MeV.

TABLE XXIV

Radioactive Products with Large C/E Dispersions, Resulting from D-T Neutron Irradiation of Mo, In, Sn, Ta, W, and Pb

Irradiated Material	Isotopic Products with Large C/E Dispersion (Overall C/E Dispersion)		Important Reactions Leading to Production of the Radioactive Isotopic Products
Molybdenum	^{101}Tc	(1.3 to 2.4)	^{100}Mo$(n,\gamma)^{101}$Mo $\rightarrow$ ^{101}Tc
	^{101}Mo	(1.5 to 3.3)	^{100}Mo$(n,\gamma)^{101}$Mo
	^{91}Mo	(0.7 to 4.2)	^{92}Mo$(n,2n)^{91}$Mo
	^{97}Nb	(0.68 to 4.2)	^{97}Mo$(n,p)^{97}$Nb, ^{98}Mo$(n,np/d)^{97}$Nb
	^{95}Nb	(0.7 to 2.7)	^{95}Mo$(n,p)^{95}$Nb, ^{96}Mo$(n,np/d)^{95}$Nb, ^{95m}Nb $\rightarrow$ ^{95}Nb
	^{91}Nb	(1.3 to 3.7)	^{92}Mo$(n,2n)^{91}$Mo $\rightarrow$ ^{91}Nb
	^{95}Zr	(0.4 to 1.3)	^{98}Mo$(n,\alpha)^{95}$Zr
Indium	^{112}In	(0.02 to 0.61)	^{113}In$(n,2n)^{112}$In
	^{112m}In	(0.50 to 0.80)	^{113}In$(n,2n)^{112m}$In
	^{116m}In	(0.30 to 1.45)	^{115}In$(n,\gamma)^{116m}$In
	^{115m}In	(0.009 to 3.57)	^{115}In$(n,n')^{115m}$In
	^{114}In	(0.003 to 0.92)	^{115}In$(n,2n)^{114m}$In $\rightarrow$ ^{114}In
	^{115}Cd	(1.6 to 9.7)	^{115}In$(n,p)^{115}$Cd
	^{114m}In	(0.005 to 1.46)	^{115}In$(n,2n)^{114m}$In
Tin	^{117}In	(0.18 to 7.32)	^{117}Sn$(n,p)^{117}$In, ^{118}Sn$(n,np/d)^{117}$In, ^{117m}In $\rightarrow$ ^{117}In
	^{116m}In	(0.1 to 2.7)	^{116}Sn$(n,p)^{116m}$In, ^{117}Sn$(n,np/d)^{116m}$In
	^{115m}In	(0.40 to 4.89)	^{115}Sn$(n,p)^{115m}$In, ^{116}Sn$(n,np/d)^{115m}$In, ^{118}Sn$(n,\alpha)^{115m}$Cd $\rightarrow$ ^{115m}In, ^{118}Sn$(n,\alpha)^{115}$Cd $\rightarrow$ ^{115m}In
	^{117m}Sn	(0.0061 to 1.9)	^{118}Sn$(n,2n)^{117m}$Sn, ^{116}Sn$(n,\gamma)^{117m}$Sn
	^{113}Sn	(0.6 to 1.9)	^{114}Sn$(n,2n)^{113}$Sn, ^{112}Sn$(n,\gamma)^{113}$Sn, ^{114}Sn$(n,2n)^{113m}$Sn $\rightarrow$ ^{113}Sn, ^{112}Sn$(n,\gamma)^{113m}$Sn $\rightarrow$ ^{113}Sn
Tantalum	^{180m}Hf	(7.21×10^{-4} to 100.2)	^{180}Ta$(n,p)^{180m}$Hf, ^{181}Ta$(n,np/d)^{180m}$Hf
	^{180m}Ta	(0.53 to 10.7)	^{181}Ta$(n,2n)^{180m}$Ta
Tungsten	^{186}Ta	(1.1 to 2.6)	^{186}W$(n,p)^{186}$Ta
	^{183}Hf	(0.5 to 5.7)	^{186}W$(n,\alpha)^{183}$Hf
	^{184}Ta	(0.8 to 2.2)	^{184}W$(n,p)^{184}$Ta
	^{187}W	(0.95 to 6.80)	^{186}W$(n,\gamma)^{187}$W
	^{183}Ta	(0.8 to 2.7)	^{183}W$(n,p)^{183}$Ta, ^{184}W$(n,np/d)^{183}$Ta
	^{182}Ta	(0.70 to 2.81)	^{182}W$(n,p)^{182}$Ta, ^{183}W$(n,np/d)^{182}$Ta, ^{182m}Ta $\rightarrow$ ^{182}Ta
Lead	^{204m}Pb	(24.9 to 48.5)	^{204}Pb$(n,n')^{204m}$Pb, ^{206}Pb$(n,3n)^{204m}$Pb
	^{203}Pb	(0.57 to 1.72)	^{204}Pb$(n,2n)^{203}$Pb

Note that the RACC library does not have cross-section data for the ^{59}Co$(n,2n)^{58m}$Co and ^{59}Co$(n,\gamma)^{60m}$Co reactions, which contribute to the production of ^{58}Co and ^{60}Co, respectively. The REAC-3 library has clear trends for a large overprediction for ^{59}Fe, ^{58}Co, and ^{60}Co. As for ^{58}Co, the sum of CSIs for both the ^{59}Co$(n,2n)^{58m}$Co and ^{59}Co$(n,2n)^{58}$Co reactions in REAC-3 is almost twice as much as for the other libraries. For ^{60}Co, the sum of CSIs for both the ^{59}Co$(n,\gamma)^{60m}$Co and ^{59}Co$(n,\gamma)^{60}$Co reactions is 1.6 times that for ACT4; it is 3.7 times that for DKR-ICF; it is more than 3000 times that for RACC.

V.I. Nickel

Figure 50 is a plot of C/Es for nickel. The data for three spectral locations, i.e., A, B, and K, are considered. The results with the ENDF/B-VI, JENDL-3, and JEF-2 (same as ENDF/B-VI) cross sections are also included for ^{57}Ni. The cross sections are plotted as a function of energy for the ^{58}Ni$(n,2n)^{57}$Ni, ^{58}Ni$(n,p)^{58}$Co, and ^{60}Ni$(n,p)^{60}$Co reactions in Figs. 51, 52, and 53. The JENDL-3 and ENDF/B-VI libraries do not differ significantly from each other for ^{58}Ni$(n,2n)^{57}$Ni below 16 MeV. All the libraries have a rather coarse

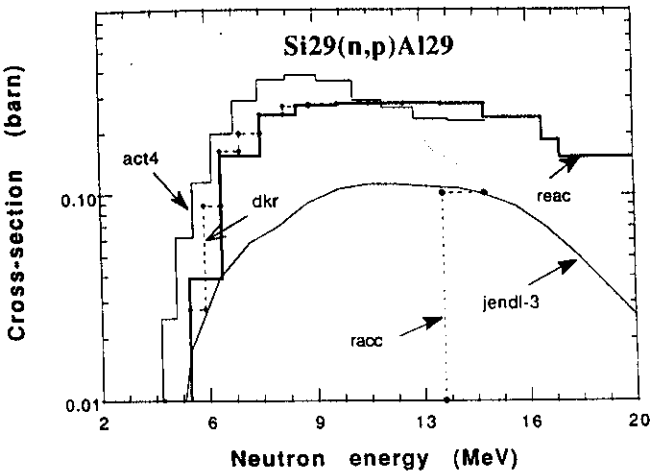

Fig. 23. Cross sections for $^{29}Si(n,p)^{29}Al$ reaction from different libraries.

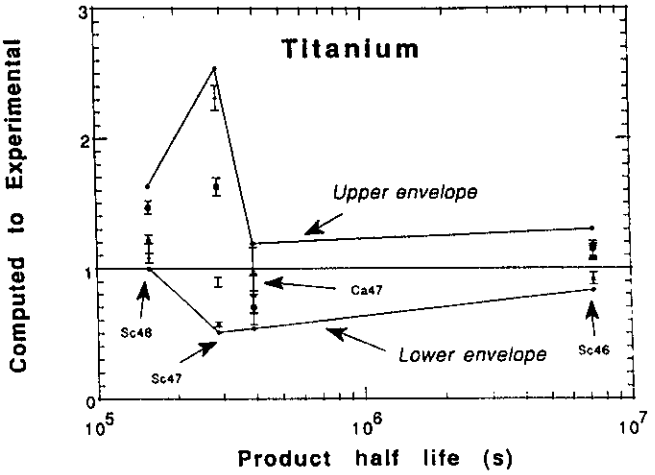

Fig. 25. Titanium: Overall C/E dispersion for isotopic activities, using activation cross-section data contained in ACT4, REAC-3, DKR-ICF, RACC libraries.

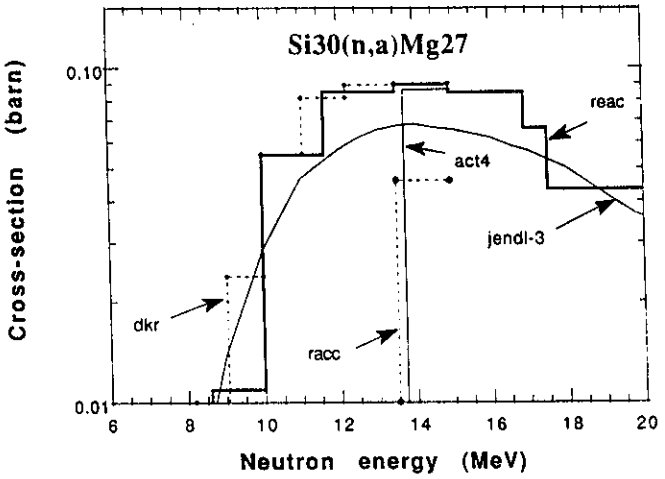

Fig. 24. Cross sections for $^{30}Si(n,\alpha)^{27}Mg$ reaction from different libraries.

group structure in the energy range of interest for this reaction to make any unambiguous judgment as to the quality of the cross section. But, the CSIs from DKR-ICF and RACC are considerably above those from ENDF/B-VI, JENDL-3, and the other libraries. This can explain the tendency of both these libraries to systematically overpredict C/Es for $^{58}Ni(n,2n)^{57}Ni$. As for $^{58}Ni(n,p)^{58}Co$, all four libraries have different cross sections and deviate from ENDF/B-VI. The cross sections for $^{60}Ni(n,p)^{60}Co$ differ much from each other; the cross section in DKR-ICF appears to be much lower than that in other libraries between 10 to 15 MeV. These cross-section data need large improvement.

The RACC library does not have cross sections for the $^{62}Ni(n,p)^{62m}Co$ and $^{58}Ni(n,p)^{58m}Co$ reactions. The cross section for the $^{62}Ni(n,\alpha)^{59}Fe$ reaction is too low. The production rate of ^{59}Fe is three orders lower compared with those by the other libraries. The CSI for the $^{62}Ni(n,\alpha)^{59}Fe$ reaction for RACC is three to four orders lower than those for the other three libraries (see Table XV). The REAC-3 library systematically overpredicts the ^{59}Fe production. There are two contributors behind this trend: (a) the largest cross section for the $^{62}Ni(n,\alpha)^{59}Fe$ reaction (see CSIs in Table XV) and (b) the large value for the $^{60}Ni(n,2p)^{59}Fe$ reaction from REAC-3, as much as ~30% of the total ^{59}Fe production. In fact, this reaction channel is absent in the other three libraries. As for ^{58}Co, the sum of CSIs for the $^{58}Ni(n,p)^{58m}Co$ and $^{58}Ni(n,p)^{58}Co$ reactions

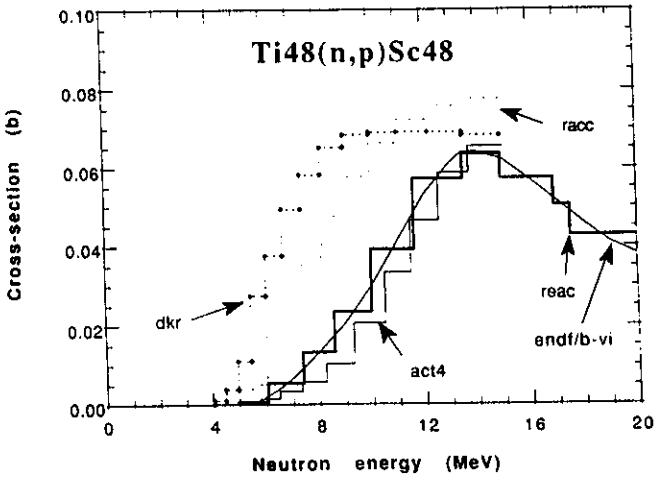

Fig. 26. Cross sections for $^{48}Ti(n,p)^{48}Sc$ reaction from different libraries.

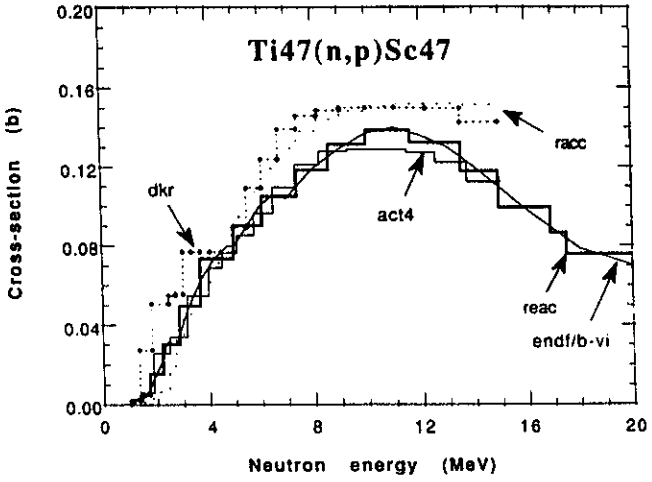

Fig. 27. Cross sections for $^{47}Ti(n,p)^{47}Sc$ reaction from different libraries.

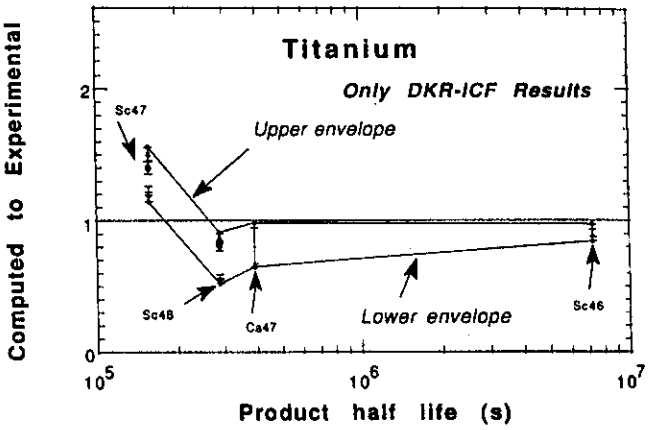

Fig. 30. Titanium: C/E dispersion for isotopic activities, using activation cross-section data contained in DKR-ICF library alone.

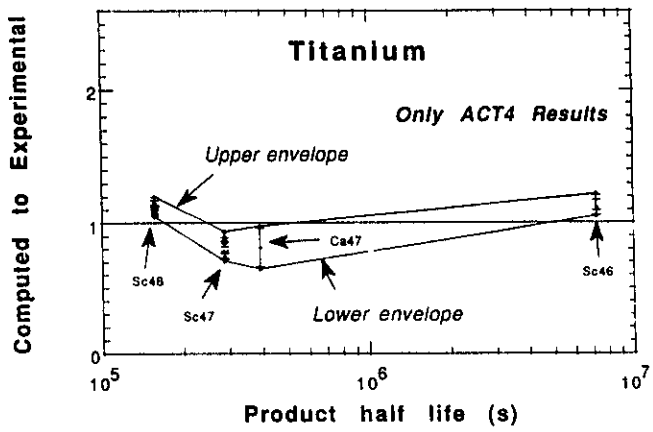

Fig. 28. Titanium: C/E dispersion for isotopic activities, using activation cross-section data contained in ACT4 library alone.

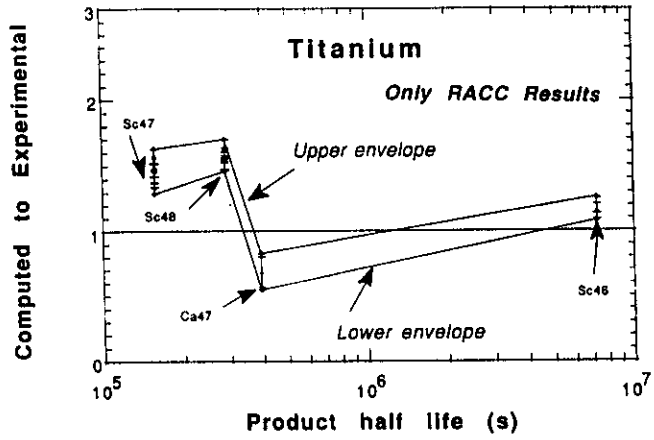

Fig. 31. Titanium: C/E dispersion for isotopic activities, using activation cross-section data contained in RACC library alone.

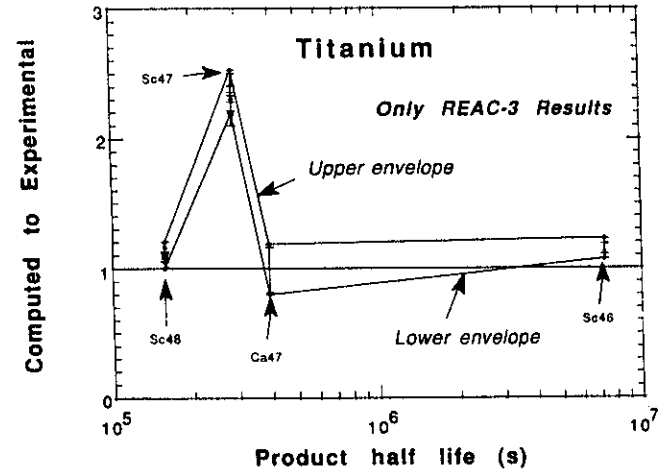

Fig. 29. Titanium: C/E dispersion for isotopic activities, using activation cross-section data contained in REAC-3 library alone.

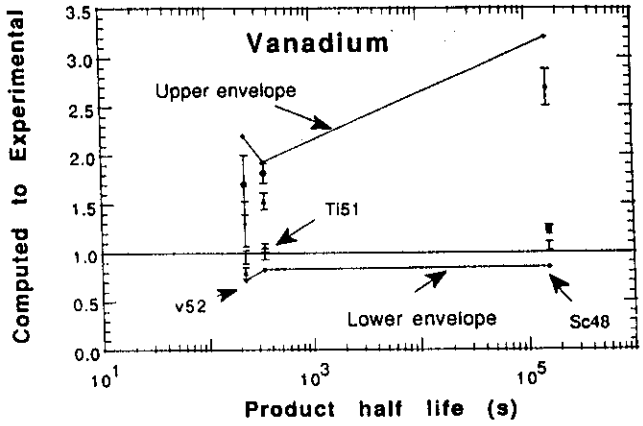

Fig. 32. Vanadium: Overall C/E dispersion for isotopic activities, using activation cross-section data contained in ACT4, REAC-3, DKR-ICF, RACC, and JENDL-3 libraries.

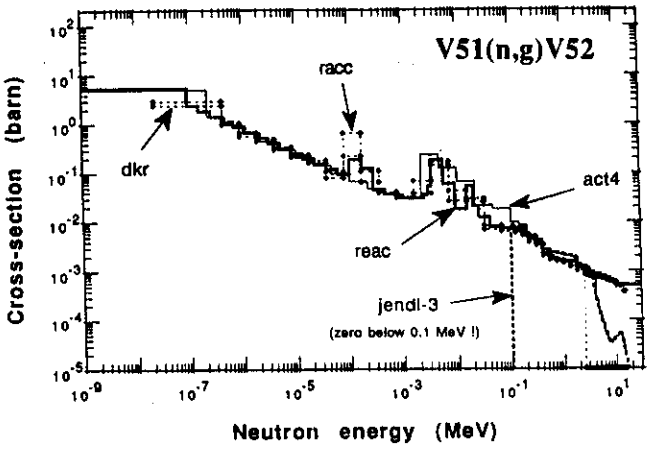

Fig. 33. Cross sections for $^{51}V(n,\gamma)^{52}V$ reaction from different libraries.

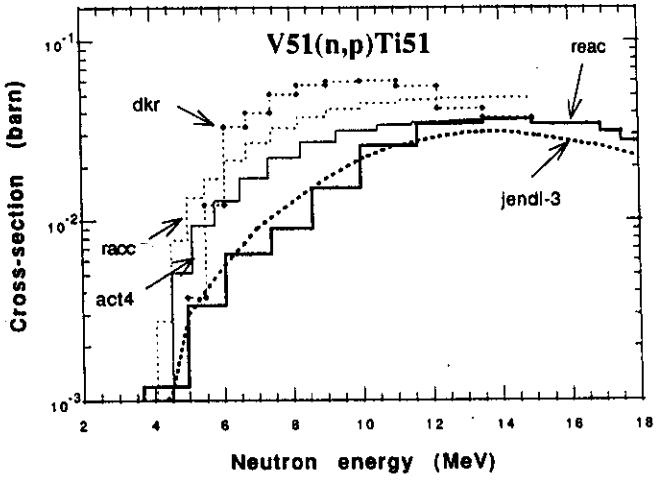

Fig. 34. Cross sections for $^{51}V(n,p)^{51}Ti$ reaction from different libraries.

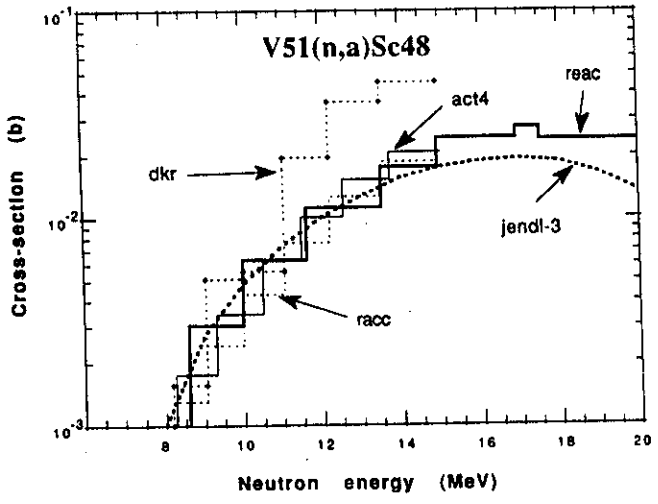

Fig. 35. Cross sections for $^{51}V(n,\alpha)^{48}Sc$ reaction from different libraries.

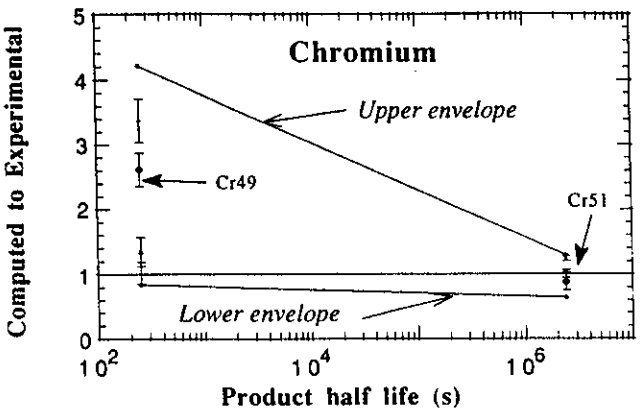

Fig. 36. Chromium: Overall C/E dispersion for isotopic activities, using activation cross-section data contained in ACT4, REAC-3, DKR-ICF, and RACC libraries.

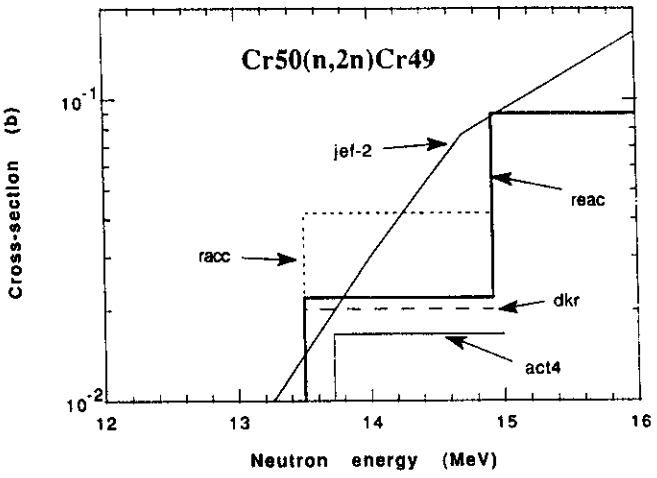

Fig. 37. Cross sections for $^{50}Cr(n,2n)^{49}Cr$ reaction from different libraries.

is the lowest for RACC, a factor of ~2 or more compared with that from the other three libraries. The contribution of $^{58}Ni(n,np+d)^{57}Co$ to ^{57}Co production is a factor of ~4 lower compared with the other libraries. The contribution of $^{60}Ni(n,p)^{60m}Co$ to ^{60}Co production is approximately a factor of 4 higher compared with the other libraries.

V.J. Copper

Figure 54 is a plot of C/Es for copper. The data for two spectral locations, i.e., A and K, are considered. The cross sections are plotted as a function of energy for the $^{65}Cu(n,2n)^{64}Cu$, $^{63}Cu(n,\gamma)^{64}Cu$, and $^{63}Cu(n,\alpha)^{60}Co$ reactions in Figs. 55, 56, and 57. The ENDF/B-VI cross sections are also plotted. All four libraries have different cross sections and deviate from ENDF/B-VI. In fact, both ACT4 and DKR-ICF have

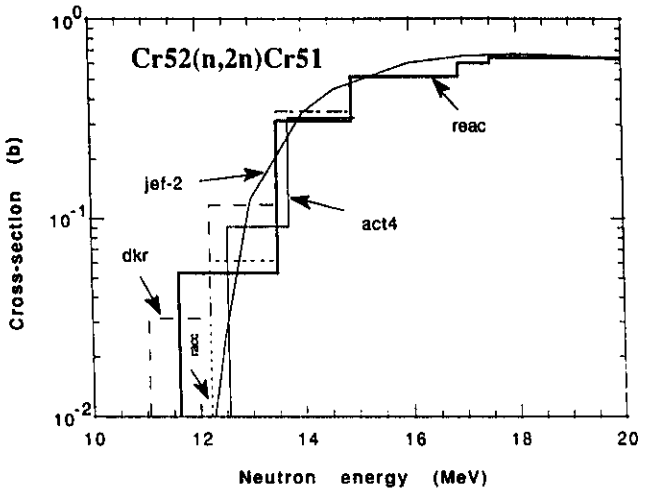

Fig. 38. Cross sections for $^{52}Cr(n,2n)^{51}Cr$ reaction from different libraries.

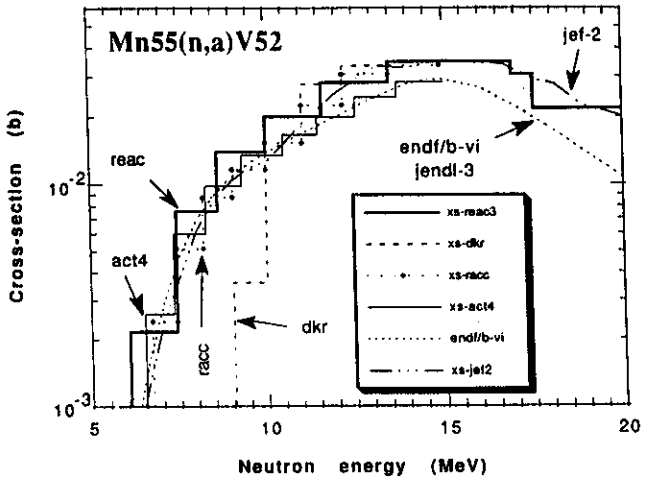

Fig. 40. Cross sections for $^{55}Mn(n,\alpha)^{52}V$ reaction from different libraries.

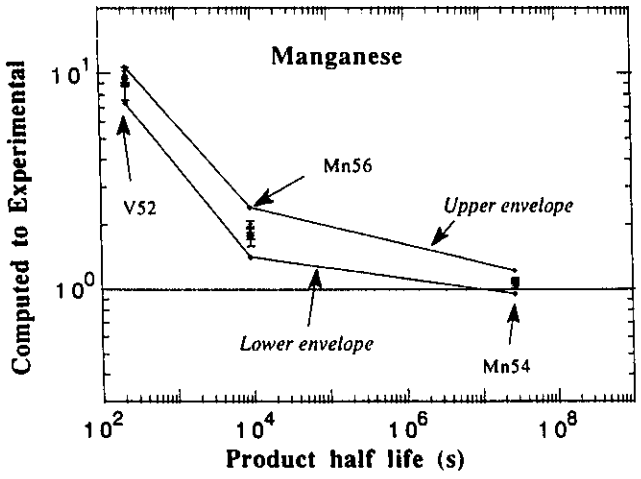

Fig. 39. Manganese: Overall C/E dispersion for isotopic activities, using activation cross-section data contained in ACT4, REAC-3, DKR-ICF, and RACC libraries.

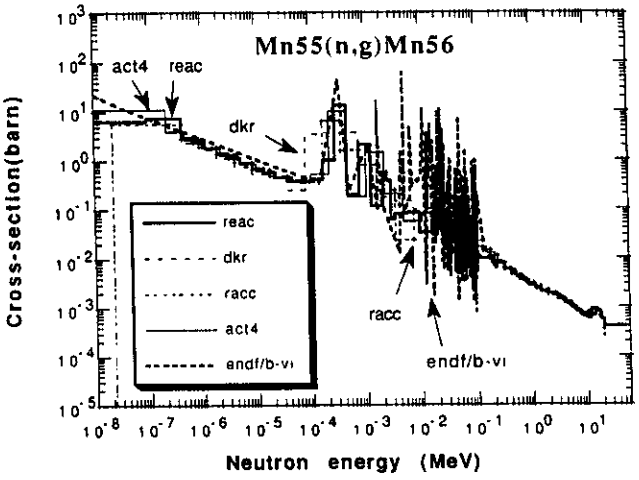

Fig. 41. Cross sections for $^{55}Mn(n,\gamma)^{56}Mn$ reaction from different libraries.

cross sections for the $^{63}Cu(n,\alpha)^{60}Co$ reaction that are much lower than those in ENDF/B-VI, REAC-3, and RACC. As for ^{60}Co, the sum of the CSIs for the $^{63}Cu(n,\alpha)^{60m}Co$ and $^{63}Cu(n,\alpha)^{60}Co$ reactions is quite low for DKR-ICF (see Table XVI). This explains the trend of systematically low C/E values for this library for ^{60}Co. Regarding C/E dispersion of ^{62m}Co, it appears that the experimental data for the spectral location A, which lead to C/Es lying toward the upper envelope, might be in error. The cross-section data for the ACT4 and REAC-3 libraries for $^{65}Cu(n,\alpha)^{62m}Co$ yield computed reaction rates that lie within 15% of each other.

Both the DKR-ICF and RACC libraries do not have cross-section data for $^{65}Cu(n,\alpha)^{62m}Co$ as well as

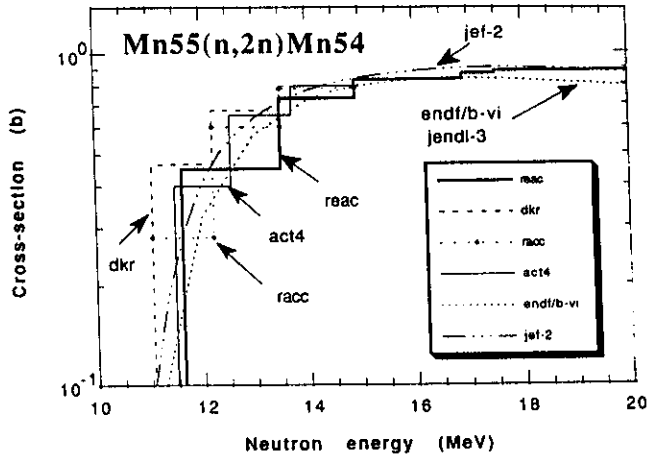

Fig. 42. Cross sections for $^{55}Mn(n,2n)^{54}Mn$ reaction from different libraries.

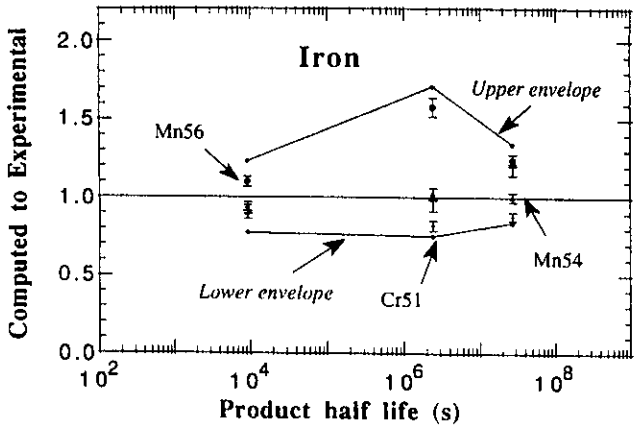

Fig. 43. Iron: Overall C/E dispersion for isotopic activities, using activation cross-section data contained in ACT4, REAC-3, DKR-ICF, and RACC libraries.

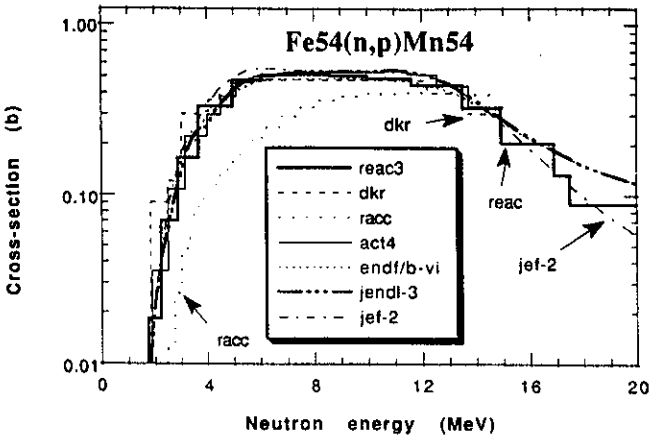

Fig. 46. Cross sections for $^{54}Fe(n,p)^{54}Mn$ reaction from different libraries.

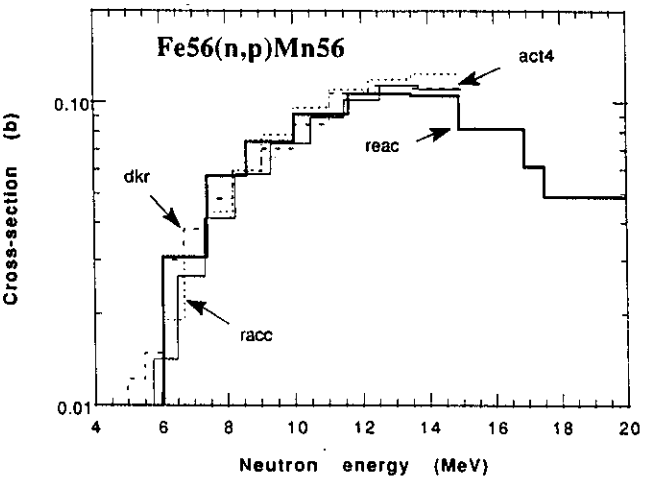

Fig. 44. Cross sections for $^{56}Fe(n,p)^{56}Mn$ reaction from different libraries.

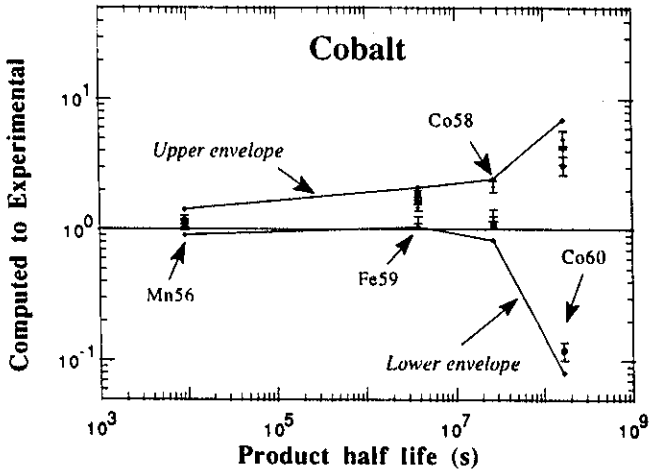

Fig. 47. Cobalt: Overall C/E dispersion for isotopic activities, using activation cross-section data contained in ACT4, REAC-3, DKR-ICF, and RACC libraries.

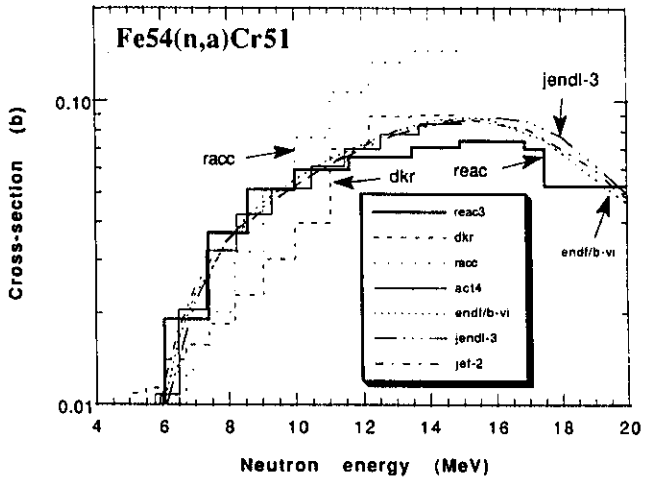

Fig. 45. Cross sections for $^{54}Fe(n,\alpha)^{51}Cr$ reaction from different libraries.

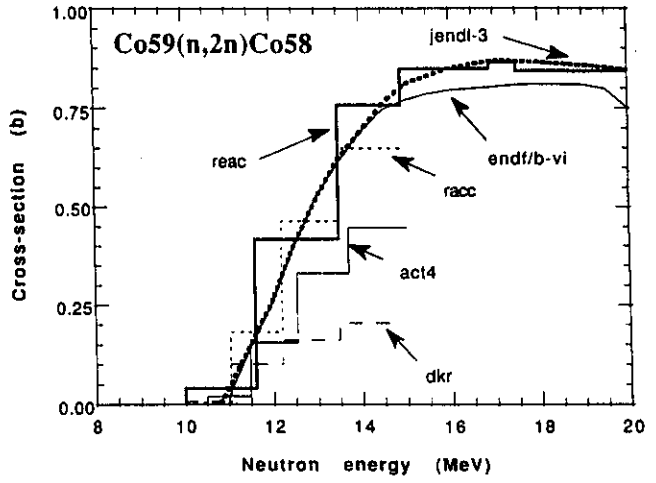

Fig. 48. Cross sections for $^{59}Co(n,2n)^{58}Co$ reaction from different libraries.

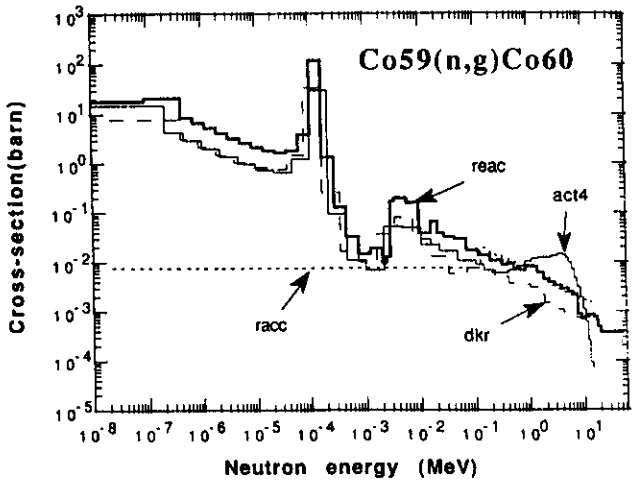

Fig. 49. Cross sections for $^{59}Co(n,\gamma)^{60}Co$ reaction from different libraries.

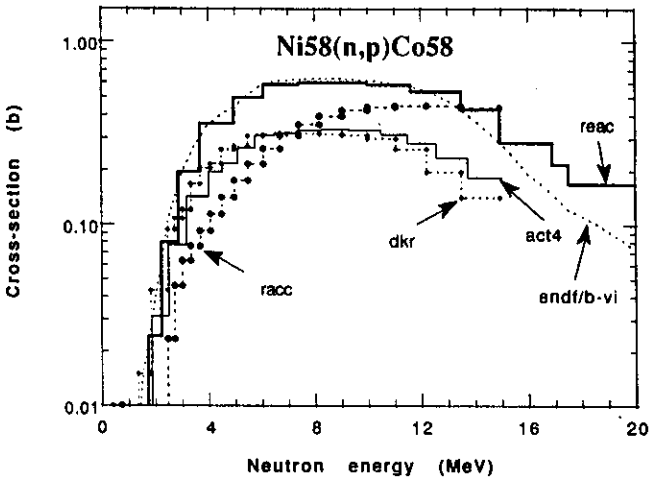

Fig. 52. Cross sections for $^{58}Ni(n,p)^{58}Co$ reaction from different libraries.

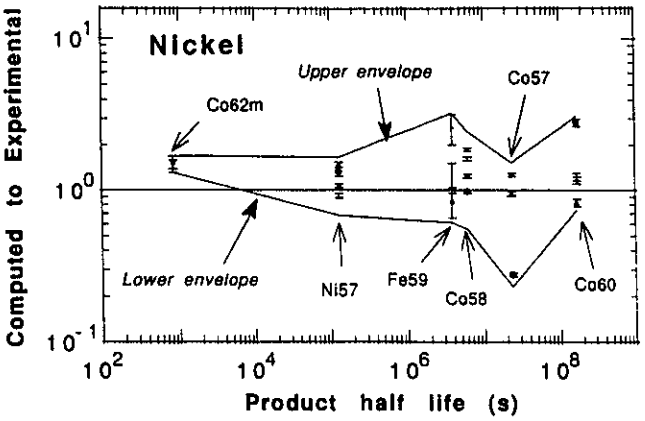

Fig. 50. Nickel: Overall C/E dispersion for isotopic activities, using activation cross-section data contained in ACT4, REAC-3, DKR-ICF, and RACC libraries.

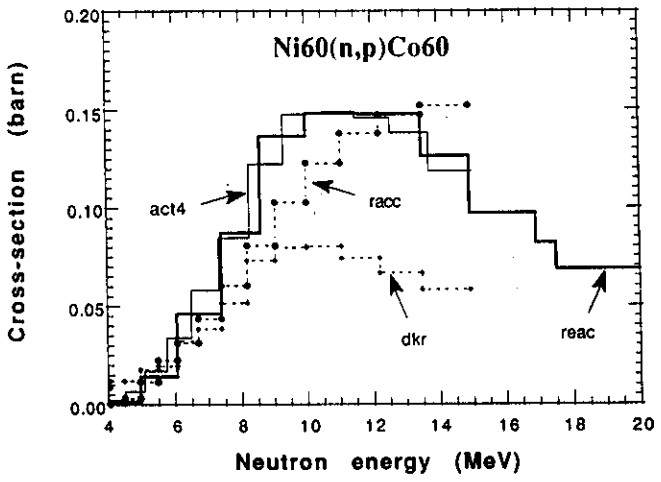

Fig. 53. Cross sections for $^{60}Ni(n,p)^{60}Co$ reaction from different libraries.

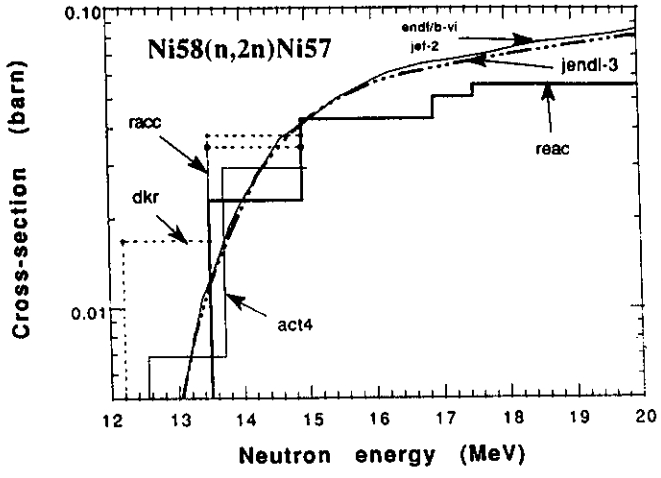

Fig. 51. Cross sections for $^{58}Ni(n,2n)^{57}Ni$ reaction from different libraries.

$^{63}Cu(n,\alpha)^{60m}Co$, the latter reaction being an important contributor to the production of ^{60}Co. In addition, the RACC library does not have cross sections for $^{65}Cu(n,p)^{65}Ni$.

V.K. Zinc

Figure 58 is a plot of C/Es for zinc. The data for three spectral locations, i.e., C, F, and L, are considered. The cross sections are plotted as a function of energy for the $^{70}Zn(n,2n)^{69m}Zn$, $^{67}Zn(n,p)^{67}Cu$, and $^{66}Zn(n,2n)^{65}Zn$ reactions in Figs. 59, 60, and 61. No cross-section data were found for these and other important reactions in the ENDF/B-VI, JENDL-3, and JEF-2 libraries. The RACC cross-section shapes and values are widely different compared with the other libraries (see Table XVII). In fact, CSIs for both the

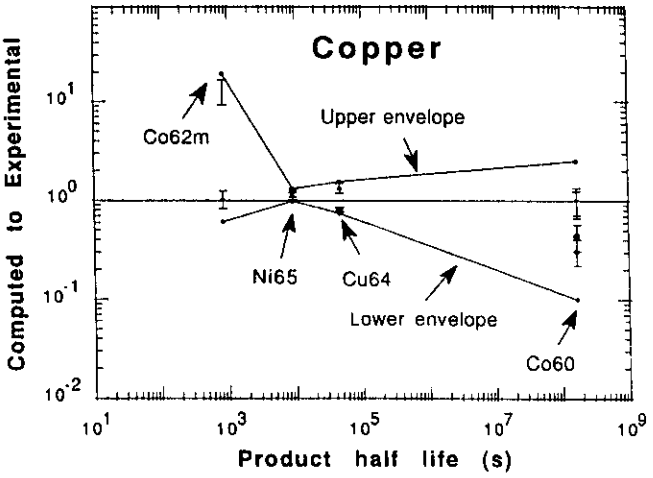

Fig. 54. Copper: Overall C/E dispersion for isotopic activities, using activation cross-section data contained in ACT4, REAC-3, DKR-ICF, and RACC libraries.

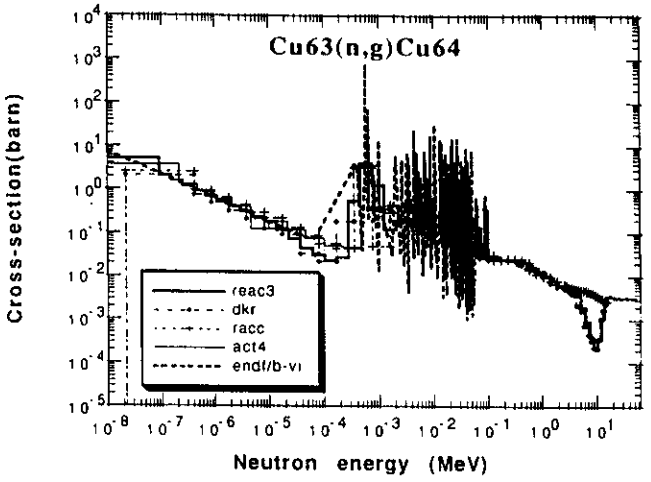

Fig. 56. Cross sections for $^{63}Cu(n,\gamma)^{64}Cu$ reaction from different libraries.

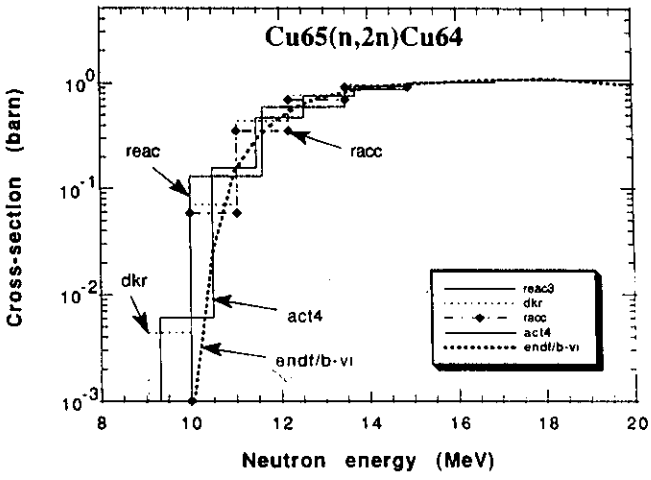

Fig. 55. Cross sections for $^{65}Cu(n,2n)^{64}Cu$ reaction from different libraries.

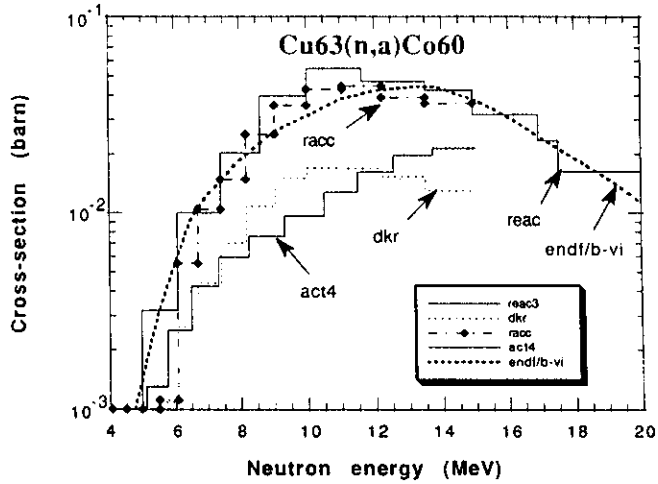

Fig. 57. Cross sections for $^{63}Cu(n,\alpha)^{60}Co$ reaction from different libraries.

$^{67}Zn(n,p)^{67}Cu$ and $^{66}Zn(n,2n)^{65}Zn$ reactions in the RACC library are almost an order lower compared with those for the other three libraries. The RACC cross section for the $^{66}Zn(n,2n)^{65}Zn$ reaction drops to zero below ~13.5 MeV. As for the $^{67}Zn(n,p)^{67}Cu$ reaction, the cross section drops to zero below ~14 MeV. Wide divergences are observed among the cross sections in all the libraries, as is quite evident from the plots. Also, the CSIs for these reactions differ significantly from each other (see Table XVII).

The RACC library does not have cross-section data for $^{70}Zn(n,2n)^{69m}Zn$ and $^{68}Zn(n,np/d)^{67}Cu$. This leads to serious underestimation of the ^{69m}Zn production by RACC as the other contributing reaction $^{68}Zn(n,\gamma)^{69m}Zn$ does not account for much for the neutron energy spectra covered. In addition, it has low contributions to ^{65}Zn: The $^{66}Zn(n,2n)^{65}Zn$ rate is a factor of 2 to 10 lower compared with the other libraries, depending on the neutron energy spectrum, and the $^{64}Zn(n,\gamma)^{65}Zn$ reaction rate is four to six orders lower compared with the other libraries, again depending on the neutron energy spectrum.

V.L. Zirconium

Figure 62 is a plot of C/Es for zirconium. The data for two spectral locations, i.e., A and C, are considered. It is evident from this figure as well as Table XX that the large C/E dispersions are present for all the observed isotopic products. The cross sections are plotted as a function of energy for the $^{94}Zr(n,p)^{94}Y$, $^{96}Zr(n,\gamma)^{97}Zr$, $^{90}Zr(n,2n)^{89m}Zr$, $^{90}Zr(n,2n)^{89}Zr$, and

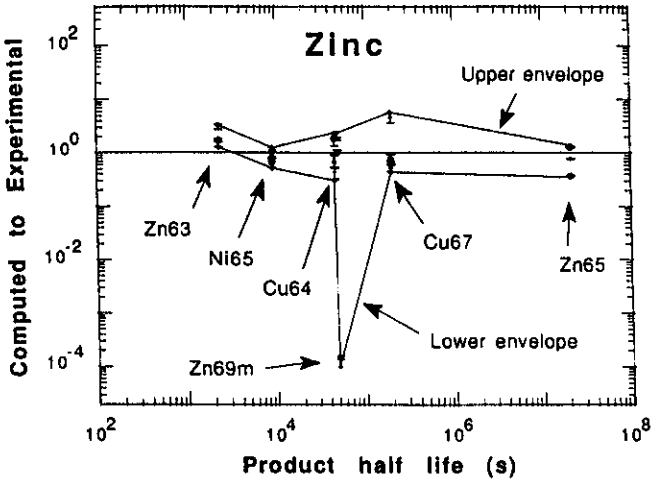

Fig. 58. Zinc: Overall C/E dispersion for isotopic activities, using activation cross-section data contained in ACT4, REAC-3, DKR-ICF, and RACC libraries.

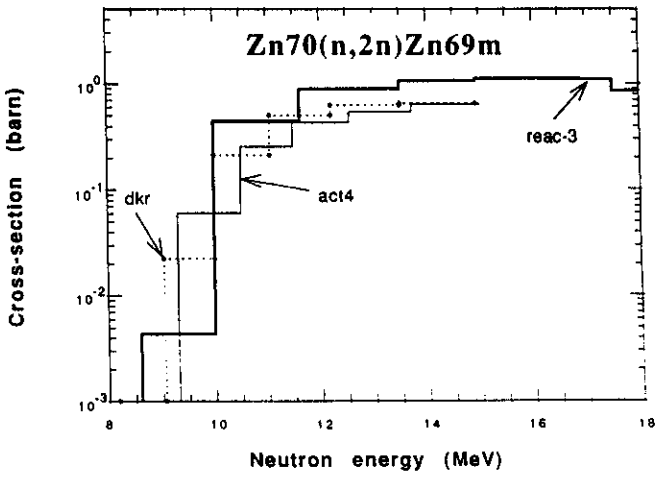

Fig. 59. Cross sections for $^{70}Zn(n,2n)^{69m}Zn$ reaction from different libraries.

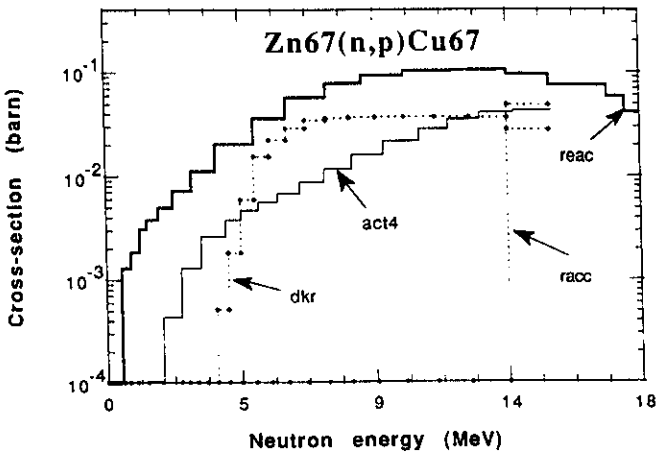

Fig. 60. Cross sections for $^{67}Zn(n,p)^{67}Cu$ reaction from different libraries.

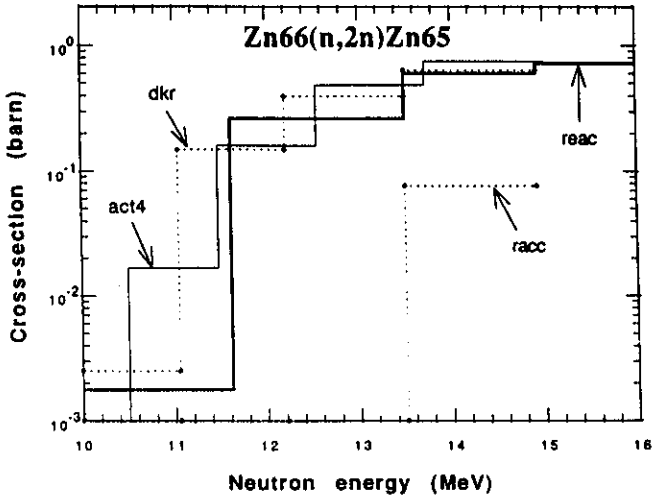

Fig. 61. Cross sections for $^{66}Zn(n,2n)^{65}Zn$ reaction from different libraries.

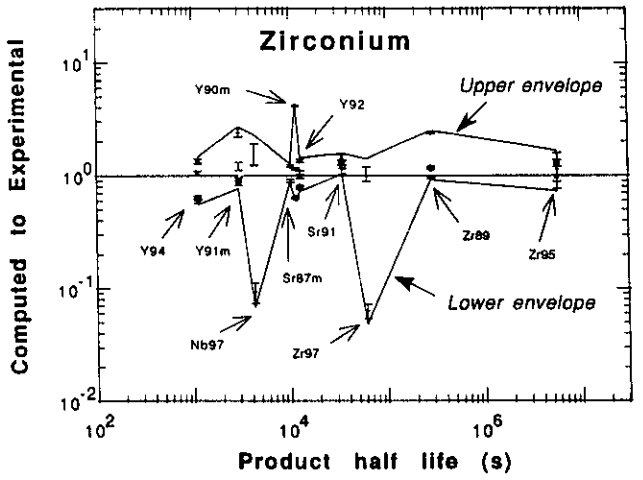

Fig. 62. Zirconium: Overall C/E dispersion for isotopic activities, using activation cross-section data contained in ACT4, REAC-3, DKR-ICF, and RACC libraries.

$^{96}Zr(n,2n)^{95}Zr$ reactions in Figs. 63 through 67. The RACC and DKR-ICF libraries do not have a cross section for $^{96}Zr(n,\gamma)^{97}Zr$. The ENDF/B-VI cross sections are also plotted for $^{94}Zr(n,p)^{94}Y$, $^{90}Zr(n,2n)^{89}Zr$, and $^{96}Zr(n,2n)^{95}Zr$. Wide divergences are observed in the cross sections in all the libraries. The REAC-3 library yields very low C/Es for both ^{97}Zr and ^{97}Nb. In fact, the production reaction for both these isotopes is $^{96}Zr(n,\gamma)^{97}Zr$. As can be seen from Fig. 64 and Table XVI, the cross sections for the ACT4 and REAC-3 libraries differ sharply in the various energy regions. The C/E trends can even undergo reversal for these two libraries under different spectra. Note that the $^{94}Zr(n,\gamma)^{95}Zr$ reaction cross section for these two libraries has similar problem, but because of the dominant contribution

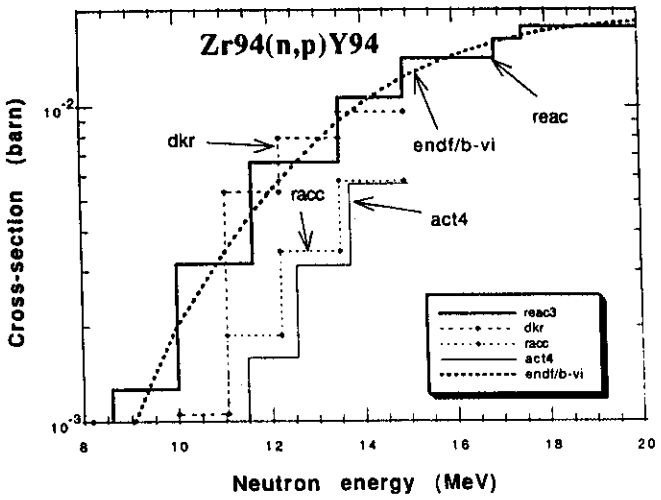

Fig. 63. Cross sections for $^{94}Zr(n,p)^{94}Y$ reaction from different libraries.

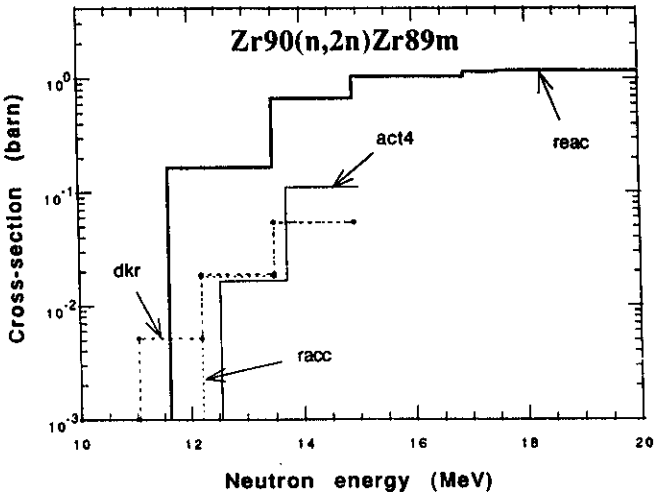

Fig. 65. Cross sections for $^{90}Zr(n,2n)^{89m}Zr$ reaction from different libraries.

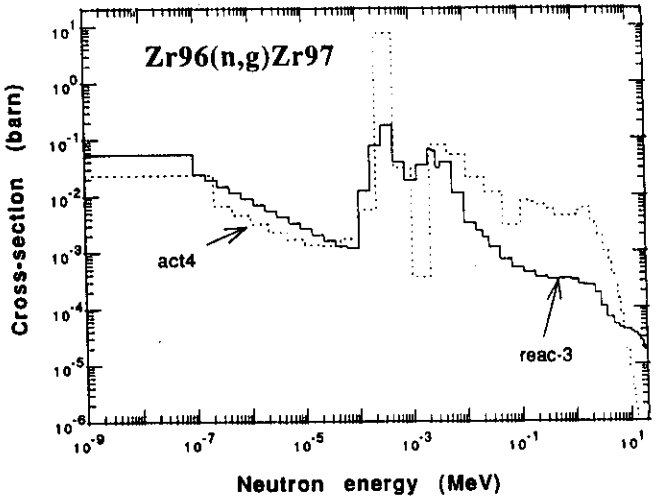

Fig. 64. Cross sections for $^{96}Zr(n,\gamma)^{97}Zr$ reaction from different libraries.

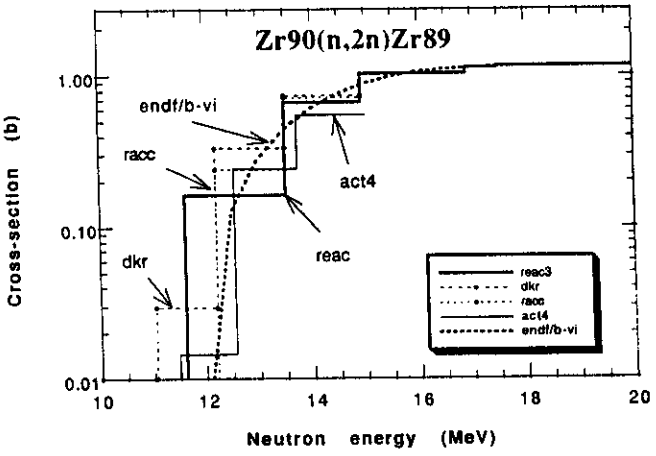

Fig. 66. Cross sections for $^{90}Zr(n,2n)^{89}Zr$ reaction from different libraries.

of the competing nuclear reaction $^{96}Zr(n,2n)^{95}Zr$, the C/E dispersions for the ^{95}Zr activity do not show similar erratic behavior. In addition, REAC-3 largely overpredicts the contribution of ^{89m}Zr to ^{89}Zr production almost up to a factor of 2 higher for most of the situations of interest, compared with the other libraries. This is due to a larger cross section for the $^{90}Zr(n,2n)$-^{89m}Zr reaction in the REAC-3 library.

Let us now look at the librarywise behavior for C/Es. The DKR-ICF and RACC libraries do not have cross-section data for the $^{96}Zr(n,\gamma)^{97}Zr$, $^{90}Zr(n,\alpha)$-^{87m}Sr, and $^{91}Zr(n,n'\alpha)^{87m}Sr$ reactions. In addition, RACC does not have cross sections for $^{94}Zr(n,\gamma)^{95}Zr$. The ACT4 and RACC cross sections for the $^{94}Zr(n,p)$-^{94}Y reaction are much lower than those for ENDF/

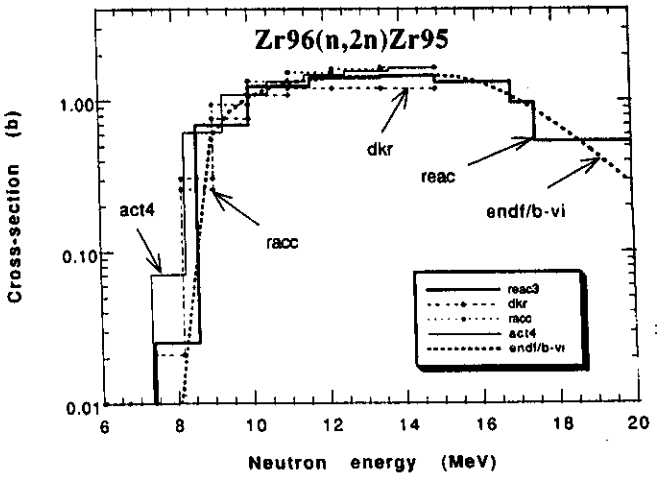

Fig. 67. Cross sections for $^{96}Zr(n,2n)^{95}Zr$ reaction from different libraries.

B-VI, REAC-3, and DKR-ICF. This explains systematically lower C/E values for ^{94}Y activity for these two libraries. For ^{90m}Y, both DKR-ICF and RACC yield almost identical but systematically low C/Es. The only contributing reaction for these two libraries is ^{90}Zr$(n,p)^{90m}$Y. There is one more contributor in the ACT4 library: ^{91}Zr$(n,np)^{90m}$Y. The REAC-3 library has two additional reaction channels: ^{91}Zr$(n,d)^{90m}$Y and ^{92}Zr$(n,nd)^{90m}$Y. The most dominant contributor for both the ACT4 and REAC-3 libraries is ^{90}Zr(n,p)-^{90m}Y. However, for example, the REAC-3 reaction rate for this channel is ~3.7 times that from ACT4. The ^{91}Zr$(n,np)^{90m}$Y channel contributes ~3% to the ^{90m}Y activity in ACT4 and ~1.5% in REAC-3. The combined fractional contribution of three minor channels to the total ^{90m}Y activity from the REAC-3 library is ~4%. But, this contribution by REAC-3 in itself is almost ~15% of the total ^{90m}Y activity from ACT4! It implies that the REAC-3 cross sections for the secondary channels also add to the overprediction of the ^{90m}Y activity.

V.M. Niobium

Figure 68 is a plot of C/Es for niobium. The data for four spectral locations, i.e., A, C, E, and K, are considered. The JENDL-3 dosimetry cross sections were also used for ^{93}Nb$(n,2n)$Nb^{92m}. The cross sections are plotted as a function of energy for the ^{93}Nb$(n,\alpha)^{90m}$Y and ^{93}Nb$(n,2n)^{92m}$Nb reactions in Figs. 69 and 70. The RACC and DKR-ICF libraries do not have cross sections for ^{93}Nb$(n,\alpha)^{90m}$Y. The JENDL-3 dosimetry cross sections are also plotted for ^{93}Nb$(n,2n)^{92m}$Nb. Significant deviations are observed in the cross sections in all the libraries. The CSIs for both reactions differ widely among the libraries (see Table XVI). Figure 71

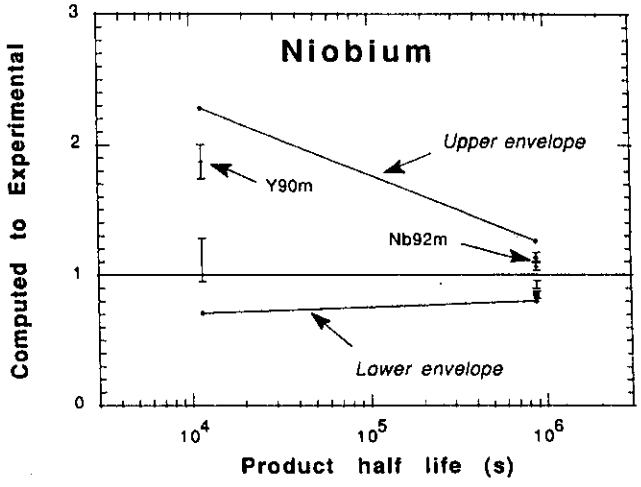

Fig. 68. Niobium: Overall C/E dispersion for isotopic activities, using activation cross-section data contained in ACT4, REAC-3, DKR-ICF, and RACC libraries.

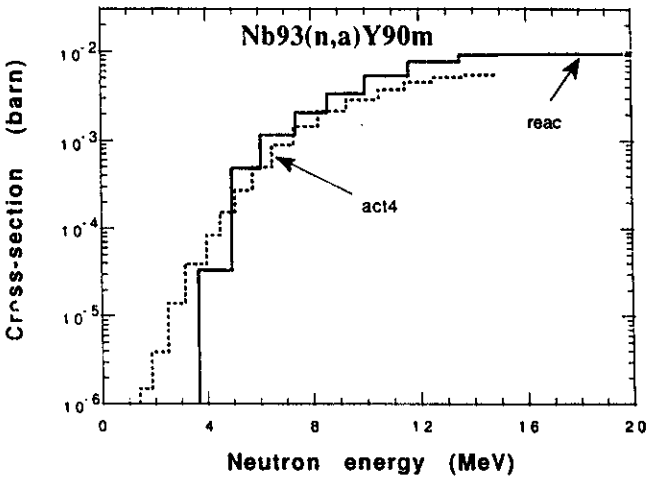

Fig. 69. Cross sections for ^{93}Nb$(n,\alpha)^{90m}$Y reaction from different libraries.

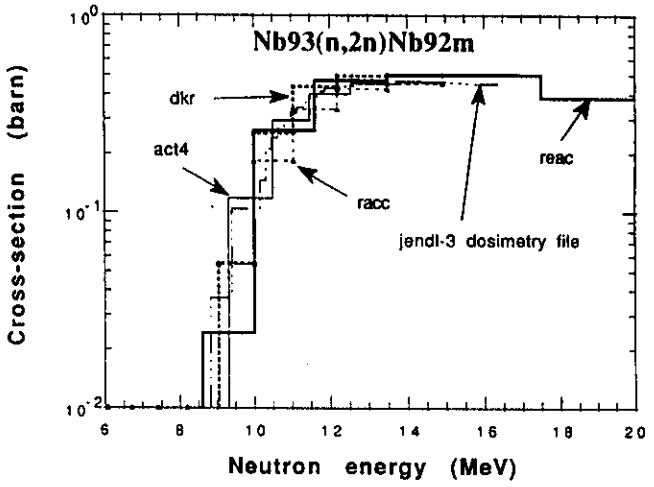

Fig. 70. Cross sections for ^{93}Nb$(n,2n)^{92m}$Nb reaction from different libraries.

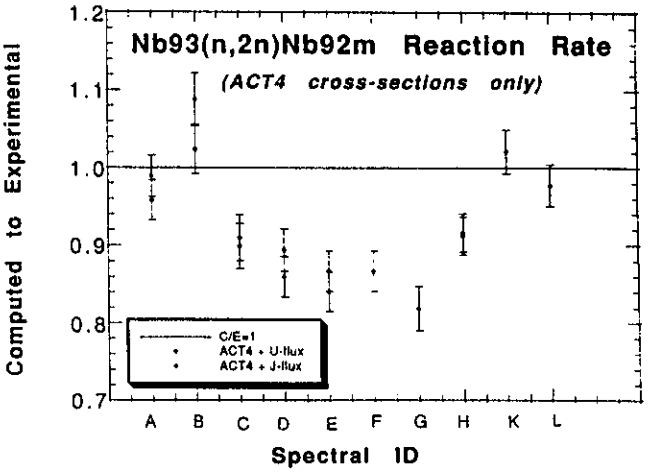

Fig. 71. The C/Es for ^{93}Nb$(n,2n)^{92m}$Nb activity for spectral locations A through L with ACT4 cross sections.

shows C/Es for $^{93}Nb(n,2n)^{92m}Nb$ for the spectral locations A through L with the ACT4 cross-section data. Both the United States and Japan fluxes have been utilized. One can observe that C/Es deviate considerably from unity even for this relatively well-known dosimetry reaction.

V.N. Molybdenum

Figure 72 is a plot of C/Es for molybdenum. The data for two spectral locations, i.e., A and C, are considered. The cross sections are plotted as a function of energy for the $^{92}Mo(n,2n)^{91m}Mo$, $^{92}Mo(n,2n)^{91}Mo$, $^{94}Mo(n,2n)^{93m}Mo$, $^{92}Mo(n,\gamma)^{93m}Mo$, $^{96}Mo(n,p)$-^{96}Nb, $^{100}Mo(n,2n)^{99}Mo$, and $^{95}Mo(n,p)^{95m}Nb$ reactions in Figs. 73 through 79, respectively. The RACC library does not have cross sections for $^{92}Mo(n,2n)$-^{91m}Mo and $^{94}Mo(n,2n)^{93m}Mo$. Note that ^{91}Nb is produced by β^- decay of ^{91}Mo. Wide divergences are observed in the cross sections in all the libraries. Although cross sections for $^{100}Mo(n,\gamma)^{101}Mo$ are not shown, large divergences are observed among the four libraries on one hand and vis-a-vis ENDF/B-VI on the other.

We see important differences among C/Es from different libraries. On ^{93m}Mo production predictability, there are two contributing channels: $^{94}Mo(n,2n)$-^{93m}Mo and $^{92}Mo(n,\gamma)^{93m}Mo$. Only two libraries, i.e., ACT4 and REAC-3, have cross sections for the $^{92}Mo(n,\gamma)^{93m}Mo$ channel. The fractional contributions from this channel in the two libraries are very different. For example, for spectrum A, the fractional contributions of the $^{92}Mo(n,\gamma)^{93m}Mo$ channel are ~0.2 and ~75% for ACT4 and REAC-3, respectively. The cross sections for the $^{92}Mo(n,\gamma)^{93m}Mo$ reactions in the two libraries are not only orders different but also

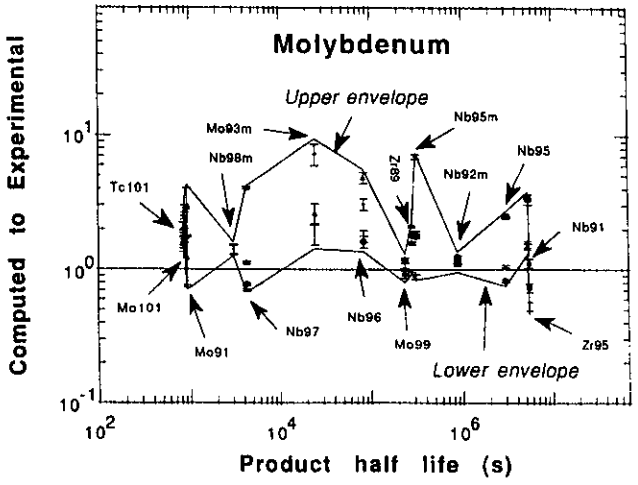

Fig. 72. Molybdenum: Overall C/E dispersion for isotopic activities, using activation cross-section data contained in ACT4, REAC-3, DKR-ICF, and RACC libraries.

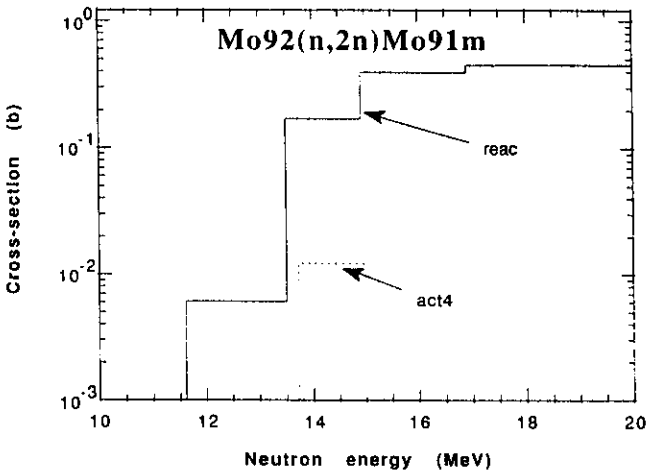

Fig. 73. Cross sections for $^{92}Mo(n,2n)^{91m}Mo$ reaction from different libraries.

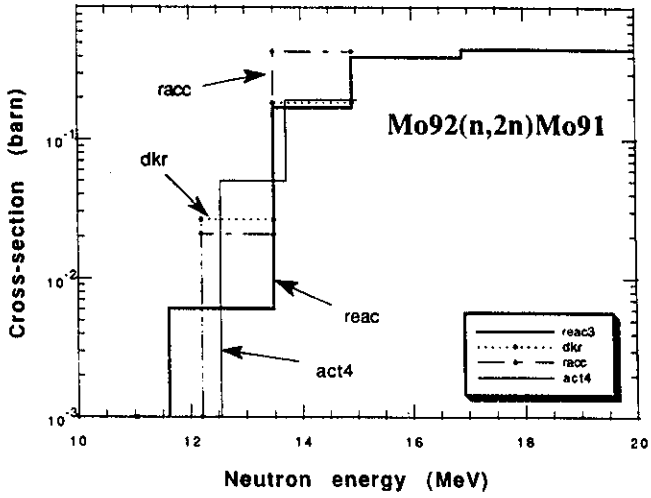

Fig. 74. Cross sections for $^{92}Mo(n,2n)^{91}Mo$ reaction from different libraries.

have divergent energy-wise dependence, as shown in Fig. 76. In fact, the ACT4 shape does not conform to the usual trend of an (n,γ) reaction at lower neutron energies; usually, the cross section for such reactions has $1/v$ dependence at low neutron energies.

As for ^{89}Zr, both DKR-ICF and RACC do not have cross sections for the $^{92}Mo(n,\alpha)^{89m}Zr$ channel. But, in spite of this, these two libraries along with REAC-3 have a systematic tendency to overpredict C/Es because of the significantly larger $^{92}Mo(n,\alpha)^{89}Zr$ channel in all these three libraries. In fact, the contributions to ^{89}Zr from $^{92}Mo(n,\alpha)^{89}Zr$ alone, in descending order for the four libraries, are: RACC, DKR-ICF, REAC-3, and ACT4. In fact, overall, ACT4 yields the best C/Es.

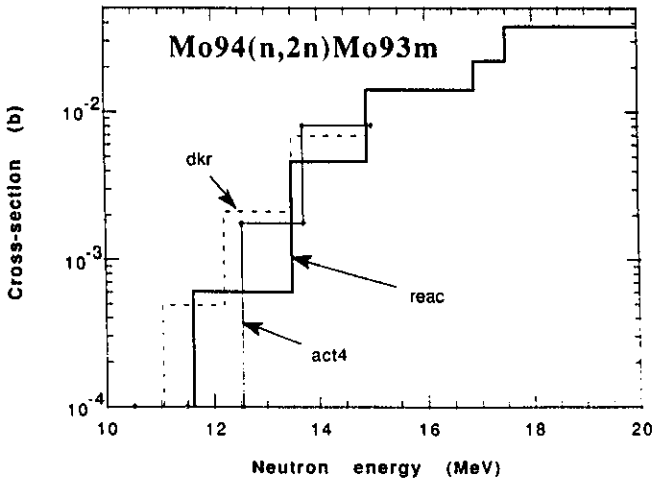

Fig. 75. Cross sections for $^{94}Mo(n,2n)^{93m}Mo$ reaction from different libraries.

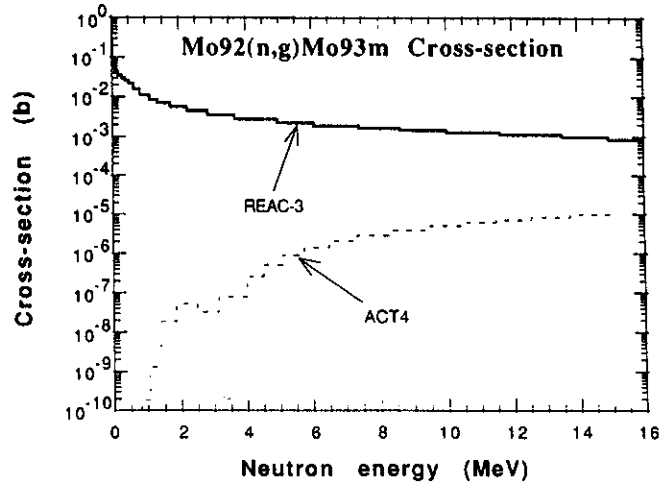

Fig. 76. Cross sections for $^{92}Mo(n,\gamma)^{93m}Mo$ reaction from different libraries.

For ^{91}Mo, both the DKR-ICF and RACC libraries do not have cross sections for the $^{92}Mo(n,2n)^{91m}Mo$ channel. In spite of this, RACC yields the largest C/Es for ^{91}Mo. The REAC-3 library shows almost as much as ~36% of contribution from the $^{92}Mo(n,2n)^{91m}Mo$ channel; for ACT4, this channel contributes ~3 % only. In fact, CSI for this channel from REAC-3 is an order larger than that from ACT4 (see Table XVI).

For ^{96}Nb, the DKR-ICF library yields a factor of 3 to 4 higher results above the other three libraries for the $^{96}Mo(n,p)^{96}Nb$ channel. This can be easily understood from the cross-section plots for this channel in Fig. 77. The REAC-3 library appears to have excessive contributions from three secondary channels, i.e., $^{97}Mo(n,np)^{96}Nb$, $^{97}Mo(n,d)^{96}Nb$, and $^{98}Mo(n,t)^{96}Nb$. In fact, the primary channel $^{96}Mo(n,p)^{96}Nb$

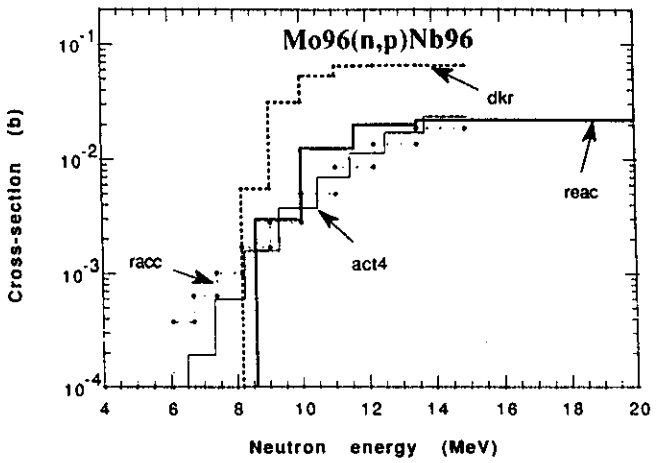

Fig. 77. Cross sections for $^{96}Mo(n,p)^{96}Nb$ reaction from different libraries.

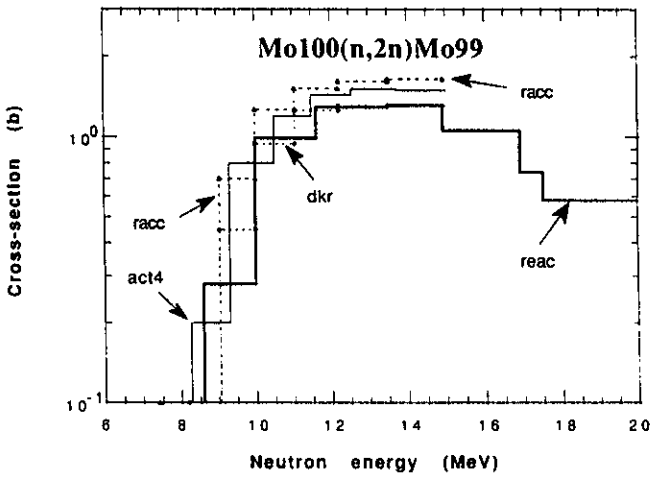

Fig. 78. Cross sections for $^{100}Mo(n,2n)^{99}Mo$ reaction from different libraries.

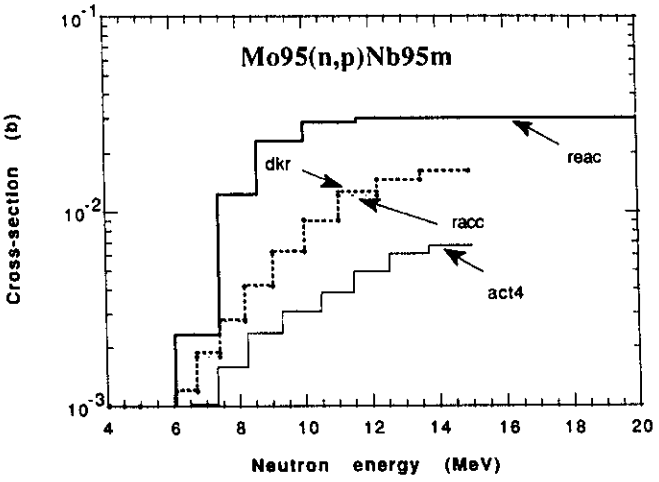

Fig. 79. Cross sections for $^{95}Mo(n,p)^{95m}Nb$ reaction from different libraries.

contributes only as much as ~50% by REAC-3, compared with ~94% by ACT4. All the libraries overpredict the ^{96}Nb production.

For ^{95m}Nb, REAC-3 has the largest cross section for the ^{95}Mo$(n,p)^{95m}$Nb channel whereas ACT4 has the lowest cross section; this is also reflected in CSIs (see Table XVI). In fact, REAC-3, DKR-ICF, and RACC predict much larger contributions from this channel compared with that by ACT4, the overprediction being as much as a factor of 2 to 5 larger. The REAC-3 library has large contributions from the secondary channels (see Table IX) too. These channels contribute as much as ~50% in REAC-3 whereas in ACT4 it amounts to ~10% only.

For ^{95}Nb, the trends observed for ^{95m}Nb have important impact, as ^{95m}Nb → ^{95}Nb channel makes a significant contribution. The DKR-ICF library predicts too large contribution by ^{95}Mo$(n,p)^{95}$Nb channel. In fact, the contribution by this library is ~2.5 times that by ACT4. REAC-3, again, has large contributions from the secondary channels (see Table IX); their contribution is as much as ~30% to the total.

For ^{97}Nb, one discovers very peculiar trends with all the libraries when one looks very closely at the finer, channelwise decompositions. Even though the C/E ranges predicted by ACT4 and RACC are rather close, the channelwise contributions are widely different even for these two libraries. For example, for the ^{97}Mo$(n,p)^{97}$Nb channel, RACC has the lowest contribution. The RACC contribution is almost ~70% of the ACT4 contribution. But, for the secondary channels of ^{98}Mo$(n,np/d)^{97}$Nb, the RACC contribution is as much as ~2.5 times that by ACT4. For ACT4, the secondary channels contribute ~20%; they contribute, respectively, ~45, ~30, and ~55% for RACC, DKR-ICF, and REAC-3.

V.O. Type 316 Stainless Steel

Figure 80 is a plot of C/Es for stainless steel. The data for three spectral locations, i.e., A, B, and C, are considered. The C/E dispersions are especially large for ^{57}Ni, ^{89}Zr, ^{99}Mo, ^{59}Fe, ^{58}Co, ^{57}Co, and ^{60}Co. Figures 81 through 84 show C/Es for the ACT4, REAC-3, DKR-ICF, and RACC libraries, respectively. Primarily, the trends observed for the steel components, i.e., Fe, Ni, Mn, Mo, and Co, are reflected in these figures. However, there could be compensating or complicating effects arising due to competing reaction channels from these component materials. The spectral integrals for these reaction channels differ widely among the four libraries. As for ^{51}Cr, the competing reaction channels come from Cr and Fe, e.g., ^{52}Cr$(n,2n)^{51}$Cr, and ^{50}Cr$(n,\gamma)^{51}$Cr from Cr, and ^{54}Fe$(n,\alpha)^{51}$Cr from Fe. For example, the contribution from Fe is as much as ~6% for spectrum A by ACT4. Manganese-56 receives contributions from Fe, Mn, and Co. Cobalt-58 gets contributions from Co and Ni. Iron-59 receives contributions from three materials, e.g., Co, Ni, and Fe. Manganese-54 receives comparable contributions from Fe and Mn. For example, ^{54}Fe$(n,p)^{54}$Mn contributes as much as ~60% for spectrum A, by the ACT4 library. Cobalt-60 receives contributions from Ni and Co. For ^{99}Mo, the major source of C/E divergence comes from ascendence of the ^{98}Mo$(n,\gamma)^{99}$Mo reaction channel as the neutron spectrum softens in going from spectrum A to B.

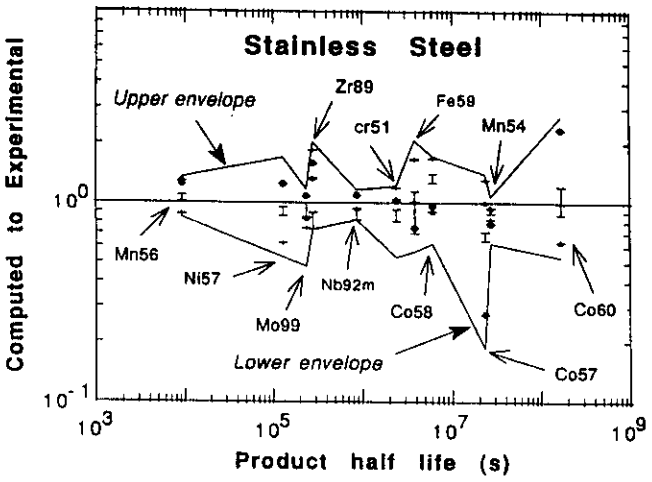

Fig. 80. Type 316 stainless steel: Overall C/E dispersion for isotopic activities, using activation cross-section data contained in ACT4, REAC-3, DKR-ICF, and RACC libraries.

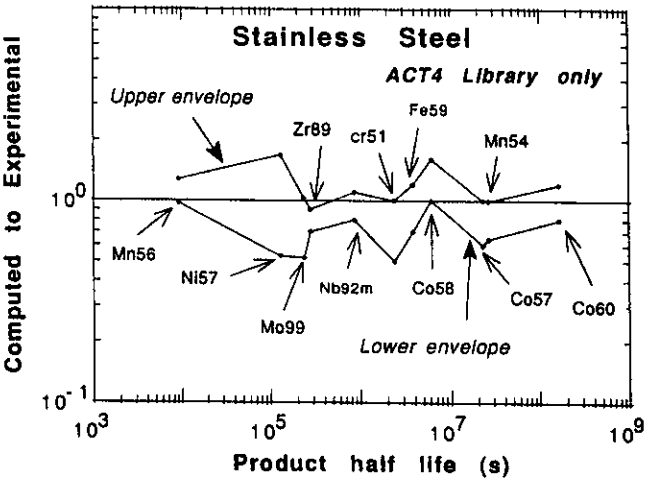

Fig. 81. Type 316 stainless steel: C/E dispersion for isotopic activities, using activation cross-section data contained in ACT4 library alone.

V.P. Indium

Figure 85 is a plot of C/Es for indium. The data for two spectral locations, i.e., A and C, are considered. The cross sections are plotted as a function of

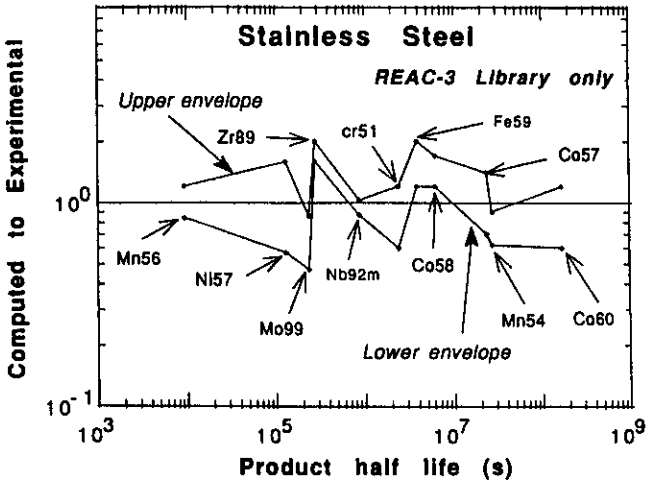

Fig. 82. Type 316 stainless steel: C/E dispersion for isotopic activities, using activation cross-section data contained in REAC-3 library alone.

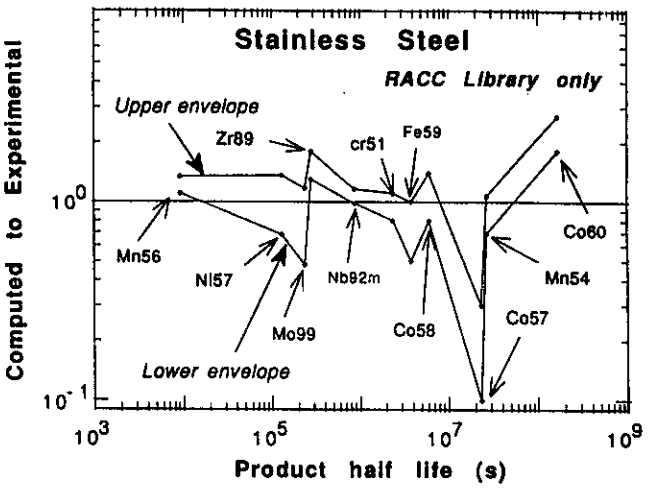

Fig. 84. Type 316 stainless steel: C/E dispersion for isotopic activities, using activation cross-section data contained in RACC library alone.

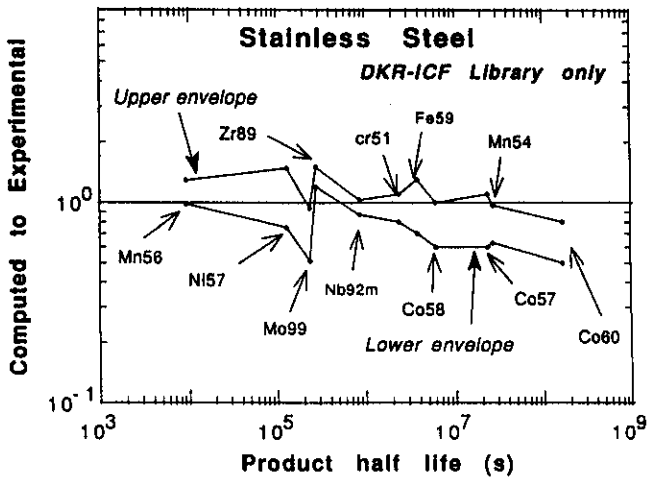

Fig. 83. Type 316 stainless steel: C/E dispersion for isotopic activities, using activation cross-section data contained in DKR-ICF library alone.

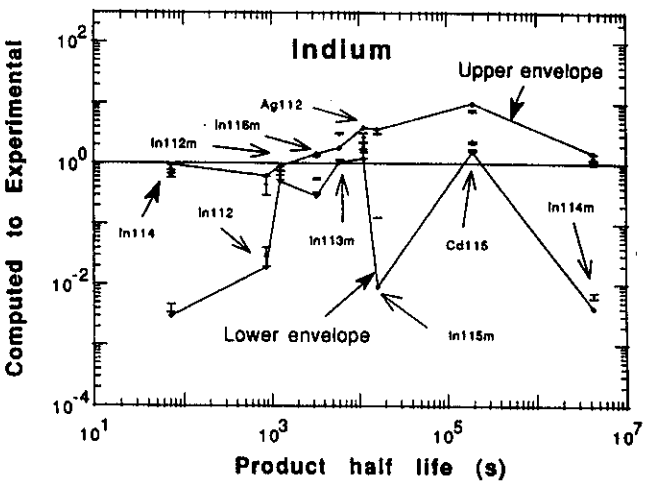

Fig. 85. Indium: Overall C/E dispersion for isotopic activities, using activation cross-section data contained in ACT4, REAC-3, DKR-ICF, and RACC libraries.

energy for the $^{115}In(n,2n)^{114}In$ and $^{115}In(n,2n)^{114m}In$ reactions in Figs. 86 and 87. The RACC and ACT4 libraries do not have cross sections for these reactions. Significant divergences are observed in the cross sections for the two libraries (REAC-3 and DKR-ICF). The RACC library does not have any cross sections for indium isotopes. Also, there are no cross section data in the DKR-ICF library for the following reactions: $^{113}In(n,2n)^{112m}In$, $^{113}In(n,n')^{113m}In$, and $^{115}In(n,n')^{115m}In$.

All the libraries underpredict ^{112}In. For DKR-ICF, this underprediction is rather strong because of the absence of the $^{113}In(n,2n)^{112m}In$ reaction channel that makes the dominant contribution to ^{112}In for the cooling times considered experimentally. The larger REAC-3 cross section for $^{113}In(n,n')^{113m}In$ leads to systematic overprediction of ^{113m}In by this library. All the libraries systematically overpredict ^{112}Ag. Indium-114*m* is seriously underpredicted by ACT4 because of the absence of a major contributor, i.e., $^{115}In(n,2n)^{114m}In$. Similarly, ^{114}In is seriously underpredicted by ACT4 because of the absence of a major contributor, i.e., $^{115}In(n,2n)^{114m}In \rightarrow {}^{114}In$. As for ^{115m}In, the $^{115}In(n,n')^{115m}In$ reaction channel is absent in ACT4. However, ^{115m}In receives contributions from two other reaction channels too (see Table XII). This is the sole reason C/Es are nonzero for ^{115m}In. The REAC-3 library appears to significantly overpredict the ^{115m}In

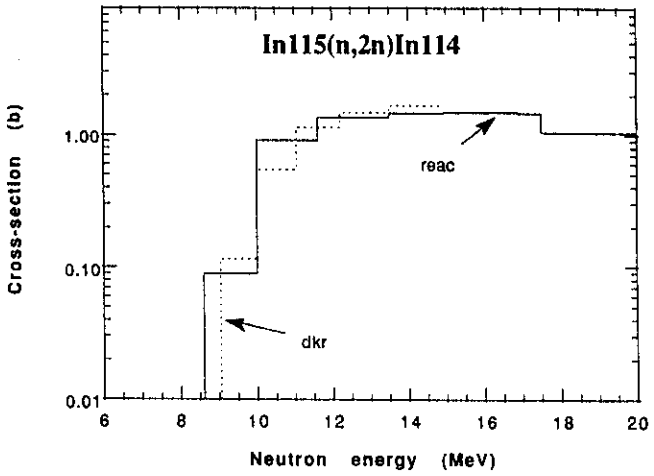

Fig. 86. Cross sections for $^{115}In(n,2n)^{114}In$ reaction from different libraries.

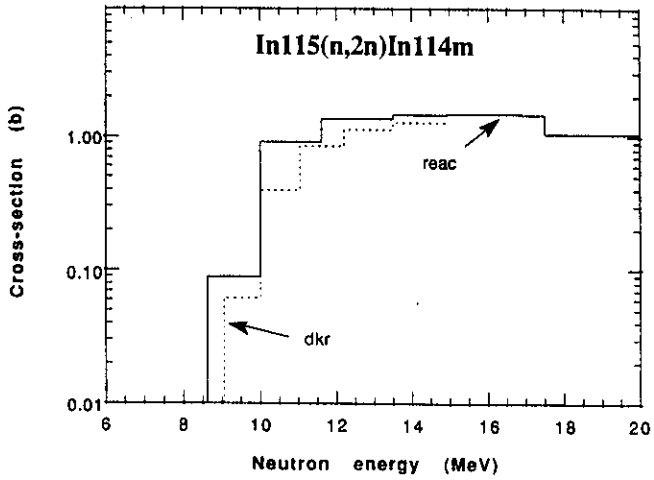

Fig. 87. Cross sections for $^{115}In(n,2n)^{114m}In$ reaction from different libraries.

contribution via the $^{115}In(n,n')^{115m}In$ channel. This channel contributes as much as ~80% to the total. As for ^{115}Cd, all the libraries overpredict, even as the REAC-3 cross section needs a much larger reduction.

V.Q. Tin

Figure 88 is a plot of C/Es for tin. The data for two spectral locations, i.e., C and E, are considered. The cross sections are plotted as a function of energy for the $^{117}Sn(n,p)^{117}In$, $^{116}Sn(n,p)^{116m}In$, $^{116}Sn(n,\gamma)^{117m}Sn$, $^{118}Sn(n,2n)^{117m}Sn$, and $^{114}Sn(n,2n)^{113}Sn$ reactions in Figs. 89 through 93. The JENDL-3 cross sections are also included for $^{114}Sn(n,2n)^{113}Sn$. Wide divergences are observed in the cross sections in all the libraries. The cross section shapes for the $^{116}Sn(n,\gamma)^{117m}Sn$ reaction

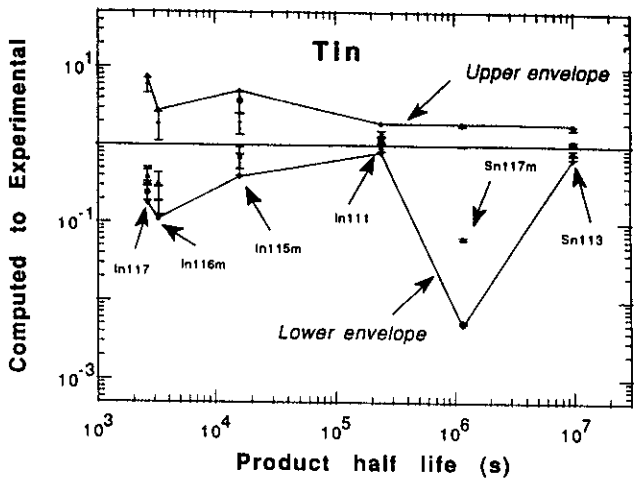

Fig. 88. Tin: Overall C/E dispersion for isotopic activities, using activation cross-section data contained in ACT4, REAC-3, DKR-ICF, and RACC libraries.

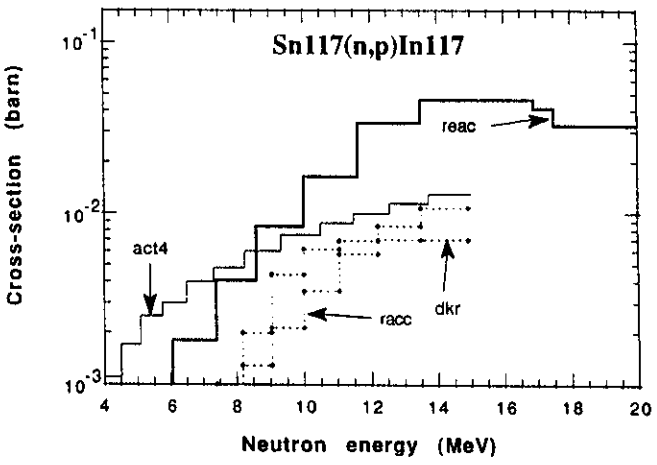

Fig. 89. Cross sections for $^{117}Sn(n,p)^{117}In$ reaction from different libraries.

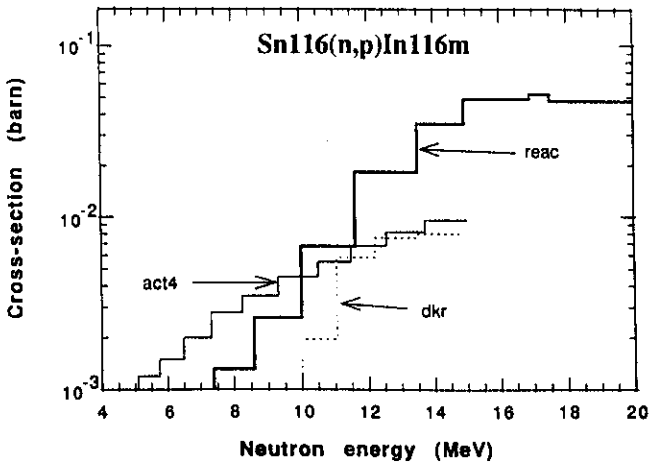

Fig. 90. Cross sections for $^{116}Sn(n,p)^{116m}In$ reaction from different libraries.

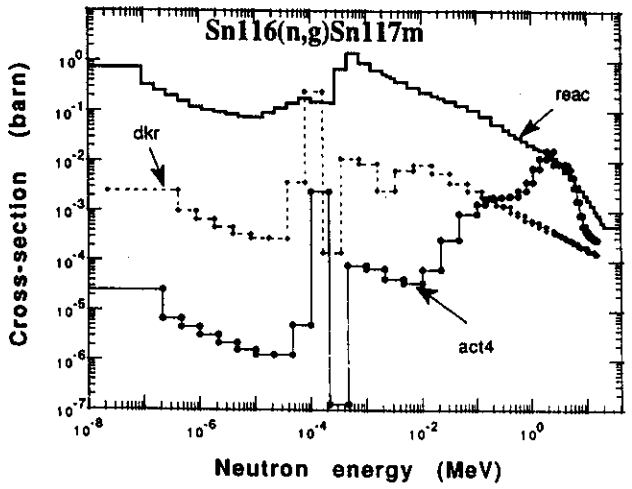

Fig. 91. Cross sections for $^{116}Sn(n,\gamma)^{117m}Sn$ reaction from different libraries.

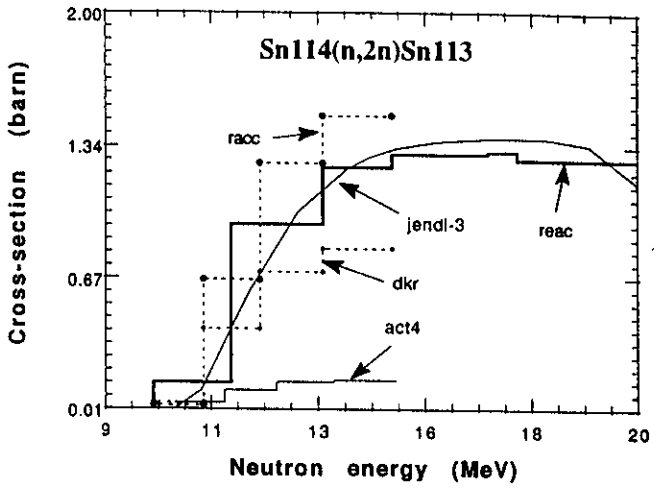

Fig. 93. Cross sections for $^{114}Sn(n,2n)^{113}Sn$ reaction from different libraries.

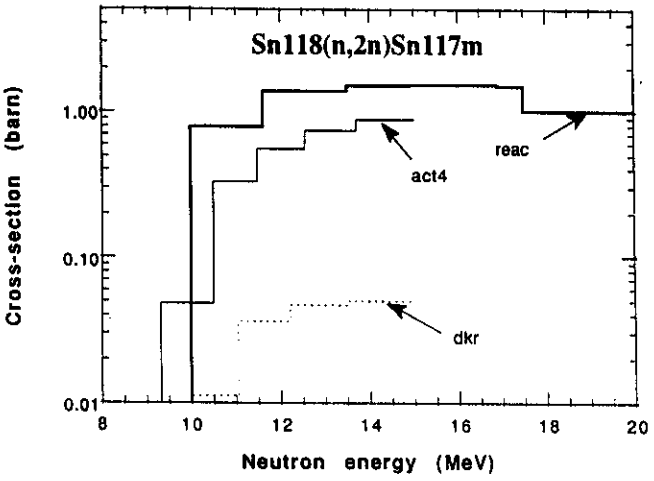

Fig. 92. Cross sections for $^{118}Sn(n,2n)^{117m}Sn$ reaction from different libraries.

are particularly noteworthy for orders of magnitudes differences among different libraries (see Fig. 91).

For ^{117}In, whereas REAC-3 strongly overpredicts, all the remaining libraries severely underpredict it. There are eight reaction channels contributing to the ^{117}In production (see Table XIII). The leading contributors are $^{117}Sn(n,p)^{117}In$ and $^{117}Sn(n,p)^{117m}In$. Whereas REAC-3 overpredicts the contributions from these two channels, all the other libraries severely underpredict. The cross-section shapes for the $^{117}Sn(n,p)^{117}In$ channel (see Fig. 89) are a typical demonstration of the status of the cross sections in all the libraries. The REAC-3 library has large, additional contributions from the secondary channels like $^{118}Sn(n,np/d)^{117m}In$ and $^{118}Sn(n,np/d)$-^{117}In also. For ^{116m}In, whereas REAC-3 tends to overpredict, both the ACT4 and DKR-ICF libraries seriously underpredict it. For example, the REAC-3 contribution from the leading channel of $^{116}Sn(n,np)^{116m}In$ is ~7 times that by ACT4, and ~4.5 times that by DKR-ICF for spectral location E (see Fig. 90 for the cross-section comparison). The contributions from the remaining two channels (see Table XIII) in REAC-3 account for as much as ~25% of total.

For ^{115m}In, whereas REAC-3 and RACC overpredict, both the ACT4 and DKR-ICF libraries underpredict it. For the cooling times covered, the one-step channels, i.e., $^{115}Sn(n,p)^{115m}In$, $^{116}Sn(n,np/d)^{115m}In$, and $^{117}Sn(n,t)^{115m}In$, make no contribution to ^{115m}In. The only contributors are $^{118}Sn(n,\alpha)^{115m}Cd \rightarrow {}^{115m}In$ and $^{118}Sn(n,\alpha)^{115}Cd \rightarrow {}^{115m}In$. The RACC and DKR-ICF libraries have cross sections for the $^{118}Sn(n,\alpha)^{115}Cd$ channel. The RACC prediction from this channel alone is ~2 times that by REAC-3. The ACT4 contributions appear to be low. For example, for the $^{118}Sn(n,\alpha)$-^{115m}Cd channel, the ACT4 prediction is about one-third of the REAC-3 prediction; for the $^{118}Sn(n,\alpha)^{115}Cd$ channel, the ACT4 calculation is only as much as ~0.3 times that by REAC-3.

For ^{117m}Sn, REAC-3 systematically overpredicts whereas DKR-ICF severely underpredicts it. In spite of the ten reaction channels contributing to the ^{117m}Sn production (see Table XIII), the main channel is $^{118}Sn(n,2n)^{117m}Sn$. The CSIs for this channel are listed in Table XVII. Only the ACT4 cross section appears reasonable (see Fig. 92). Whereas REAC-3 has too large a cross section, DKR-ICF has too low a cross section. For ^{113}Sn, both ACT4 and DKR-ICF underpredict whereas REAC-3 overpredicts it. The major difference between the ACT4 and REAC-3 predictions results from the $^{114}Sn(n,2n)^{113}Sn$ reaction channel. The ACT4 contribution from this channel is almost one-tenth of that by REAC-3 (see Fig. 93 and Table XVII). In addition, the $^{114}Sn(n,2n)^{113m}Sn \rightarrow {}^{113}Sn$ channel

appears to be significantly overpredicted by REAC-3. Indium-111 is a net result of five channels. However, the dominant contribution comes from the following two-step process: $^{112}Sn(n,2n)^{111}Sn \rightarrow {}^{111m}In \rightarrow {}^{111}In$. For example, this process alone accounts for as much as ~97% of the total for ACT4 and ~92, 100, and ~99%, respectively, for the REAC-3, DKR-ICF, and RACC libraries. The ACT4 prediction is comparable to that by RACC but is significantly above those by REAC-3 and ACT4.

V.R. Tantalum

Figure 94 is a plot of C/Es for tantalum. The data for three spectral locations, i.e., A, B, and C, are considered. There are no cross sections in ACT4 and RACC for computing ^{180m}Hf. Even though DKR-ICF has cross sections for $^{180}Ta(n,p)^{180m}Hf$, it has no cross section data for $^{181}Ta(n,np/d)^{180m}Hf$. As a result, DKR-ICF yields a very low C/E for ^{180m}Hf. The RACC library does not have cross sections for $^{181}Ta(n,2n)^{180m}Ta$. The cross sections are plotted as a function of energy for $^{181}Ta(n,p)^{181}Hf$ in Fig. 95. The ENDF/B-VI cross section is also plotted. Wide divergences are observed in the cross sections from all the libraries.

For ^{180m}Hf, the major contributors in REAC-3 are $^{181}Ta(n,np)^{180m}Hf$ and $^{181}Ta(n,d)^{180m}Hf$. In fact, they account for as much as ~94 and ~6%, respectively, to the total production. The REAC-3 library strongly overpredicts ^{180m}Hf. The DKR-ICF library does not have these major channels. As a result, its prediction comes entirely from $^{180}Ta(n,p)^{180m}Hf$. In fact, even for this channel, the DKR-ICF prediction is ~35% of that by REAC-3. The REAC-3 cross sections

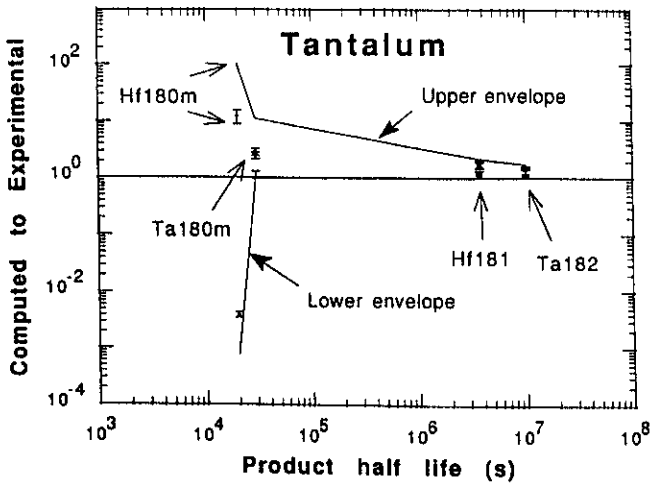

Fig. 94. Tantalum: Overall C/E dispersion for isotopic activities, using activation cross-section data contained in ACT4, REAC-3, DKR-ICF, and RACC libraries.

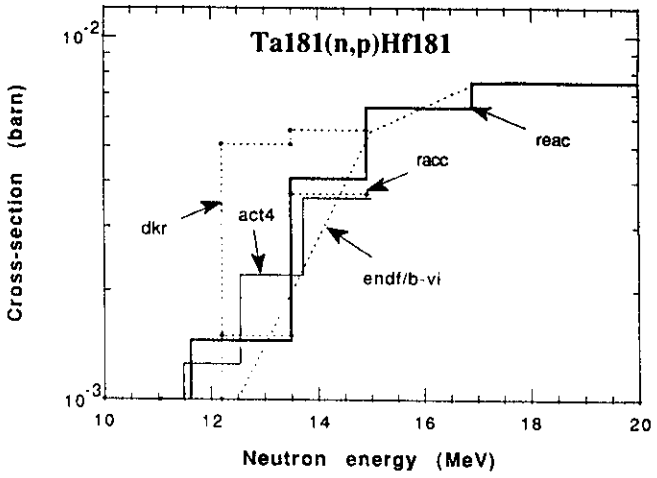

Fig. 95. Cross sections for $^{181}Ta(n,p)^{181}Hf$ reaction from different libraries.

for both the major channels need to be revised drastically. As for ^{180m}Ta, the cross section for $^{181}Ta(n,2n)^{180m}Ta$ appears to need large revision for all the libraries. Even the CSIs for this reaction differ widely for REAC3 and ACT4 (see Table XVI). For ^{181}Hf, both REAC-3 and DKR-ICF tend to overpredict by large amounts. The ACT4 and RACC predictions are closer to the experimental results. For ^{182}Ta, all the libraries overpredict. The RACC library has no cross section data for $^{181}Ta(n,\gamma)^{182m}Ta$ channel.

V.S. Tungsten

Figure 96 is a plot of C/Es for tungsten. The data for three spectral locations, i.e., A, B, and K, are considered. The ENDF/B-VI cross sections are also used for the $^{186}W(n,p)^{186}Ta$ and $^{184}W(n,p)^{184}Ta$ reactions. The cross sections are plotted as a function of energy for the $^{186}W(n,p)^{186}Ta$, $^{186}W(n,\alpha)^{183}Hf$, $^{184}W(n,p)^{184}Ta$, and $^{186}W(n,\gamma)^{187}W$ reactions in Figs. 97 through 100. Wide divergences are observed in the cross sections in all the libraries. Note that the ACT4 cross section for $^{186}W(n,\gamma)^{187}W$ drops rapidly above ~7 MeV.

Large differences are seen when one looks at C/E trends for individual libraries. For ^{186}Ta, C/E divergences are related in large measure to coarse energy group structures used in all four libraries. The cross-section shapes for ACT4, DKR-ICF, and RACC differ significantly with respect to ENDF/B-VI (see Fig. 97). For ^{182m}Ta, only REAC-3 has nonzero cross-section data. The cross sections for all the contributing channels (see Table XXII) appear to be excessive. For ^{183}Hf, REAC-3, DKR-ICF, and RACC systematically overpredict whereas ACT4 tends to underpredict. The cross-section shapes for $^{186}W(n,\alpha)^{183}Hf$ differ much (see Fig. 98). For ^{184}Ta, except for ACT4, all the libraries overpredict. The ACT4 library underpredicts a little.

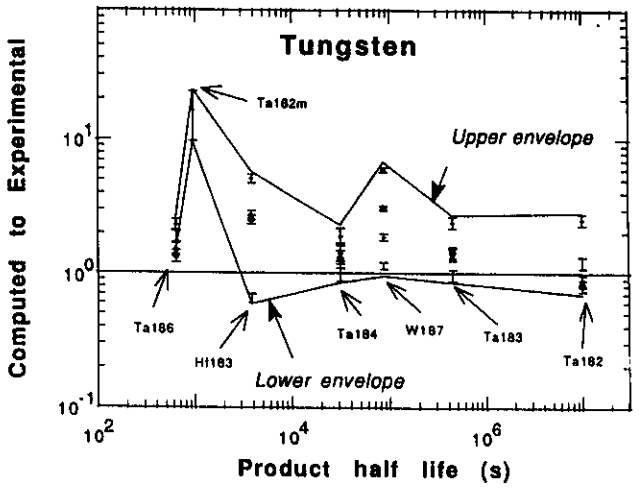

Fig. 96. Tungsten: Overall C/E dispersion for isotopic activities, using activation cross-section data contained in ACT4, REAC-3, DKR-ICF, and RACC libraries.

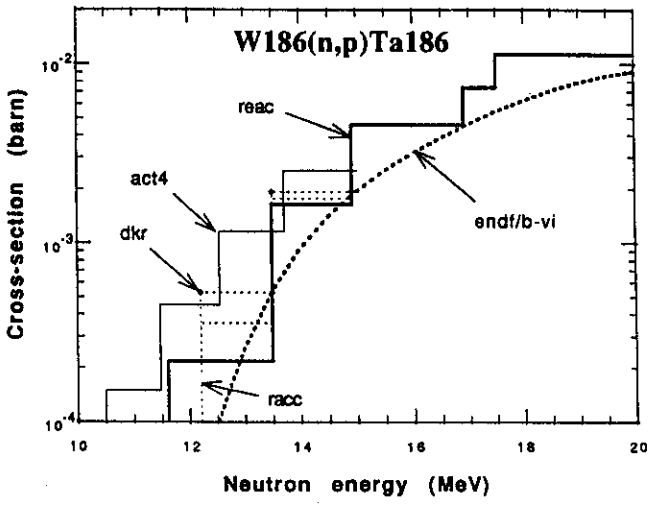

Fig. 97. Cross sections for $^{186}W(n,p)^{186}Ta$ reaction from different libraries.

Interestingly, except for ACT4, the shapes of the cross section for the $^{184}W(n,p)^{184}Ta$ reaction follow closely that given by ENDF/B-VI (see Fig. 94).

For ^{187}W, all the libraries have a tendency to overpredict. One of the major contributors is the cross-section representation for $^{186}W(n,\gamma)^{187}W$ in these libraries. As shown in Table XVI, the CSIs for this reaction differ widely from each other. In fact, DKR-ICF has the largest CSI, ~2.7 times that for ACT4. This discrepancy in cross-section representation leads to a discrepancy in C/Es for ^{187}W, the largest C/E being observed for DKR-ICF. For ^{183}Ta, REAC-3 tends to overpredict because of large contributions from ^{183}Hf

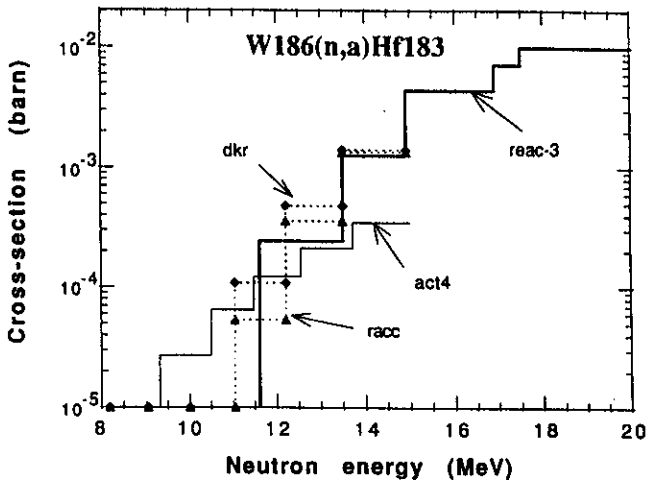

Fig. 98. Cross sections for $^{186}W(n,\alpha)^{183}Hf$ reaction from different libraries.

and $^{183}W(n,p)^{183}Ta$ (see Table XI). Even, DKR-ICF and RACC tend to overpredict because of the same reasons.

For ^{182}Ta, both DKR-ICF and RACC systematically underpredict. This is primarily because of the absence of reaction channels involving the production of ^{182m}Ta. In addition, there is underprediction for the lead channel $^{182}W(n,p)^{182}Ta$. The ACT4 prediction comes closest to the experimental numbers in spite of the absence of contributions from the ^{182m}Ta channels. The REAC-3 library on the other hand systematically overpredicts because of the following: first, possible overestimation of the contribution from the ^{182m}Ta channels. These channels contribute as much as ~50% of the total by REAC-3. This contribution

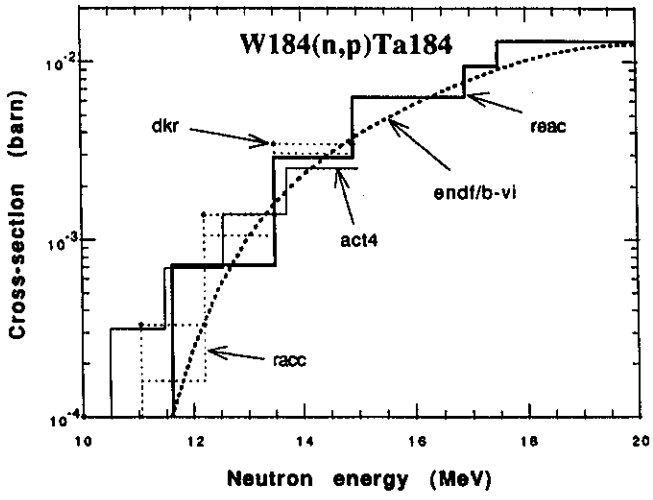

Fig. 99. Cross sections for $^{184}W(n,p)^{184}Ta$ reaction from different libraries.

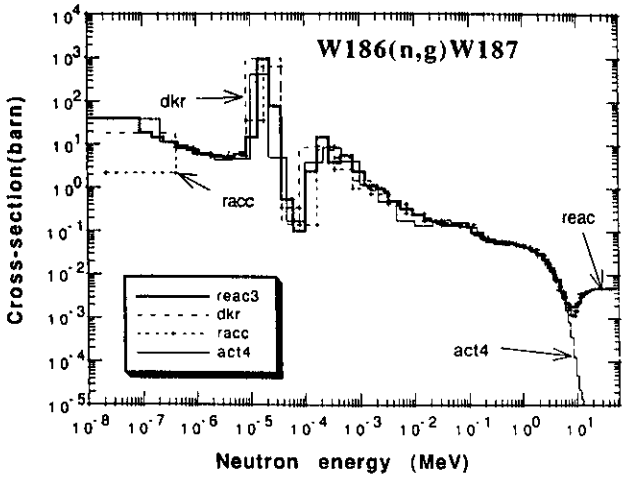

Fig. 100. Cross sections for $^{186}W(n,\gamma)^{187}W$ reaction from different libraries.

alone exceeds the total ^{182}Ta production rate predicted by ACT4. Second, the secondary channels for both ^{182m}Ta and ^{182}Ta make appreciable contributions. For example, for direct ^{182}Ta contributions alone, excluding $^{182m}Ta \rightarrow {}^{182}Ta$, the three secondary channels of $^{183}W(n,np)^{182}Ta$, $^{183}W(n,d)^{182}Ta$, and $^{184}W(n,t)^{182}Ta$ among themselves contribute as much as ~15%.

V.T. Lead

Figure 101 is a plot of C/Es for lead. The data for three spectral locations, i.e., C, F, and L, are considered. The JENDL-3 cross sections are also used for the $^{204}Pb(n,2n)^{203}Pb$ reaction. Except for REAC-3, no library has cross sections for $^{204}Pb(n,n')^{204m}Pb$ and/or $^{206}Pb(n,3n)^{204m}Pb$. As a result, the C/E dispersion for ^{204m}Pb is obtained from REAC-3 alone. The overprediction by REAC-3 is too high. This fact fits in with the general trend of REAC-3 of yielding a strong overprediction of the metastable state production cross sections. The cross sections are plotted as a function of energy for the $^{204}Pb(n,2n)^{203}Pb$ reaction in Fig. 102. Wide divergences are observed in the cross sections in all the libraries for this reaction. While ACT4 has a trend to underpredict ^{203}Pb production, RACC has a strong trend to overpredict. These trends are understandable in view of the cross-section shapes of these libraries (see Fig. 102).

VI. SAFETY/QUALITY FACTORS FOR ISOTOPIC RADIOACTIVITY

It is clear from the previous section that, in general, there is significant disagreement between the calculation and the experimental measurement for almost all the isotopic activities measured. Obviously, the calculated neutron energy spectrum and the activation cross sections used in the radioactivity calculations contribute to the disagreement. The inadequacies in radiation transport cross sections and geometrical/material modeling of the irradiated assembly are notable contributors to the uncertainties in the calculated neutron energy spectrum. In principle, it is possible to mitigate these inadequacies. However, the task of bringing out significant improvement in the whole range of activation cross sections itself requires an enormous amount of effort spread over many years.

The designers of a fusion machine need reliable information on neutron-induced radioactivity in its various components. The entire range of the neutron energy spectrum is involved in the radioactivity calculations. The machine component closest to the D-T

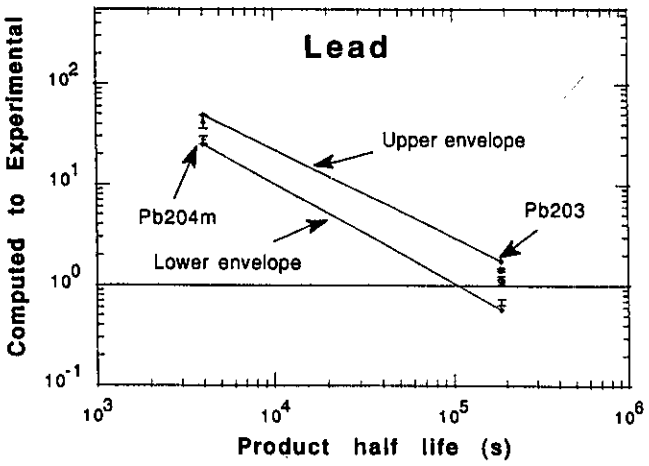

Fig. 101. Lead: Overall C/E dispersion for isotopic activities, using activation cross-section data contained in ACT4, REAC-3, DKR-ICF, and RACC libraries.

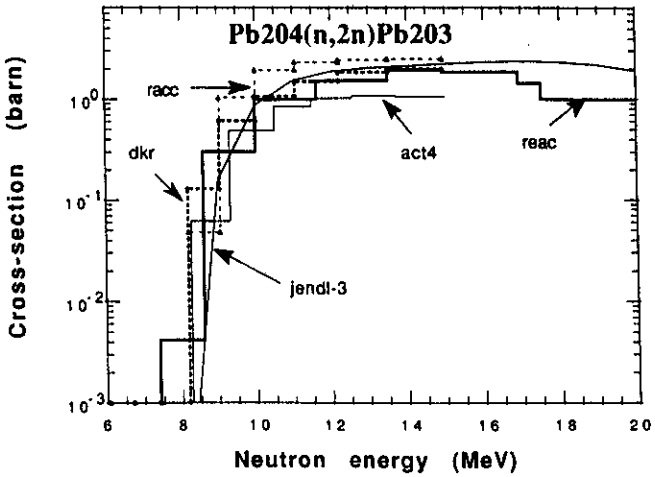

Fig. 102. Cross sections for $^{204}Pb(n,2n)^{203}Pb$ reaction from different libraries.

plasma sees the hardest spectrum; the one farthest from the plasma usually sees the softest spectrum. Be reminded that the (n,γ) reactions are preferably provoked by the low-energy part of the neutron energy spectrum, unlike the $(n,2n)$, (n,p), $(n,np/d)$, (n,t), and (n,α) reactions that are preferably provoked by the high-energy part of the spectrum. Thus, even for a machine component close to D-T plasma, low-energy as well as high-energy neutrons can induce radioactive isotopes of concern. The designers accept the inadequacies of modeling and the cross-section data and incorporate safety factors to come up with a somewhat conservative design.[35,36]

Underprediction or overprediction of radioactivity by a code is undesirable because of its implications for decay heat, safety, and waste-disposal. Ideally, one needs to correct the calculation, using a multiplier such that the corrected prediction is equal to the actual (experimental) amount of radioactivity. This correction factor for a code (and library) can be defined as

$$\text{ideal correction factor (ICF)} = 1/(C/E) ,$$

where the inverse of the observed C/Es defines the correction factor for a given isotopic activity. As long as one has access to a very large amount of C/E data for each observable isotopic activity, one can obtain the ICF and associated confidence level. The ICF can also be seen as a quality factor that is indicative of the quality of the ensemble of the cross-sectional library, computed neutron energy flux, and experimental data.

In practice, it is almost impossible to obtain the ICF as defined earlier because of problems associated with the impossibility of exact modeling of the experimental assembly, non-vanishing errors of the calculational method/code, and finite experimental error. Thus, one will rather be dealing with a distribution of correction factors.[37] If this distribution is statistically reliable, one can set a confidence level and obtain a correction factor that when multiplied to the calculated value yields a corrected calculational result that will be equal to or greater than the experimental value. Such a correction factor can be termed a safety factor. It is evident that the said safety factor will reduce to an ICF only when the associated probability distribution is a delta function centered at ICF; then, the confidence level in such a safety factor is 100%. However, it is almost impossible to obtain a delta function probability distribution of the safety factor (or correction factor). The realistic probability distributions could at best be Gaussian-like. The C/E results discussed in the preceding section can be utilized directly to estimate the safety factors for prediction of each induced isotopic radioactivity. But, the associated confidence level in the estimated safety factor for a number of isotopic activities may suffer because of a limited number of neutron energy spectra covered during measurements. In other words, such safety factors may not be reliable for use for a different neutron energy spectrum. In such a case, they may even turn out to be too large or too small. More reliable safety factors can be generated by conducting measurements under a wide range of neutron energy spectra.

A separate safety factor for each radioactive, isotopic product is needed. Any radioisotope can, given favorable conditions, make critical contributions to decay afterheat, biological dose, and biological hazard potential resulting from D-T neutron-induced radioactivity in a fusion machine. We must underline here that an ideal safety factor will be unity with cent percent confidence. Usually, the safety factor departs from unity. In a sense, the safety factor is a good indicator of the quality of the ensemble of the experimental data, the calculated neutron energy spectrum, and the activation cross-section library. Viewed this way, the safety factor can be termed a quality factor too.

VII. LIBRARY SELECTION FOR FUSION MACHINE DESIGN

At times, a designer may simply be interested in ascertaining general trends for a code/library regarding its prediction capability. In what follows, we have attempted to discern some collective and individual trends for four libraries used in the present work. As mentioned in the preceding section, a safety factor can be looked at as a sort of quality factor too. In principle, a separate quality factor can be associated with each library if all other parameters are held constant. Toward this end, first of all, we obtain a probability density distribution of C/Es irrespective of the type of isotopic activity, sample material, or neutron energy spectrum.[37] This probability distribution is normalized such that its integration over the entire C/E range from 0.0 to infinity yields exactly 1. Five such probability distributions have been obtained: one each for each of the four libraries and a consolidated one for all four libraries combined together. The consolidated probability distribution is shown as a function of C/E in Fig. 103. Also shown in Fig. 103 is a Gaussian distribution. This Gaussian distribution is obtained such that C/E of its peak is the same as that of the peak in the actual distribution and its full width at half maximum (FWHM) is the same as that of the peak in the actual distribution. The latter condition leads to obtention of the standard deviation of the Gaussian distribution. It is obvious from the figure that, away from the peak, the actual distribution differs widely from the Gaussian. Figure 104 provides a closer look at the peak. Also shown is the uncertainty in the consolidated probability density distribution for various C/Es. Figure 105 has individual probability densities from each of the four libraries too. There are large disagreements among the four libraries in the entire range of C/Es. Figures 106 through 109 show individual probability distributions for the ACT4, REAC-3, DKR-ICF, and RACC libraries, respectively. The figures also show the Gaussian distribution for each library. Figure 110 shows the confidence level as

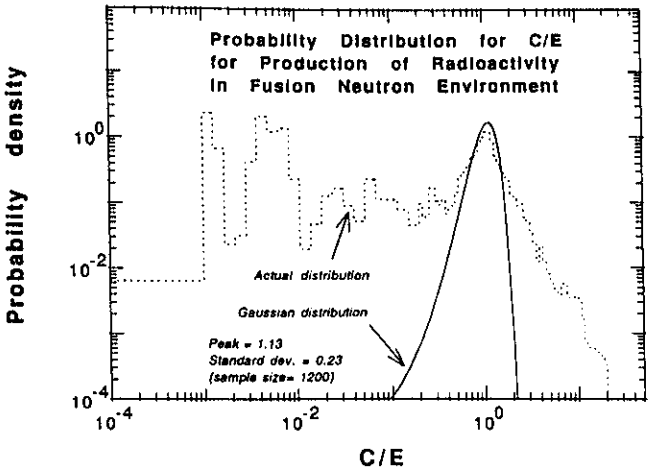

Fig. 103. Consolidated probability density distribution of C/Es obtained by combining results by all the four libraries, ACT4,REAC-3,DKR-ICF, and RACC.

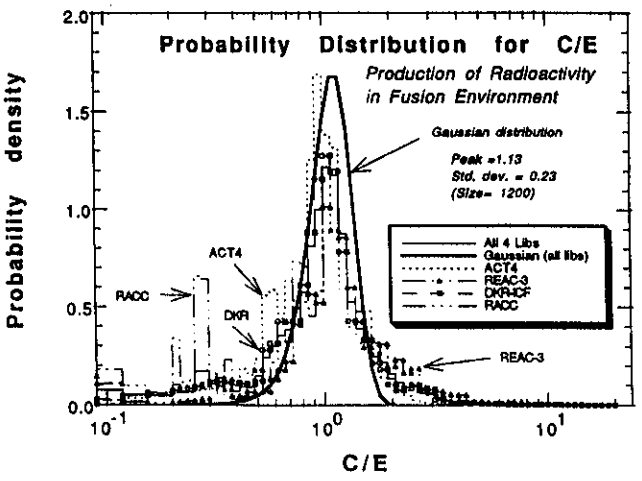

Fig. 105. Intercomparison of individual probability density distributions of C/Es obtained by each of the four libraries, ACT4, REAC-3, DKR-ICF, and RACC.

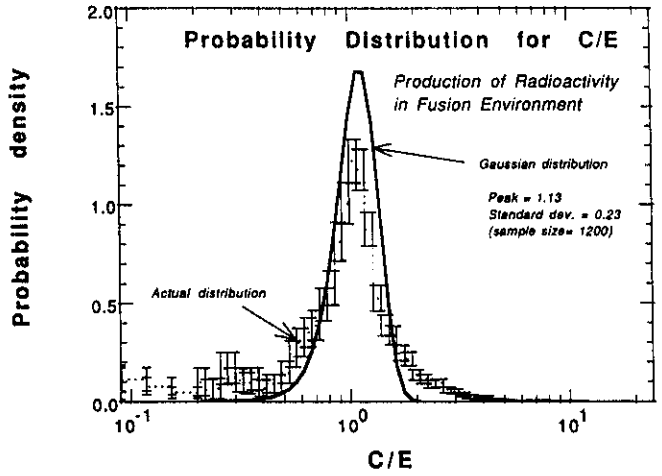

Fig. 104. Consolidated probability density distribution of C/Es with related uncertainties.

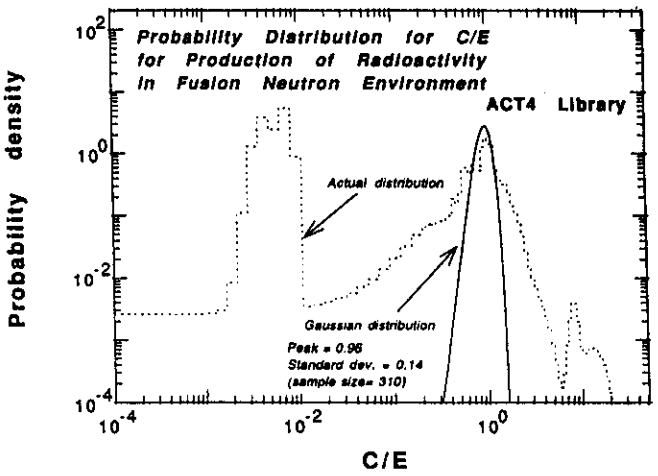

Fig. 106. Probability density distribution of C/Es obtained using ACT4 library.

a function of the safety factor for all the four libraries taken together. The maximum possible confidence level is unity. The figure also shows the uncertainty in the confidence level. It is evident that the confidence level improves very slowly beyond a safety factor value of 2. Figure 111 shows a plot of confidence level as a function of the safety factor for all four libraries. If one is willing to accept a confidence level of 70%, all the libraries will be usable without any need for a safety factor. Between a 70 to 80% confidence level, ACT4 appears to need the largest safety factor. Beyond 91%, however, ACT4 gets above both the DKR-ICF and RACC libraries, as shown in Fig. 112. The REAC-3 library is the most conservative library. It is very difficult to approach a 99% confidence level for all libraries even for a safety factor of 5.

VIII. RECOMMENDATIONS

In view of the large discrepancies observed between the calculations and the experimentally measured isotopic radioactivities, it is evident that much work needs to be undertaken both in the area of cross-section evaluation and the experimental measurement of the radioactivities. The calculation methods need to be improved too for bringing the discrepancies between the calculations and the measurements under control.

Tables XXIII and XXIV list the isotopic products for which the largest C/E dispersions have been reported in the present work. Practically, all the materials show up in this list. Although zirconium, molybdenum, tungsten, nickel, indium, zinc, vanadium, and cobalt have the largest number of the problematic isotopic

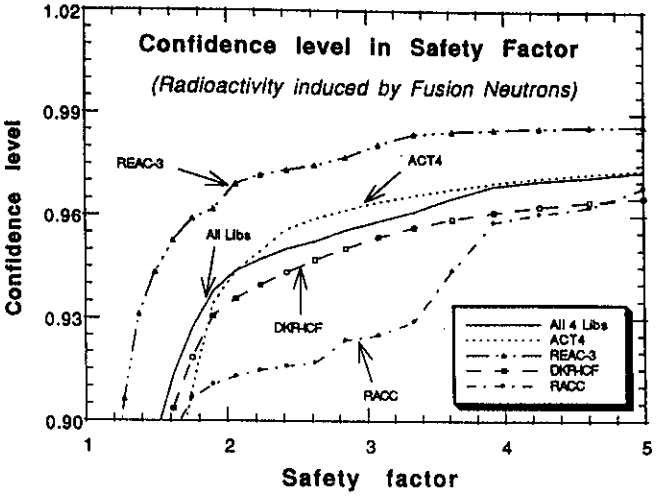

Fig. 112. Fractional confidence level (above 0.90) for each of the four libraries as a function of safety factor.

2. experiments embracing all the materials of interest to the ITER and DEMO fusion machines, provided it would be possible to improve significantly, by a factor of 10 or more above current levels, on the available neutron fluences. Basically, all the materials dealt with in the present work will have to be covered in addition to any new materials recommended by the designers.

The following suggestions are recommended to be implemented for enhancing the effectiveness and the quality of the future work:

1. There is a need to have a unique and complete cross-section library, using the most recent and available cross-section data. As a corollary, a single radioactivity code will be highly desirable for the best results.

2. A very fine energy group structure should be adopted for the unique cross-section library. A reasonable compromise for the total number of energy groups may be somewhere near 200.

3. The transport cross sections used for computing the neutron energy spectrum should use the same energy group structure as for the activation cross-section library. This will eliminate the calculational error resulting from the conversion of the neutron energy spectrum from one group structure to another.

4. There is a need to perform radioactivity experiments for all the materials under a large number of neutron energy spectra. This will help in checking the validity of the activation cross-section library over a large neutron energy range.

5. The cross-section evaluators need to begin with improving first those cross sections that are responsible for large C/E dispersions. Once these problem cross sections are greatly improved, the evaluators can move on to the remaining cross-section data.

IX. SUMMARY AND CONCLUSIONS

The U.S. DOE/JAERI collaborative experiments on radioactivity have spanned Phase-IIC through -IIIC (1988 through 1991). Source neutron intensity, neutron energy spectra, irradiation time, and cooling time have been the important variables. Phase-IIC was done with a point source. Phase-IIIA, -IIIB, and -IIIC have involved a simulated line source. The irradiated materials have included Fe, Ni, Cr, Mn-Cu alloy, Ti, Mo, Zr, Ta, W, Si, Mg, Al, V, Nb, SS316/AISI316, $YBa_2Cu_3O_7$, $ErBa_2Cu_3O_7$, Sn, Ag, Pb, Zn, In, and Au. All radioactive gamma emitters from these irradiated materials of half-lives less than ~5 yr have been the targets of interest.

An extensive database of measured decay gamma radioactivities for Fe, Ni, Cr, SS316, Mn, Mo, Cu, Co, Ti, V, Al, W, Zr, Zn, Sn, Nb, Pb, and Si has been compiled as a result of this collaborative program. Two kinds of analysis of these measured radioactivities have been conducted. The first analysis looked at the decay gamma radioactivities integrated over 100 KeV to 3 MeV of gamma energy for an irradiated material. This has been characterized as analysis of integrated decay gamma radioactivity. This method of analysis does not directly look at the role of the activation cross sections in the observed discrepancies between the calculations and the measurements. There are other parameters that can contribute to the observed C/E discrepancies: erroneous data on product half-life, branching ratios, and decay gamma yields. The second method of analysis is geared to look at each individual isotopic activity measured in the experiments. The calculation uses the data on half-lives, branching ratios, and the decay gamma yields as documented in Ref. 22. This eliminates the error contributed by these three factors; of course, one presumes that Ref. 22 has the correct data! The activation cross-section libraries of the four leading radioactivity codes, ACT4/THIDA-2, REAC-3, DKR-ICF, and RACC were used to analyze the measured isotopic activities. In the latter method, the C/E discrepancies can be believed to be coming from any or all of the following four sources: (a) activation cross-section data in the used library, (b) neutron energy spectra computed by transport code, (c) neutron energy spectrum conversion from the transport group structure to the activation library group structure, and (d) experimental error.

The analysis of the individual isotopic activities from irradiated samples of Al, Si, Ti, V, Cr, Mn, Fe, Co, Ni, Cu, SS316, Zn, Zr, Nb, Mo, In, Sn, Ta, W, and Pb has been reported in the present work. A number of neutron energy spectra have been covered in the analysis. The analysis has revealed large discrepancies

for all the materials in spite of the fact that at most 14 spectra have been included in the analysis. Incidentally, these are all quite hard neutron energy spectra. Vanadium, cobalt, nickel, zinc, zirconium, molybdenum, indium, tin, and tungsten show the largest number of discrepant isotopic activities.

From a reactor designer standpoint, it is important to know which activation library is the most suitable for doing the nucleonic design of a fusion reactor. The designer will like to be somewhat conservative in predicting radioactivity-related effects. In this regard, one can find that the use of engineering safety factors comes in very handy. In the present work, an attempt has been made to outline an approach to define a confidence level with a safety factor, employing the C/E results discussed in this work. It is also shown that a given confidence level generally carries an uncertainty.

A number of recommendations have been made for directing the future effort in the areas of radioactivity measurements and analyses for maximizing the resultant gains. Strong international coordination will be needed to sincerely implement these recommendations.

ACKNOWLEDGMENTS

The authors wish to acknowledge J. Kusano, C. Kutukake, S. Tanaka, and Y. Abe for the operation of the FNS accelerator.

The U.S. contributors were supported by the U.S. Department of Energy, Office of Fusion Energy, under contract DE-FG03-86ER52123.

REFERENCES

1. E. E. BLOOM et al., "Low Activation Materials for Fusion Applications," *J. Nucl. Mater.*, **122 & 123**, 17 (1984).

2. G. LOGAN, "A Rationale for Fusion Economics Based on Inherent Safety," *J. Fusion Energy*, **4**, 245 (1985).

3. T. NODA et al., "Materials Selection for Reduced Activation of Fusion Reactors," *J. Nucl. Mater.*, **155–157**, 581 (1988).

4. E. T. CHENG, "Radioactivity Aspects of Fusion Reactors," *Fusion Eng. Des.*, **8–10** (1989).

5. M. ZUCCHETTI, "Impurity Concentration Limits and Activation in Fusion Reactor Structural Materials," *Fusion Technol.*, **19**, 294 (1991).

6. L. R. GREENWOOD and D. L. BOWERS, "Production of Long-Lived Activities in Fusion Materials," *J. Nucl. Mater.*, **155–157**, 585 (1988).

7. R. W. CONN et al., "Lower Activation Materials and Magnetic Fusion Reactors," *Nucl. Technol./Fusion*, **5**, 291 (1984).

8. A. KUMAR, M. A. ABDOU, Y. IKEDA, and C. KONNO, "Radioactivity and Nuclear Heating Measurements for Fusion Applications," *Proc. Symp. Fusion Technology*, p. 872, B. E. KEEN, M. HUGUET, and R. HEMSWORTH, Eds., Elsevier, New York (1991).

9. Y. IKEDA, C. KONNO, T. NAKAMURA, A. KUMAR, and M. A. ABDOU, "Experiment on Induced Activities and Decay-Heat in Simulated D-T Neutron Fields: JAERI/USDOE Collaborative Program on Fusion Neutronics," *Fusion Technol.*, **19**, 1961 (1991).

10. A. KUMAR, M. A. ABDOU, Y. IKEDA, and T. NAKAMURA, "Analysis of Induced Activities Measurements Related to Decay-Heat in Phase IIC Experimental Assembly: USDOE/JAERI Collaborative Program on Fusion Neutronics Experiments," *Fusion Technol.*, **19**, 1909 (1991).

11. A. KUMAR, M. Z. YOUSSEF, Y. IKEDA, and C. KONNO, "Experiments and Analysis for Measurements of Decay-Heat Related Induced Activities in Simulated Line Source Driven D-T Neutron Fields of Phase IIIA: USDOE/JAERI Collaborative Program on Fusion Neutronics," *Fusion Technol.*, **19**,1859 (1991).

12. A. KUMAR, "Measurement and Analysis of Decay Radioactivity Data on Tungsten," Memo, University of California, Los Angeles (Feb. 19, 1991).

13. Y. IKEDA, C. KONNO, Y. OYAMA, T. NAKAMURA, A. KUMAR, M. Z. YOUSSEF, and M. A. ABDOU, "Experimental Verification of the Current Data and Methods for Induced Radioactivity and Decay Heat Calculation in D-T Fusion Reactors," *Fusion Eng. Des.*, **18**, 387 (1991).

14. A. KUMAR, M. A. ABDOU, and J.-P. SCHNEEBERGER, "Integral Fusion Neutronics Experiments and Analysis," *Proc. Topl. Mtg. New Horizons in Radiation Protection and Shielding*, Pasco, Washington, April 26–30, 1992, p. 619, American Nuclear Society (1992).

15. Y. IKEDA, A. KUMAR, and C. KONNO, "Measurements of Long-Lived Activation Cross Sections by 14 MeV Neutrons at FNS," presented at Int. Conf. Nuclear Data for Science and Technology, Julich, Germany (May 1991); see also *Proc. Int. Workshop on Fusion Neutronics*, June 7, 1991, Karlsruhe, Germany, p. 172; see also Memo 03-305, Japan Atomic Energy Research Institute (Sep. 1991).

16. A. KUMAR et al., "Measurements of Decay Radioactivity of Long-lived Isotopes," *Fusion Technol.*, **21**, 2180 (1992).

17. A. KUMAR et al., "Induced Radioactivity Measurements in Fusion Neutron Environment: Joint Report of USDOE/JAERI Collaborative Program on Fusion Neutronics," UCLA-ENG-91-32/UCLA-FNT-53, University of California, Los Angeles and JAERI-M-93-018, Japan Atomic Energy Research Institute (Feb. 1993).

18. Y. SEKI et al., "THIDA-2: An Advanced Code System for Calculation of Transmutation, Activation, Decay Heat

and Dose Rate," CCC-410, Radiation Shielding Information Center (Apr. 1987).

19. F. M. MANN, "REAC*2: Users Manual and Code Description," WHC-EP-0282, Westinghouse Hanford Company (1989).

20. D. L. HENDERSON and O. YASAR, "A Radioactivity and Dose Rate Calculation Code Package," Vols. 1 and 2, CCC-323, Radiation Shielding Information Center (Apr. 1987).

21. J. JUNG, "Theory and Use of the Radioactivity Code RACC," ANL/FPP/TM-122, Argonne National Laboratory (1979).

22. E. BROWNE and R.B. FIRESTONE, *Table of Radioactive Isotopes*, V.S. SHIRLEY, Ed., Wiley-Interscience, New York (1986).

23. T. NAKAMURA et al., "A Line D-T Neutron Source Facility for Annular Blanket Experiment: Phase III of the JAERI/USDOE Collaborative Program on Fusion Neutronics," *Fusion Technol.*, **19**, 1873 (1991).

24. Y. OYAMA et al., "Annular Blanket Experiment Using a Line DT Neutron Source: Phase IIIA of the JAERI/USDOE Collaborative Program on Fusion Neutronics," *Fusion Technol.*, **19**, 1879 (1991).

25. Y. OYAMA et al., "Phase III Experimental Results of JAERI/USDOE Collaborative Program on Fusion Neutronics," *Fusion Eng. Des.*, **18**, 203 (1991).

26. *Table of Isotopes*, C. M. LEDERER and V. SHIRLEY, Ed., 7th ed., John Wiley and Sons, New York (1978).

27. H. BABA, "Gamma-Ray Spectrum Analysis Code for Ge(Li) Detectors," PSR-84, Radiation Shielding Information Center (1978); see also JAERI-M 7017, Japan Atomic Energy Research Institute (1977).

28. "MCNP—An General Monte Carlo Code for Neutron and Photon Transport: Version 3A," LA-7396-M, Rev. 2, J. F. BRIESMEISTER, Ed., Los Alamos National Laboratory (Sep. 1988); see also MCNP3B, Los Alamos National Laboratory (July 1988).

29. L. P. KU and J. KOLIBAL, "RUFF—A Ray Tracing Program to Generate Uncollided Flux and First Collision Moments for DOT 4, A User's Manual," EAD-R-16, Princeton University Plasma Physics Laboratory (1980).

30. W. A. RHOADES and R. L. CHILDS, "DOT-IV Version 4.3: One and Two Dimensional Transport Code Collection," CCC-429, Radiation Shielding Information Center (May 1984).

31. R. E. MacFARLANE, "TRANSX-CTR: A Guide for Interfacing MATXS Cross-Section Libraries to Nuclear Transport Codes for Fusion Systems Analysis," LA-9863-MS, Los Alamos National Laboratory (Feb. 1984).

32. Y. IKEDA et al., "Measurements of Induced Activity in Type 316 Stainless Steel by Irradiation in D-T Neutron Fields," *Fusion Technol.*, **8**, 1466 (1985).

33. A. KUMAR and C. SAHRAOUI, "Analysis of Activation Measurements done on Slabs of Beryllium and Lead at LOTUS Facility," *Fusion Technol.*, **3**, 484 (1988).

34. S. AZAM and A. KUMAR, "Analysis and Measured Integral Data on an Experimental Lithium Module at the LOTUS Neutronics Facility," *Nucl. Eng. Des./Fusion*, **19**, 259 (1992).

35. M. E. SAWAN and L. A. EL-GUEBALY, "Three-Dimensional Neutronics Analysis for the U.S. Magnet Shield of ITER," *Fusion Technol.*, **19**, 1469 (1991).

36. L. A. EL-GUEBALY, "Overview of the US-ITER Magnet Shield: Concept and Problems," *Fusion Technol.*, **19**, 1475 (1991).

37. A. KUMAR and Y. IKEDA, "On Disagreement Between Measurements and Calculations of D-T Neutron Driven Induced Radioactivity and Nuclear Heating," *Proc. Int. Conf. Nuclear Data for Science and Technology*, Gatlinburg, Tennessee, May 9–13, 1994, p. 883, American Nuclear Society (1994).

Anil Kumar (PhD, University of Bombay, India, 1981) is senior development engineer at the University of California, Los Angeles (UCLA). His current research interests include fusion reactor nucleonics experiments and analysis, technique development for nuclear heating, decay heat measurements, biological dose, fusion diagnostics, safety factor methodology for fusion reactor design parameters, low-activation materials, inertial confinement fusion, and sequential reactions. He has conducted experiments at leading facilities such as the Fusion Neutronics Source (FNS) facility in Japan, the Tokamak Fusion Test Reactor (TFTR) at Princeton University, and LOTUS in Switzerland.

Yujiro Ikeda (PhD, nuclear engineering, Nagoya University, Japan, 1981) is head of the Fusion Neutronics Laboratory in the Department of Reactor Engineering at the Japan Atomic Energy Research Institute (JAERI). He has worked in the areas of fusion neutronics experiments, induced radioactivity

experiment and analysis, direct nuclear heating measurements, activation cross-section measurements, and fusion dosimetry.

Mohamed A. Abdou is a professor in the Department of Mechanical, Aerospace, and Nuclear Engineering at UCLA and also is the director of fusion technology at UCLA. His research interests include neutronics, thermomechanics, fusion technology, and reactor design and analysis. He served as the U.S. leader of the JAERI/U.S. Department of Energy (U.S. DOE) collaboration on fusion blanket neutronics.

Mahmoud Z. Youssef (PhD, nuclear engineering, University of Wisconsin, 1980) is a senior research engineer in the Department of Mechanical, Aerospace, and Nuclear Engineering at UCLA. He participated in several conceptual magnetic fusion energy and inertial fusion energy reactor design studies with emphasis on nuclear analysis and blanket/shield design. His research interests are in the areas of blanket/shield design optimization, nuclear data, sensitivity/uncertainty studies, neutronics methods and code development, tritium fuel cycle, radioactivity and safety aspects of fusion, integral experiments, neutronics testing, and research and development for fusion reactors, particularly the International Thermonuclear Experimental Reactor (ITER).

Chikara Konno (MS, physics, Kyoto University, Japan, 1985) is a research scientist in the Department of Reactor Engineering at JAERI. He has worked in the areas of fusion neutronics experiments, cross-section measurements, and neutron spectrum measurements using a proton-recoil counter.

Kazuaki Kosako (BE, atomic engineering, Tokai University, Japan, 1984) has worked at Sumitomo Atomic Energy Industries since 1994. He worked in the Department of Reactor Engineering at JAERI from 1984 to 1992 where he was involved mainly in fusion neutronics. He is currently interested in the area of radiation damage of materials.

Yukio Oyama (BS, physics, 1975; MS, nuclear physics, 1977; and Dr. Eng., 1989, Osaka University, Japan) is a principal scientist at JAERI. He has worked in the area of fusion neutronics experiments since 1978. He is currently involved in intense and high-energy neutron source projects.

Tomoo Nakamura (BS, physics, Kyoto University, Japan, 1957) is currently director of the Public Acceptance Database Center, Research Organization for Information Science and Technology. His research background includes experimental reactor physics on fast breeder reactors and nuclear technology on fusion reactor blankets. He served as the former Japanese leader of the JAERI/U.S. DOE collaboration on fusion blanket neutronics.

Hiroshi Maekawa (BE, 1965; MS, 1967; and Dr. Eng., 1970, nuclear engineering, Tokyo Institute of Technology, Japan) is the deputy director of the Department of Reactor Engineering and the head of the Intense Neutron Source Laboratory at JAERI. He has worked on fusion neutronics for more than 20 years, and he planned and constructed the FNS facility. He served as the Japanese leader of the JAERI/U.S. DOE collaboration on fusion blanket neutronics. His recent research has focused on International Fusion Materials Irradiation Facility conceptual design activities.